





Research Article

A Novel Adaptive Square Root UKF with Forgetting Factor for the Time-Variant Parameter Identification

Yanzhe Zhang ^{1,2}, Yong Ding ^{3,4}, Jianqing Bu ^{1,5,6} and Lina Guo ⁷

¹State Key Laboratory of Mechanical Behavior and System Safety of Traffic Engineering Structures, Shijiazhuang Tiedao University, Shijiazhuang 050043, China

²School of Civil Engineering, Shijiazhuang Tiedao University, Shijiazhuang 050043, China

³School of Civil Engineering, Harbin Institute of Technology, Harbin 150090, China

⁴Key Lab of Structures Dynamic Behavior and Control (Harbin Institute of Technology), Ministry of Education, Heilongjiang, Harbin 150090, China

⁵School of Traffic and Transportation, Shijiazhuang Tiedao University, Shijiazhuang 050043, China

⁶Key Laboratory of Traffic Safety and Control of Hebei Province, Hebei Province, Shijiazhuang, China

⁷College of Water Conservancy and Civil Engineering, Northeast Agricultural University, Harbin 150048, China

Correspondence should be addressed to Jianqing Bu; bujq_stdu@163.com

Received 6 March 2023; Revised 8 August 2023; Accepted 12 August 2023; Published 6 September 2023

Academic Editor: Fabio Casciati

Copyright © 2023 Yanzhe Zhang et al. This is an open access article distributed under the Creative Commons Attribution License, which permits unrestricted use, distribution, and reproduction in any medium, provided the original work is properly cited.

The unscented Kalman filter (UKF) serves as an efficient estimator widely utilized for the recursive identification of parameters. However, the UKF is not well suited for tracking time-variant parameters. Moreover, the unscented transformation (UT) used in the UKF typically relies on Cholesky decomposition to perform the square root operation of the covariance matrix. This method necessitates the matrix to maintain symmetry and positive definiteness. Due to the adverse influence of rounding error and noise, it becomes challenging to guarantee the positive definiteness of the matrix in each recursive step for practical engineering. The square root UKF (SRUKF) eliminates the need for the square root operation in the UT by directly updating the square root of the covariance matrix during each recursion. However, the SRUKF still relies on the rank 1 update to the Cholesky factorization to perform the recursive process, which also necessitates the matrix to be positive definite. Furthermore, the SRUKF is ineffective in the identification of time-variant parameters. Therefore, this paper proposes a modification to the SRUKF that ensures unconditional numerical stability by utilizing QR decomposition. Subsequently, the modified square root UKF (MSRUKF) method is enhanced by incorporating an adaptive forgetting factor that can be adjusted based on the residual information from each recursive step. This adaptation leads to the development of the adaptive SRUKF with forgetting factor (ASRUKF-FF) method, which significantly improves the tracking capability for time-variant parameters. To validate the effectiveness of the proposed method, this paper demonstrates its application in identifying the time-variant stiffness and damping parameters of a three-story frame structure. In addition, the method is employed to estimate the time-variant stiffness of the bridge excited by vehicles. The simulation results show that the proposed method has the superiority of high accuracy, strong robustness, and widespread applicability, even with incomplete measurements and inappropriate parameter settings.

1. Introduction

During the service life of civil engineering structures, when subjected to extreme loads, the structural parameters may experience sudden or gradual changes, including stiffness degradation and an increase in damping. The challenge of accurately tracking parameter changes has been a topic of

ongoing interest in the field of civil engineering [1, 2]. Timely and accurate understanding of the changing characteristics of structural parameters holds great significance for tasks such as structural optimization design, maintenance, and reinforcement, as well as the selection of postdisaster rescue routes. When civil engineering structures are subjected to extremely large external excitations, such as earthquakes on

buildings or overweight vehicles on bridges, they often exhibit nonlinear behavior. Furthermore, the identification of time-variant parameters in structures remains challenging due to factors such as incomplete test information, model errors, measurement noise, and other interferences.

Over the past few decades, several parameter identification technologies have been developed to address the challenge of identifying time-variant parameters in nonlinear structures. Representative researches mainly include time, frequency, and time-frequency domain signal processing methods [3–9]. In the time-frequency domain methods, the wavelet multiresolution analysis (WMA), Hilbert transform (HT), Hilbert–Huang transform (HHT), and variational mode decomposition (VMD) are fully developed for different applications. However, the WMA requires complete knowledge of displacement, velocity, and acceleration responses at all degrees of freedom, as well as external load information [10], which limits its practical application. In addition, the HT, HHT, and VMD methods can only provide empirical information [11] and lack strict mathematical derivation. Considering that only time-domain methods can be applied for online identification due to their recursive characteristics, while basic frequency domain methods are generally nonrecursive [12], time-domain methods such as least squares estimation (LSE), extended Kalman filter (EKF), unscented Kalman filter (UKF), Monte Carlo filter (MCF), and others [13–21] have received significant attention.

The LSE method optimizes parameters by minimizing the errors between measured and simulated responses [22]. However, the LSE requires measurements of all displacement and velocity values. The identification process of the MCF method often necessitates a significant number of sampling points, leading to high computational demands [2]. Compared to the LSE and MCF methods, the EKF and UKF offer a significant advantage as fast online identification methods with recursive characteristics. When new data are measured, the EKF and UKF can efficiently update the parameters through Bayesian data fusion technology [23, 24], which is known for its space-saving and high-efficiency capabilities. However, the EKF is typically employed for handling weakly nonlinear problems and requires the computation of complex Jacobian matrices when linearizing nonlinear functions using the first-order Taylor series expansion technique. In addition, the EKF algorithm can diverge if the sampling interval is not small enough. To address the limitations of the EKF, the UKF was introduced by Julier and Uhlmann in 1995, specifically designed to handle strongly nonlinear problems [25, 26]. In the UKF, it is assumed that the system state vector and noise follow Gaussian probability distributions. The systematic mean and covariance are deterministically sampled using the unscented transformation (UT) to generate sigma points. By approximating the probability density distribution of the nonlinear function, the UKF avoids errors caused by directly linearizing the nonlinear function and achieves accuracy beyond second-order. Currently, the UKF has gained widespread adoption in the field of constant parameter identification and load identification [27, 28]. However, in

practical applications, the UT process of the UKF requires the covariance matrix to be positive definite. Due to the adverse influence of rounding error and noise, the covariance matrix can become nonpositive definite during the actual recursive process, leading to the divergence of the recursive algorithm. To address this issue, Van der Merwe et al. [29] proposed the SRUKF method, building upon the UKF framework. The SRUKF directly recurses the square root of the covariance matrix, eliminating the need for square root operations and enhancing the numerical stability of the UKF algorithm to a certain extent.

Some research studies further show that both the UKF and SRUKF methods are ineffective in accurately identifying time-variant parameters [1, 2, 30]. The values of the state covariance, modeling error covariance (\mathbf{Q} in Section 2.1), and measurement error covariance (\mathbf{R} in Section 2.1) matrices significantly impact the stability and accuracy of the identification process as they represent model uncertainty and measurement noise levels. It is crucial to determine appropriate and reasonable values for these matrices. As a result, most existing adaptive methods related to the UKF are modifications that focus on adjusting one or more of these three variables. Representative research in this area includes the state covariance adaptive filter [1, 12, 30–33], the Sage–Husa adaptive filter [2, 30, 34–37], the dual adaptive filter [38], the forgetting factor filter [39, 40], and the moving window adaptive filter [40, 41]. In the state covariance adaptive filter, as described in [30], the prior state covariance in the time update step was uniformly enlarged using an adaptive weighting coefficient λ_k . This coefficient was calculated based on a fading factor formula, where the choice of the forgetful factor was determined through empirical experience. However, in [1, 12, 31], only specific major diagonal elements corresponding to time-variant parameters of the state covariance matrix were expanded, while the other elements remained unchanged. Further analysis reveals that in [1, 12] and [31], the decision regarding which major diagonal element needs to be expanded is made by comparing the sensitive parameter with a threshold. This threshold is calculated based on transcendental probability. In the context of the strong tracking filter, the authors in [32, 33] introduced a correction to the prior state covariance using a fading factor that can be approximated through a suboptimal algorithm. The derivation process of this fading factor is known to be highly complex. After verification, the abovementioned state covariance correction technologies are all applicable to time-variant parameter identification. In the case of the Sage–Husa adaptive filter, the authors in [2] focused on modifying the measurement error covariance, while the authors in [30, 34–37] simultaneously addressed the revision of both the modeling error covariance and the measurement error covariance. Furthermore, the authors in [34, 37] introduced further simplifications to the correction formula. Regrettably, among the mentioned Sage–Husa adaptive filter studies, only the authors in [30] took into account the time-variant characteristics of structural parameters. Furthermore, according to the research conducted by Yang and Gao [42], when the statistical characteristics of modeling error

and measurement error are unknown, simultaneous estimation of them based on the Sage–Husa noise estimator is susceptible to algorithm divergence. Regarding the other adaptive filters, the studies [38, 40] primarily focused on addressing the impact of model uncertainty. They tackled the issue of updating the nonlinear finite element model when uncertainties existed in parameters such as geometry, node mass, dead load, damping coefficient, and the number of integration points. However, it should be noted that the studies [38, 40] did not specifically address the time-variant problem of parameters. Similarly, the methods proposed in [39, 41] are primarily utilized for fault diagnosis purposes. Although these methods are effective in handling time-varying noise systems, they do not specifically address the time-variant parameter identification problem. By the way, the measurement error covariance was modified in [38–40], while the modeling error covariance and measurement error covariance were improved simultaneously in [41].

Based on the analysis provided, it can be concluded that methods based on state covariance correction technology, as well as a limited number of Sage–Husa adaptive filters, have shown effectiveness in identifying time-variant parameters. Nevertheless, it should be noted that the proposed Sage–Husa adaptive methods may encounter numerical stability issues in certain scenarios. Furthermore, it is worth mentioning that the adaptive filters proposed in [30, 32, 33] are based on the SRUKF method [29], which still relies on the rank 1 update to Cholesky factorization process. This requirement for positive-definiteness in the matrix indicates that the SRUKF does not fundamentally resolve the issue of numerical instability in calculations. Indeed, the authors in [34] proposed a modified SRUKF method; however, it is acknowledged that the derivation of the adaptive algorithm in this approach can be relatively complex. Therefore, taking inspiration from the concept presented in literature [34], this paper modifies the standard SRUKF by incorporating QR decomposition. This modification aims to ensure the unconditional stability of the algorithm. Subsequently, the state covariance correction technology is applied to the MSRUKE algorithm, leading to the proposal of the ASRUKE-FF method. In contrast to the aforementioned methods, where the covariance correction coefficient is typically an empirical constant or determined through experience, this paper introduces a novel approach. The correction coefficient of the state covariance can be adaptively adjusted based on the forgetting factor, which follows a clear mathematical derivation process. Furthermore, the proposed adaptive algorithm is characterized by its simplicity in implementation, ease of programming, and robustness. The specific arrangement of this paper is as follows: the algorithms used are described in Section 2. The identification of time-variant stiffness and damping of a three-degree-of-freedom frame structure is presented in Section 3. The identification of time-variant stiffness of a simply supported bridge in the vehicle bridge system is considered in Section 4. Finally, the conclusion is obtained in Section 5.

2. Algorithms Description

2.1. The Standard Square Root UKF. The SRUKF method is a model-driven algorithm that enables the direct utilization of optimization algorithms for the identification of structural parameters. This can be accomplished by leveraging the equations in state space. The state and measurement equations of the nonlinear discrete-time system can be expressed in the following equations, respectively:

$$\mathbf{X}_k = f(\mathbf{X}_{k-1}, \mathbf{u}_{k-1}) + \mathbf{w}_{k-1}, \quad (1)$$

$$\mathbf{Y}_k = h(\mathbf{X}_k) + \mathbf{v}_k, \quad (2)$$

where k is the discrete time, \mathbf{X} is the system state vector, \mathbf{u} is the system input matrix, \mathbf{Y} is the system measurement vector, \mathbf{w} and \mathbf{v} are the modeling error and measurement error, respectively, and $f(\bullet)$ and $h(\bullet)$ represent the nonlinear function; both \mathbf{w} and \mathbf{v} are assumed to follow a Gaussian distribution and satisfy the following relationship: $\mathbf{w} \sim N(\mathbf{0}, \mathbf{Q})$ and $\mathbf{v} \sim N(\mathbf{0}, \mathbf{R})$.

The algorithm procedure of the standard SRUKF method can be described as follows:

- (1) Initialization of the state vector and square root of the state covariance matrix:

$$\hat{\mathbf{X}}_0^+ = E[\mathbf{X}_0], \quad (3)$$

$$\mathbf{S}_0^+ = \text{chol}[\mathbf{P}_0^+] = \text{chol}\left\{E\left[(\mathbf{X}_0 - \hat{\mathbf{X}}_0^+)(\mathbf{X}_0 - \hat{\mathbf{X}}_0^+)^T\right]\right\}, \quad (4)$$

where $\hat{\mathbf{X}}_0^+$ is the initial state vector and \mathbf{X}_0 denotes the initial values determined by experience, finite element analysis, or design drawings. $\hat{\mathbf{P}}_0^+$ is the initial state covariance matrix that is composed of uncorrelated diagonal elements [43]. $\hat{\mathbf{P}}_0^+$ represents the confidence in the initial state estimates and must be specified a priori. In the absence of any prior knowledge of \mathbf{X}_0 , it is common to assume high values for $\hat{\mathbf{P}}_0^+$ [44, 45]. $\text{chol}\{\bullet\}$ denotes Cholesky factorization.

- (2) Time update:

$$\begin{aligned} \chi_{k-1}^{(0)} &= \hat{\mathbf{X}}_{k-1}^+, \\ \chi_{k-1}^{(i)} &= \hat{\mathbf{X}}_{k-1}^+ + (\sqrt{(n+\lambda)} \mathbf{S}_{k-1}^+)_i, \quad i = 1, 2, \dots, n, \\ \chi_{k-1}^{(i+n)} &= \hat{\mathbf{X}}_{k-1}^+ - (\sqrt{(n+\lambda)} \mathbf{S}_{k-1}^+)_i, \quad i = 1, 2, \dots, n, \end{aligned} \quad (5)$$

$$\hat{\mathbf{X}}_k^{(j)} = f(\chi_{k-1}^{(j)}, \mathbf{u}_{k-1}), \quad j = 0, 1, 2, \dots, 2n, \quad (6)$$

$$\hat{\mathbf{X}}_k^- = \sum_{i=0}^{2n} W_m^{(j)} \hat{\mathbf{X}}_k^{(j)}, \quad (7)$$

$$\mathbf{S}_k^- = \text{qr}\left\{\left[\sqrt{W_c^{(j)}} \left(\hat{\mathbf{X}}_k^{(1:2n)} - \hat{\mathbf{X}}_k^-\right), \sqrt{\mathbf{Q}_k}\right]^T\right\}, \quad (8)$$

$$\mathbf{S}_k = \text{cholupdate}\left\{\mathbf{S}_k^-, \sqrt{W_c^{(0)}}\left(\hat{\mathbf{X}}_k^{(0)} - \hat{\mathbf{X}}_k^-\right), \text{sgn}\{W_c^{(0)}\}\right\}, \quad (9)$$

where n is the dimension of the state vector, $qr\{\bullet\}$ denotes the QR decomposition that returns the upper triangular part of the matrix, $\text{cholupdate}\{\bullet\}$ denotes the rank 1 update to Cholesky factorization which also returns the upper triangular Cholesky factor, and $\text{sgn}\{\bullet\}$ is the sign function. As an illustration, $\text{cholupdate}\{\mathbf{A}, \mathbf{B}, \pm c\}$ gives the Cholesky factor of $(\mathbf{D} \pm c \mathbf{B}\mathbf{B}^T)$, where $\mathbf{A} = \text{chol}\{\mathbf{D}\}$. For more operation details of (8) and (9), please refer to [29, 46].

(3) Measurement prediction:

$$\begin{aligned} \hat{\chi}_k^{(0)} &= \hat{\mathbf{X}}_k^-, \\ \hat{\chi}_k^{(i)} &= \hat{\mathbf{X}}_k^- + \left(\sqrt{(n+\lambda)} \mathbf{S}_k\right)_p, \quad i = 1, 2, \dots, n, \\ \hat{\chi}_k^{(i+n)} &= \hat{\mathbf{X}}_k^- - \left(\sqrt{(n+\lambda)} \mathbf{S}_k\right)_p, \quad i = 1, 2, \dots, n. \end{aligned} \quad (10)$$

$$\hat{\mathbf{y}}_k^{(j)} = h(\hat{\chi}_k^{(j)}), \quad j = 0, 1, 2, \dots, 2n, \quad (11)$$

$$\hat{\mathbf{y}}_k = \sum_{i=0}^{2n} W_m^{(j)} \hat{\mathbf{y}}_k^{(j)}, \quad (12)$$

$$\mathbf{S}_{y,k}^- = qr\left\{\left[\sqrt{W_c^{(j)}}\left(\hat{\mathbf{y}}_k^{(1:2n)} - \hat{\mathbf{y}}_k\right), \sqrt{\mathbf{R}_k}\right]^T\right\}, \quad (13)$$

$$\mathbf{S}_{y,k} = \text{cholupdate}\left\{\mathbf{S}_{y,k}^-, \sqrt{W_c^{(0)}}\left(\hat{\mathbf{y}}_k^{(0)} - \hat{\mathbf{y}}_k\right), \text{sgn}\{W_c^{(0)}\}\right\}, \quad (14)$$

$$\mathbf{P}_{x,y,k} = \sum_{i=0}^{2n} W_c^{(j)} \left(\hat{\mathbf{X}}_k^{(j)} - \hat{\mathbf{X}}_k^-\right) \left(\hat{\mathbf{y}}_k^{(j)} - \hat{\mathbf{y}}_k\right)^T. \quad (15)$$

(4) Measurement update:

$$\mathbf{K}_k = \frac{\mathbf{P}_{x,y,k}}{\left(\mathbf{S}_{y,k}^T \mathbf{S}_{y,k}\right)}, \quad (16)$$

$$\hat{\mathbf{X}}_k^+ = \hat{\mathbf{X}}_k^- + \mathbf{K}_k (\mathbf{y}_k - \hat{\mathbf{y}}_k), \quad (17)$$

$$\Omega = \mathbf{K}_k \mathbf{S}_{y,k}^T, \quad (18)$$

$$\mathbf{S}_k^+ = \text{cholupdate}\{\mathbf{S}_k, \Omega, -1\}, \quad (19)$$

where y_k is the measurement at step k .

Weights can be expressed as

$$W_c^{(j)} = \begin{cases} \frac{\lambda}{n+\lambda} + 1 - a^2 + b, \\ \frac{1}{2(n+\lambda)}, \end{cases} \quad (20)$$

$$W_m^{(j)} = \begin{cases} \frac{\lambda}{n+\lambda}, \\ \frac{1}{2(n+\lambda)}, \end{cases} \quad (21)$$

where $\lambda = \alpha^2(n + \kappa) - n$ is a compound scaling parameter. $10^{-4} \leq \alpha \leq 1$ is the primary scaling factor determining the extent of the spread of the sigma points around the prior mean. b is a secondary scaling factor used to emphasize the weighting on the zeroth sigma point for the posterior covariance calculation. For Gaussian priors, $b = 2$ is optimal. κ is a tertiary scaling factor and is usually set equal to $3 - n$.

2.2. The Modified Square Root UKF. The standard SRUKF method updates the square root of the covariance matrix by utilizing the rank 1 update to Cholesky factorization. Taking (9) as an illustration, the equivalent form of (9) can be written as

$$\mathbf{P}_k^- = \mathbf{S}_k^T \mathbf{S}_k = \left(\mathbf{S}_k^-\right)^T \mathbf{S}_k^- + W_c^{(0)} \left(\hat{\mathbf{X}}_k^{(0)} - \hat{\mathbf{X}}_k^-\right) \left(\hat{\mathbf{X}}_k^{(0)} - \hat{\mathbf{X}}_k^-\right)^T, \quad (22)$$

where \mathbf{P}_k^- is the prior state covariance calculated by the time update step of the conventional UKF method, and the zero-order weight $W_c^{(0)}$ contains positive or negative signs.

To calculate \mathbf{S}_k using equation (9), the matrix on the right-hand side of equation (22) must be positive definite, indicating that the standard SRUKF method does not fundamentally eliminate the requirement for a positive-definite covariance matrix. The presence of a negative zero-order weight can indeed contribute to the matrix on the right-hand side of equation (22) not being positive definite. From equation (20), when $\kappa = 3 - n$ and $\beta = 2$, $W_c^{(0)} = 4 - n/3\alpha^2 - \alpha^2$. Because the value of α is usually small, when the dimension of the state vector is large, the zero-order weight may have a negative value, which will cause the matrix on the right-hand side equation (22) to be nonpositive, affecting the stability of the recursive algorithm.

According to Cholesky decomposition, the prior state covariance of the time update step of UKF is $\mathbf{P}_k^- = \mathbf{S}_k^T \mathbf{S}_k$. Let $\mathbf{S}_k = \mathbf{q}\mathbf{r}$, where \mathbf{q} is an orthogonal square matrix and \mathbf{r} is an upper triangular matrix, then $\mathbf{P}_k^- = \mathbf{S}_k^T \mathbf{S}_k = (\mathbf{q}\mathbf{r})^T (\mathbf{q}\mathbf{r}) = \mathbf{r}^T \mathbf{r}$. Therefore, the following relationship can be obtained:

$$\mathbf{S}_k = \mathbf{r}^T. \quad (23)$$

The UT process typically generates $(2n + 1)$ sigma points using symmetrical sampling. The sigma points are symmetrically distributed around the origin (zero point) to maintain the consistency of the sample's mean and covariance with the original state's distribution. Because removing the sigma point at the origin position does not impact the mean and covariance of the remaining sample points, based on this idea and according to equation (23), equations (8) and (9) can be replaced as follows:

$$\mathbf{r}_1 = \text{qr} \left\{ \left[\sqrt{W_c^{(j)}} \left(\widehat{\mathbf{X}}_k^{(1:2n)} - \widehat{\mathbf{X}}_k^- \right), \sqrt{\mathbf{Q}_k} \right]^T \right\}, \quad (24)$$

$$\mathbf{S}_k = \mathbf{r}_1^T. \quad (25)$$

Similarly, equations (13) and (14) can be replaced as follows:

$$\mathbf{r}_2 = \text{qr} \left\{ \left[\sqrt{W_c^{(j)}} \left(\widehat{\mathbf{y}}_k^{(1:2n)} - \widehat{\mathbf{y}}_k^- \right), \sqrt{\mathbf{R}_k} \right]^T \right\}, \quad (26)$$

$$\mathbf{S}_{y,k} = \mathbf{r}_2^T. \quad (27)$$

To update equations (18) and (19), it is necessary to derive them using the conventional UKF algorithm and the definition of covariance. First, the equivalent form of

equations (18) and (19) is expressed as equation (28). The matrix on the right-hand side of equation (28) still needs to be positive definite, which is not conducive to the stability of the recursive algorithm.

$$\begin{aligned} \mathbf{P}_k^+ &= (\mathbf{S}_k^+)^T \mathbf{S}_k^+ \\ &= \mathbf{S}_k^T \mathbf{S}_k - \mathbf{K}_k \mathbf{S}_{y,k}^T \mathbf{S}_{y,k} \mathbf{K}_k^T, \end{aligned} \quad (28)$$

where \mathbf{P}_k^+ is the posterior state covariance of the measurement update step of the conventional UKF method.

Second, the following relationship is obtained based on the posterior state covariance definition and equation (17):

$$\begin{aligned} \mathbf{P}_k^+ &= (\mathbf{S}_k^+)^T \mathbf{S}_k^+ = E \left[(\mathbf{X}_k - \widehat{\mathbf{X}}_k^+) (\mathbf{X}_k - \widehat{\mathbf{X}}_k^+)^T \right] \\ &= E \left[(\mathbf{X}_k - \widehat{\mathbf{X}}_k^- - \mathbf{K}_k (\mathbf{y}_k - \widehat{\mathbf{y}}_k)) (\mathbf{X}_k - \widehat{\mathbf{X}}_k^- - \mathbf{K}_k (\mathbf{y}_k - \widehat{\mathbf{y}}_k))^T \right]. \end{aligned} \quad (29)$$

By considering the measurement equation of (1), we can establish the following relationship:

$$\mathbf{y}_k = \mathbf{H}_k \mathbf{X}_k + \mathbf{v}_k, \quad (30)$$

$$\widehat{\mathbf{y}}_k = \mathbf{H}_k \widehat{\mathbf{X}}_k. \quad (31)$$

Substituting equations (30) and (31) into equation (29), we obtain the following equation:

$$\begin{aligned} \mathbf{P}_k^+ &= E \left[(\mathbf{X}_k - \widehat{\mathbf{X}}_k^- - \mathbf{K}_k (\mathbf{H}_k \mathbf{X}_k - \mathbf{H}_k \widehat{\mathbf{X}}_k^- + \mathbf{v}_k)) (\mathbf{X}_k - \widehat{\mathbf{X}}_k^- - \mathbf{K}_k (\mathbf{H}_k \mathbf{X}_k - \mathbf{H}_k \widehat{\mathbf{X}}_k^- + \mathbf{v}_k))^T \right] \\ &= (\mathbf{I} - \mathbf{K}_k \mathbf{H}_k) E \left[(\mathbf{X}_k - \widehat{\mathbf{X}}_k^-) (\mathbf{X}_k - \widehat{\mathbf{X}}_k^-)^T \right] (\mathbf{I} - \mathbf{K}_k \mathbf{H}_k)^T + \mathbf{K}_k E \left[\mathbf{v}_k \mathbf{v}_k^T \right] \mathbf{K}_k^T \\ &= (\mathbf{I} - \mathbf{K}_k \mathbf{H}_k) \mathbf{P}_k^- (\mathbf{I} - \mathbf{K}_k \mathbf{H}_k)^T + \mathbf{K}_k \mathbf{R}_k \mathbf{K}_k^T \\ &= (\mathbf{I} - \mathbf{K}_k \mathbf{H}_k) \mathbf{S}_k^T \mathbf{S}_k (\mathbf{I} - \mathbf{K}_k \mathbf{H}_k)^T + \mathbf{K}_k \sqrt{\mathbf{R}_k} \sqrt{\mathbf{R}_k}^T \mathbf{K}_k^T, \end{aligned} \quad (32)$$

where \mathbf{H}_k is the Jacobian matrix of the nonlinear function at the k th recursive step, and it is assumed that the measurement noise \mathbf{v}_k is unrelated to other quantities.

Third, utilizing the definition of cross-covariance and referring to equations (30) and (31), we deduce the following relationship:

$$\begin{aligned} \mathbf{P}_{xy,k} &= E \left[(\mathbf{X}_k - \widehat{\mathbf{X}}_k^-) (\mathbf{y}_k - \widehat{\mathbf{y}}_k)^T \right] \\ &= E \left[(\mathbf{X}_k - \widehat{\mathbf{X}}_k^-) (\mathbf{H}_k \mathbf{X}_k - \mathbf{H}_k \widehat{\mathbf{X}}_k^- + \mathbf{v}_k)^T \right] \\ &= E \left[(\mathbf{X}_k - \widehat{\mathbf{X}}_k^-) (\mathbf{X}_k - \widehat{\mathbf{X}}_k^-)^T \right] \mathbf{H}_k^T \\ &= \mathbf{P}_k^- \mathbf{H}_k^T = \mathbf{S}_k^T \mathbf{S}_k \mathbf{H}_k^T. \end{aligned} \quad (33)$$

The calculation method for obtaining \mathbf{H}_k from equation (33) is as follows:

$$\mathbf{H}_k = \mathbf{P}_{xy,k}^T \left((\mathbf{S}_k^T \mathbf{S}_k)^{-1} \right)^T = \mathbf{P}_{xy,k}^T (\mathbf{S}_k^T \mathbf{S}_k)^{-1}, \quad (34)$$

where equation (34) uses the property that the transposition of a symmetric matrix is equal to itself.

Finally, equations (18) and (19) can be replaced by the following expressions:

$$\mathbf{r}_3 = \text{qr} \left\{ (\mathbf{I} - \mathbf{K}_k \mathbf{H}_k) \mathbf{S}_k, \mathbf{K}_k \sqrt{\mathbf{R}_k} \right\}, \quad (35)$$

$$\mathbf{S}_k^+ = \mathbf{r}_3^T. \quad (36)$$

The calculation procedure of the MSUKF algorithm is as follows:

- (1) Initialization with equations (3) and (4)
- (2) Time update with equations (5)–(7) and (24) and (25)
- (3) Measurement prediction with equations (10)–(12), (26), (27), and (15)
- (4) Measurement update with equations (16), (17), (35), and (36)

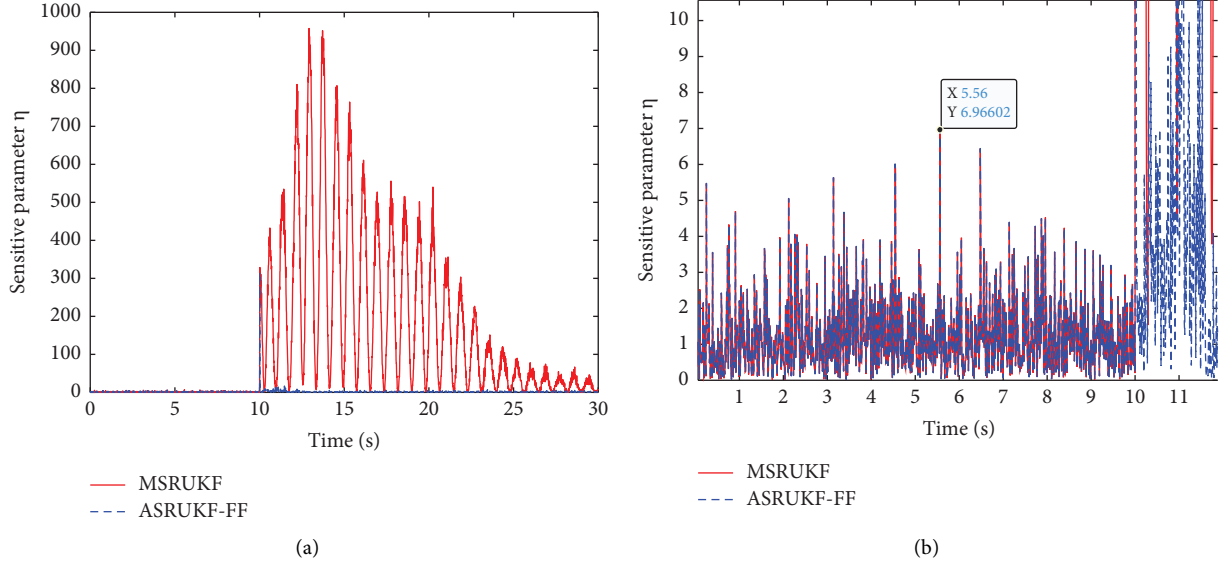


FIGURE 1: Comparison of time history curves for sensitivity parameters. (a) Time history curve of the sensitive parameter η and (b) local zoom of Figure 1(a).

2.3. The Adaptive Square Root UKF with Forgetting Factor.

Although the MSRUKEF algorithm alleviates the condition of requiring a positive-definite covariance matrix, ensuring numerical stability throughout the calculation process, its recursive nature still involves performing the UT to approximate the probability density distribution of the non-linear function. In each recursive step, the weight values of UT remain consistent, resulting in the data at each step exerting an identical impact on filtering. As the filtering progresses, the amount of acquired data steadily increases. However, the accumulation of older data diminishes the updating effect of new data on the estimates. Consequently, the state covariance matrix loses its corrective influence on the state vector, leading the filtering process to approach stability. Once the filtering reaches a state of stability, the state vector cannot be updated by new measurements. As a result, the MSRUKEF becomes incapable of tracking changes in the time-variant parameters.

To enhance the capability of the MSRUKEF algorithm in identifying time-variant parameters, this article proposes the following three steps for algorithm modification. First, drawing inspiration from the concept of utilizing a scalar in literature [1] to detect the occurrence of parameter changes, this paper also incorporates a scalar value, referred to as η (a sensitivity parameter), to pinpoint the moment of parameter change. The discrete form of η is depicted in the following:

$$\eta_k = \varepsilon_k^T (\mathbf{S}_{y,k}^T \mathbf{S}_{y,k})^{-1} \varepsilon_k, \quad (37)$$

where $\varepsilon_k = \mathbf{y}_k - \hat{\mathbf{y}}_k$, in which \mathbf{y}_k is the measurement at step k .

Second, a threshold value η_0 is introduced to intelligently trigger the adaptive algorithm when the sensitive parameter value η_t exceeds η_0 , where η_t denotes the value of the sensitive parameter at time instant t . The authors in the literature [1, 31, 47] suggest that η_0 follows a chi-square distribution with degrees of freedom equal to the number of measurements for zero-mean Gaussian innovation. However, in practice, η_0 remains interconnected with various factors, including measurement noise, modeling error covariance, measurement error covariance, initial state covariance, initial state vector, and sampling frequency. At times, relying solely on the number of measurements makes it challenging to calculate a reasonable η_0 . Considering the complexity and the involvement of multiple factors, it becomes difficult to calculate η_0 using a precise mathematical formula. Therefore, this paper proposes a more practical and reasonable approach to determine η_0 . It primarily involves the following three steps: (1) calculate the time history curve of η using MSRUKEF; (2) identify the maximum value η_t before the initial curve pulse emerges, for example, $\eta_t = 6.966$ at 10 s, as shown in Figure 1(b); and (3) set the threshold slightly higher than η_t , such as $\eta_0 = 7$ in Figure 1(b), and further refine if necessary. *Attention.* If the time history curve of η appears stable and it becomes challenging to determine the exact moment of parameter change, it indicates two possible situations: (1) the parameters may remain unchanged throughout the identification process and (2) the measurement noise is sufficiently high, making it difficult to discern the changes accurately.

Third, a forgetting factor α is defined, as shown in (38), where α belongs to the interval (0, 1) and “tr” represents the trace of the matrix. In contrast to the constant coefficient correction method suggested in [1, 12, 31, 47], the determination of the forgetting factor in this approach relies on the residual information at each recursive step. This adaptive approach enables the correction factor to be dynamically determined based on the uncertainty associated with each step.

$$\alpha_k = \begin{cases} 1, & \text{tr}(\varepsilon_k \varepsilon_k^T) \leq \text{tr}(\mathbf{S}_{y,k}^T \mathbf{S}_{y,k}), \\ \frac{\text{tr}(\mathbf{S}_{y,k}^T \mathbf{S}_{y,k})}{\text{tr}(\varepsilon_k \varepsilon_k^T)}, & \text{tr}(\varepsilon_k \varepsilon_k^T) > \text{tr}(\mathbf{S}_{y,k}^T \mathbf{S}_{y,k}). \end{cases} \quad (38)$$

Finally, leveraging the forgetting factor α , the update of the square root of the posterior state covariance matrix, as depicted in (36), is performed according to the following equation:

$$\mathbf{S}_k^+ = \frac{\mathbf{r}_3^T}{\sqrt{\alpha_k}}. \quad (39)$$

The specific algorithm flow of the ASRUKF-FF method is illustrated in Figure 2.

2.4. The Mathematical Explanation of the Forgetting Factor.

During the recursive process, the state covariance plays a crucial role in quantifying the level of uncertainty associated with the estimated state. A well-selected state covariance is a prerequisite for accurately identifying the time-variant parameters of the system. As discussed in Section 2.1, the initial state covariance can be set to a small value if the initial state values are highly reliable. However, if there is uncertainty in the initial state values, it should be chosen to be sufficiently large to encompass the actual state uncertainty. Furthermore, in the intermediate steps of the recursive process, a more precise estimation of the state covariance is required. Adjusting the state covariance appropriately can expedite the convergence to the correct value, as discussed in [1]. Therefore, the core principle of adaptive identification is to automatically adjust the state covariance by taking into account the forgetting factor and parameter sensitivity throughout the identification process.

To elucidate the origin of the forgetting factor, a mathematical explanation is provided based on the SRUKF method. When the structural parameters undergo changes during the identification process, it becomes necessary to expand the state covariance to encompass the uncertainty of the state [1]. Building upon this concept, a coefficient α is introduced, where $0 < \alpha < 1$. According to (18) and (19), the a posteriori estimate of the state covariance can be defined as follows:

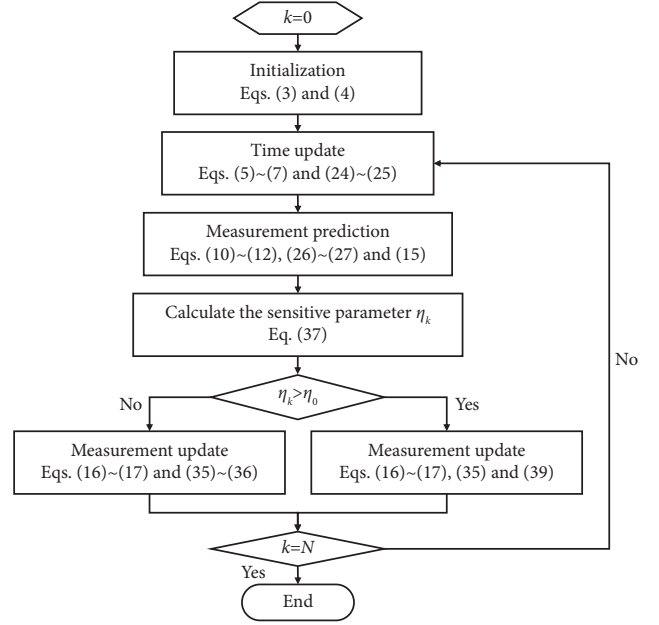


FIGURE 2: The algorithm flow of ASRUKF-FF.

$$\begin{aligned} \tilde{\mathbf{P}}_k^+ &= \frac{(\mathbf{S}_k^+)^T \mathbf{S}_k^+}{\alpha_k} \\ &= \frac{(\mathbf{S}_k^+)^T \mathbf{S}_k^+}{\sqrt{\alpha_k} \sqrt{\alpha_k}} \\ &= \frac{\mathbf{S}_k^T \mathbf{S}_k - \mathbf{K}_k \mathbf{S}_{y,k}^T \mathbf{S}_{y,k} \mathbf{K}_k^T}{\sqrt{\alpha_k} \sqrt{\alpha_k}} \\ &= \frac{\mathbf{S}_k^T \mathbf{S}_k}{\sqrt{\alpha_k} \sqrt{\alpha_k}} - \frac{\mathbf{K}_k \mathbf{S}_{y,k}^T \mathbf{S}_{y,k} \mathbf{K}_k^T}{\sqrt{\alpha_k} \sqrt{\alpha_k}}, \end{aligned} \quad (40)$$

where $\tilde{\mathbf{P}}_k^+$ is the posterior state covariance corrected by the forgetting factor, and the wave sign above the character represents the quantity corrected by the forgetting factor.

Substituting (16) into (40), we get the following equation:

$$\begin{aligned} \tilde{\mathbf{P}}_k^+ &= \frac{\mathbf{S}_k^T \mathbf{S}_k}{\sqrt{\alpha_k} \sqrt{\alpha_k}} - \mathbf{P}_{xy,k} (\mathbf{S}_{y,k}^T \mathbf{S}_{y,k})^{-1} \\ &\quad \cdot \frac{\mathbf{S}_{y,k}^T \mathbf{S}_{y,k}}{\sqrt{\alpha_k} \sqrt{\alpha_k}} \left(\mathbf{P}_{xy,k} (\mathbf{S}_{y,k}^T \mathbf{S}_{y,k})^{-1} \right)^T. \end{aligned} \quad (41)$$

Based on the identical equation principle, equation (41) can be modified as

$$\begin{aligned} \tilde{\mathbf{P}}_k^+ &= \frac{\mathbf{S}_k^T \mathbf{S}_k}{\sqrt{\tilde{\alpha}_k} \sqrt{\tilde{\alpha}_k}} - \frac{\mathbf{P}_{xy,k}}{\alpha_k} \left(\frac{\mathbf{S}_{y,k}^T \mathbf{S}_{y,k}}{\sqrt{\tilde{\alpha}_k} \sqrt{\tilde{\alpha}_k}} \right)^{-1} \\ &\quad \cdot \frac{\mathbf{S}_{y,k}^T \mathbf{S}_{y,k}}{\sqrt{\tilde{\alpha}_k} \sqrt{\tilde{\alpha}_k}} \left(\frac{\mathbf{P}_{xy,k}}{\alpha_k} \left(\frac{\mathbf{S}_{y,k}^T \mathbf{S}_{y,k}}{\sqrt{\tilde{\alpha}_k} \sqrt{\tilde{\alpha}_k}} \right)^{-1} \right)^T. \end{aligned} \quad (42)$$

Since the measurement noise is influenced by sensor accuracy and the testing environment, excessive noise can cause the identification process to diverge. Therefore, the measurement noise is not expanded. By utilizing equations (13) and (41)~(45), the following equation can be formed:

$$\begin{aligned} \tilde{\mathbf{P}}_{yy,k} &= \frac{\mathbf{S}_{y,k}^T \mathbf{S}_{y,k}}{\sqrt{\tilde{\alpha}_k} \sqrt{\tilde{\alpha}_k}} \\ &= \frac{\mathbf{P}_{yy,k}}{\alpha_k} \end{aligned} \quad (43)$$

$$= \frac{1}{\alpha_k} \sum_{j=0}^{2n} W_c^{(j)} (\hat{\mathbf{y}}_k^{(j)} - \hat{\mathbf{y}}_k) (\hat{\mathbf{y}}_k^{(j)} - \hat{\mathbf{y}}_k)^T + \mathbf{R}_k,$$

$$\begin{aligned} \tilde{\mathbf{P}}_{xy,k} &= \frac{\mathbf{P}_{xy,k}}{\alpha_k} \\ &= \frac{1}{\alpha_k} \sum_{j=0}^{2n} W_c^{(j)} (\hat{\mathbf{x}}_k^{(j)} - \hat{\mathbf{x}}_k) (\hat{\mathbf{y}}_k^{(j)} - \hat{\mathbf{y}}_k)^T, \end{aligned} \quad (44)$$

where $\mathbf{P}_{yy,k}$ is the innovation covariance matrix in the measurement update step of the conventional UKF method.

If the forgetting factor correction is not considered, equation (43) is mathematically equivalent to equations (13) and (14). The form of equation (43) is expressed to facilitate subsequent derivations.

Substituting equations (43) and (44) into equation (41), we get the following equation:

$$\tilde{\mathbf{P}}_k^+ = \frac{\mathbf{S}_k^T \mathbf{S}_k}{\sqrt{\tilde{\alpha}_k} \sqrt{\tilde{\alpha}_k}} - \frac{\tilde{\mathbf{K}}_k \mathbf{S}_{y,k}^T \mathbf{S}_{y,k} \tilde{\mathbf{K}}_k^T}{\sqrt{\tilde{\alpha}_k} \sqrt{\tilde{\alpha}_k}}, \quad (45)$$

where $\tilde{\mathbf{K}}_k = \tilde{\mathbf{P}}_{xy,k} (\tilde{\mathbf{P}}_{yy,k})^{-1}$.

The theoretical presentation above demonstrates that the ASRUKF-FF algorithm can be derived by combining the standard SRUKF with Equations (43)–(45). However, equation (45) poses challenges when applying it to the MSRUKF due to the altered calculation method for the posterior state covariance. The application of the forgetting factor to equation (35) requires additional mathematical derivation and verification, which will not be discussed in detail here. To elaborate on the origin of the forgetting factor, only equation (43) will be further discussed.

For further analysis, modify equation (43) as

$$\alpha_k (\tilde{\mathbf{P}}_{yy,k} - \mathbf{R}_k) = \sum_{j=0}^{2n} W_c^{(j)} (\hat{\mathbf{y}}_k^{(j)} - \hat{\mathbf{y}}_k) (\hat{\mathbf{y}}_k^{(j)} - \hat{\mathbf{y}}_k)^T. \quad (46)$$

Add \mathbf{R}_k to both sides of equation (46) and form as

$$\begin{aligned} \alpha_k (\tilde{\mathbf{P}}_{yy,k} - \mathbf{R}_k) + \mathbf{R}_k &= \mathbf{P}_{yy,k} \\ &= \mathbf{S}_{y,k}^T \mathbf{S}_{y,k}, \end{aligned} \quad (47)$$

$$\alpha_k (\tilde{\mathbf{P}}_{yy,k} - \mathbf{R}_k) = \mathbf{S}_{y,k}^T \mathbf{S}_{y,k} - \mathbf{R}_k. \quad (48)$$

Take the trace of equation (48) as

$$\alpha_k = \frac{\text{tr}(\mathbf{S}_{y,k}^T \mathbf{S}_{y,k} - \mathbf{R}_k)}{\text{tr}(\tilde{\mathbf{P}}_{yy,k} - \mathbf{R}_k)} \approx \frac{\text{tr}(\mathbf{S}_{y,k}^T \mathbf{S}_{y,k})}{\text{tr}(\tilde{\mathbf{P}}_{yy,k})}. \quad (49)$$

Note that equation (49) is an approximate forgetting factor due to the omission of \mathbf{R}_k . This operation makes sense as both the numerator and denominator contain the same covariance \mathbf{R}_k . Moreover, as the denominator of equation (49) emphasizes the impact of the new measurements, the corrected innovation covariance in the denominator is computed using the predicted measurement mean ($\hat{\mathbf{y}}_k$) and the actual measurements (\mathbf{y}_k). Therefore, equation (49) can be written as

$$\alpha_k = \frac{\text{tr}(\mathbf{S}_{y,k}^T \mathbf{S}_{y,k})}{\text{tr}(\varepsilon_k \varepsilon_k^T)}. \quad (50)$$

The mathematical derivation provided above allows us to obtain the rationale behind the forgetting factor and its application in the standard SRUKF form. While the MSRUKF has introduced changes in the calculation method for obtaining the square root of the posterior state covariance, as shown in equations (35) and (36), making it difficult to determine the exact location of the forgetting factor, we can still draw inspiration from equation (40). By correcting the square root of the posterior state covariance matrix, we can achieve the adaptive adjustment of the state covariance. In addition, due to the recursive calculation of the covariance in the MSRUKF method, the correction coefficient also necessitates the square root form of the forgetting factor, as demonstrated in equation (39).

3. Identification of Time-Variant Parameters of the Building Structure

3.1. The Three-Degree-of-Freedom Frame Model. The frame structure is a widely utilized construction system in civil engineering. In this section, a three-story frame structure is chosen as the subject of investigation to assess the performance and effectiveness of the proposed method. To facilitate the study, the actual frame structure is simplified into a shear model, as shown in Figure 3(a), where m_i , c_i , and k_i represent the mass, interlayer damping, and interlayer stiffness, respectively, for $i = 1, 2$, and 3 , and \ddot{x}_g represents the seismic excitation, and its time history curve is shown in Figure 3(b).

The equations of motion for this system can be derived from the interlayer responses, as described in reference [33]. Furthermore, to simulate real-world conditions, random noise is introduced into the measurements. The noise type is given as follows:

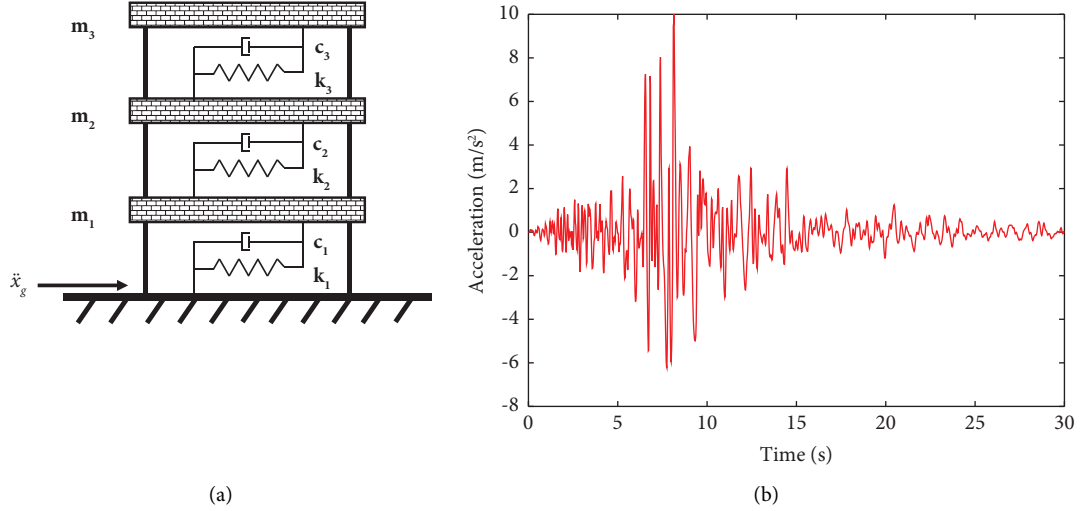


FIGURE 3: Information about the model and applied loads for structural analysis. (a) The three-story frame structure and (b) time history curve of seismic excitation.

TABLE 1: The initial state vector and state covariance.

Item	x_1	x_2	x_3	\dot{x}_1	\dot{x}_2	\dot{x}_3	k_1	k_2	k_3	c_1	c_2	c_3
\mathbf{X}_0	0	0	0	0	0	0	110	110	50	0.3	0.3	0.3
\mathbf{P}_0	$1e-8$	$1e-8$	$1e-8$	$1e-8$	$1e-8$	$1e-8$	$2e3$	$2e3$	$2e3$	0.1	0.1	0.1

Note. for convenience, dimensional units are omitted in Table 1 and x_i is the i th relative displacement, $i = 1, 2, \text{ and } 3$.

$$X_{\text{measurement}} = X_{\text{true}} + E_p N_{\text{noise}} \sigma(X_{\text{true}}), \quad (51)$$

where E_p is the percentage of the RMS noise; N_{noise} is a stochastic process following a standard normal distribution with zero mean and unit standard deviation; and σ is the standard deviation of the response without noise.

3.2. Time-Variant Stiffness and Damping Identification

3.2.1. The Effect Comparison of Different Algorithms. In this case study, the structural parameter values used are $m_1 = m_2 = m_3 = 1000$ kg, $k_1 = k_2 = 120$ kN/m, $k_3 = 60$ kN/m, and $c_1 = c_2 = c_3 = 0.6$ kNs/m. To depict the variations in parameters and evaluate the efficacy of identifying time-variant parameters, it is assumed that the stiffness parameters $k_1 \sim k_3$ undergo a sudden reduction to 80 kN/m, 80 kN/m, and 40 kN/m, respectively, at 10 s. Meanwhile, at 10 s, the damping parameters c_1 , c_2 , and c_3 are assumed to undergo a sudden change to 0.7 kNs/m, 0.65 kNs/m, and 0.65 kNs/m, respectively. The percentage of the RMS noise is 5%. The initial values of the state vector and state covariance are provided in Table 1. In addition, the covariance matrix \mathbf{Q} , representing the modeling error, is set to $1 \times 10^{-8} \mathbf{I}$, and the measurement error covariance matrix \mathbf{R} is set to $5 \times 10^{-2} \mathbf{I}$. Furthermore, in this section, the acceleration responses of the first, second, and third stories are considered as measurements. The sampling frequency is 100Hz.

Before applying the ASRUKF-FF approach, it is essential to establish a threshold for the sensitive parameter. The time history curve of this parameter, computed using both the

MSRUKF and ASRUKF-FF algorithms, is presented in Figure 1. As depicted in Figure 1(a), when structural parameters change, the time history curve of the sensitive parameter would exhibit a pulse response at the moment of change occurrence. Based on the calculation method proposed in Section 2.3 and the results shown in Figure 1(b), the threshold for the sensitive parameter can be determined as $\eta_0 = 7$. Furthermore, the ASRUKF-FF algorithm demonstrates its effectiveness in diminishing the impulse response of the sensitive parameter after 10 seconds. A lower value of the sensitive parameter indicates decreased uncertainty in the identification process, thus highlighting the enhanced accuracy of the ASRUKF-FF method.

To comprehensively demonstrate the effectiveness of the method proposed in this paper, a comparison is conducted between the ASRUKF-FF method and other existing methods, namely, the MSRUKF, adaptive UKF (AUKF) as described in literature [1], and modified strong tracking SRUKF (MSTSRUKF) as described in literature [33]. It is worth noting that the MSTSRUKF method requires the determination of a gradual forgetting factor ρ , typically satisfying $0 < \rho \leq 1$. The identification results of various algorithms are illustrated in Figure 4. Within the figure, the threshold β_0 for AUKF is determined as 16.3 using transcendental probability [1] and a gradual forgetting factor of 0.95 is applied to MSTSRUKF. For a detailed analysis of the errors in the final identification results, refer to Table 2.

Based on the analysis of Figure 4 and Table 2, the following conclusions can be drawn: (1) The MSRUKF method exhibits limited effectiveness in identifying time-variant parameters of

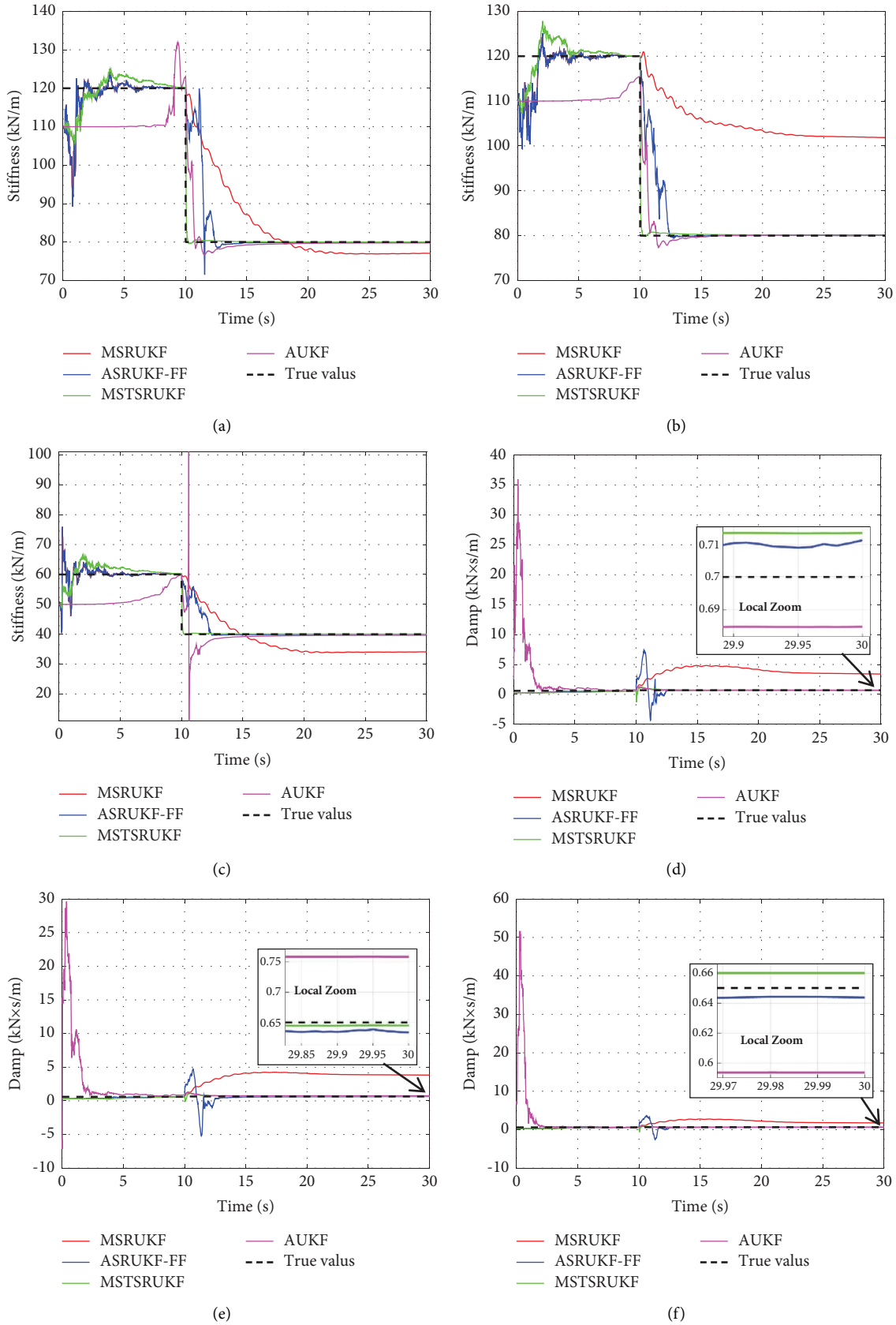


FIGURE 4: Results of parameter estimation using different algorithms: (a) the 1st-story stiffness, (b) the 2nd-story stiffness, (c) the 3rd-story stiffness, (d) the 1st-story damping, (e) the 2nd-story damping, and (f) the 3rd-story damping.

TABLE 2: Estimation errors of the final identification results based on different algorithms.

Algorithms	Error						
	k_1 (%)	k_2 (%)	k_3 (%)	c_1 (%)	c_2 (%)	c_3 (%)	
MSRUKF	-3.65	27.34	-14.71	387.88	489.68	169.98	
ASRUKF-FF	$\eta_0 = 7$	-0.07	0.07	-0.06	1.62	-2.58	-0.97
	$\eta_0 = 10$	-0.05	0.29	-0.37	1.83	0.54	-3.91
	$\eta_0 = 15$	-0.23	0.32	-0.29	-1.17	-6.56	2.83
	$\eta_0 = 16.3$	-0.09	0.15	-0.15	-0.86	-3.25	-0.39
	$\eta_0 = 20$	-0.07	0.07	-0.20	0.80	-2.96	-2.13
AUKF	$\beta_0 = 7$	-0.20	0.41	-0.07	-1.71	9.10	-2.02
	$\beta_0 = 16.3$	-0.29	0.20	-0.84	-2.19	16.59	-8.67
MSTSRUKF	$\rho = 0.95$	-0.01	0.15	0.17	1.94	-0.82	1.54
	$\rho = 0.96$	-0.01	0.16	0.17	1.95	-0.83	1.54
	$\rho = 0.99$	-0.01	0.16	0.16	1.96	-0.85	1.56

Note. Error = (identification value – true value)/true value \times 100%.

structures. It demonstrates issues of overconvergence (Figures 4(a) and 4(c)–4(f)) as well as underconvergence (Figure 4(b)). (2) The ASRUKF-FF method demonstrates a significant improvement in identification accuracy when the sensitive parameter threshold is set at $\eta_0 = 7$. It achieves a satisfactory identification effect with a maximum identification error of less than 3%. Furthermore, based on the damping identification results (Figures 4(d)–4(f)), the ASRUKF-FF method exhibits a tendency to generate pulse fluctuations precisely at the moment of structural parameter mutation. This characteristic can be utilized to estimate the exact timing of parameter changes. In comparison to other methods, the ASRUKF-FF algorithm exhibits the fastest convergence speed prior to parameter changes. (3) In the scenario, where the number of measurement values is 3 and the transcendental probability is set at 0.001, the threshold value of AUKF is calculated as $\beta_0 = 16.3$ using the chi-square inverse cumulative distribution function. However, it is observed that when β_0 is set to 16.3, the identification performance of AUKF is poor, resulting in a maximum error of 16.59% in the damping identification. By utilizing the threshold value $\beta_0 = 7$ calculated using the proposed method in Section 2.3, the identification effect of AUKF has significantly improved. Nevertheless, there is still a maximum error of 9.10%, and the convergence to the true values prior to parameter changes has not been achieved. In addition, when compared with the ASRUKF-FF and MSTSRUKF methods, the AUKF method exhibits slower convergence speed. (4) The MSTSRUKF method achieves a maximum identification error of 0.17% for stiffness and 1.94% for damping, aligning with the conclusion drawn in literature [33] that the identification error for stiffness and damping should not exceed 0.2% and 4%, respectively. Furthermore, as the literature [33] does not discuss the identification effect of different gradual forgetting factors, a brief discussion on the corresponding parameter ρ is presented here. Based on the findings in Table 2, it can be observed that the MSTSRUKF method is not significantly affected by variations in the gradual forgetting factor. The identification results remain relatively stable across different values of the parameter. (5) In terms of identification accuracy, both the

ASRUKF and MSTSRUKF methods have demonstrated excellent performance in this particular case.

To offer a more comprehensive explanation for the ASRUKF-FF algorithm's ability to identify time-variant parameters, an investigation was conducted on the time history curves of stiffness and damping parameters in the square root of the state covariance matrix (SRSCM). The comparative results of this study are presented in Figure 5, where the solid line denotes the outcomes computed by the MSRUKF algorithm and the dashed line represents the outcomes computed by the ASRUKF-FF algorithm. Figure 5 clearly indicates that the MSRUKF algorithm, lacking an adaptive function, mistakenly assumed that the identification result had converged to the true value at the time of parameter mutation (10 s). However, due to the failure to properly adjust the algorithm, the identification result was ultimately unsuccessful, as depicted in Figure 4. In contrast, the ASRUKF-FF algorithm effectively expands the SRSCM using the adaptive forgetting factor at the time of parameter change. This expansion increases the search threshold for the parameters to be identified, enabling the successful identification of time-variant parameters. Please note that due to the dynamic adjustment of the adaptive forgetting factor based on the residual information at each recursion step, the time history curves of stiffness or damping parameters in the SRSCM calculated using the ASRUKF-FF algorithm exhibit distinct peak pulses after the occurrence of parameter mutations. These peak pulses represent the results of different forgetting factor corrections.

3.2.2. Discussion on the Identification Effect of Different Sensitive Parameter Thresholds. This section discusses the identification effect of different sensitive parameter thresholds to demonstrate the stability and reliability of the proposed adaptive method. The comparative analysis adopts the control variable method, wherein all parameter settings remain the same as those in Section 3.2.1, except for the variation in sensitive parameter thresholds. This ensures a fair and controlled comparison of the results. The specific identification results are depicted in Figure 6, while the error analysis of the final identification values is presented in Table 2.

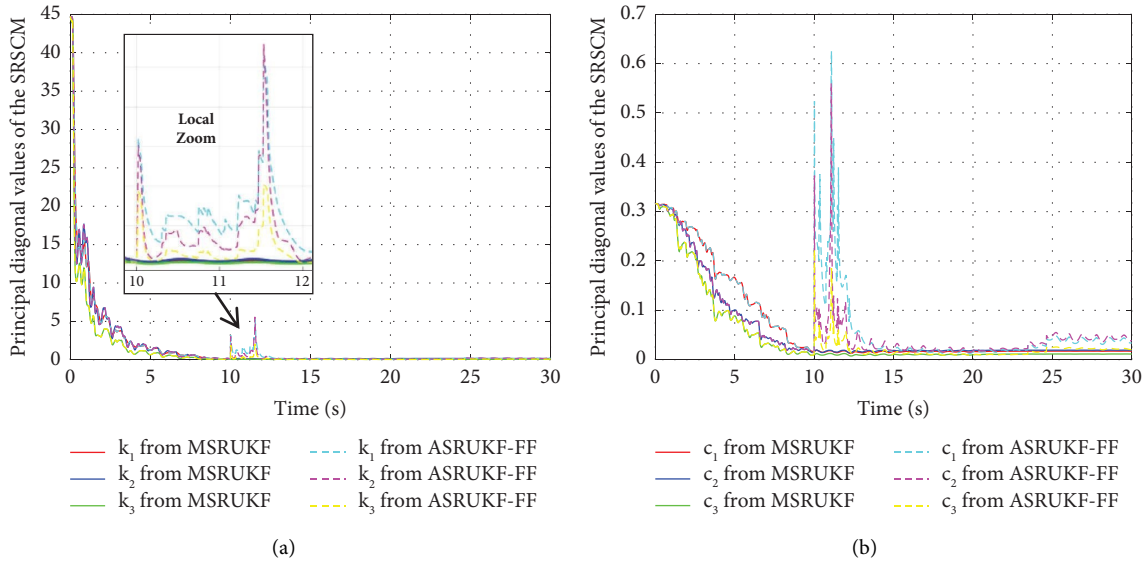


FIGURE 5: Time history curves of the principal diagonal elements in the SRSCM. (a) Time history curve of the stiffness parameter and (b) time history curve of the damping parameter.

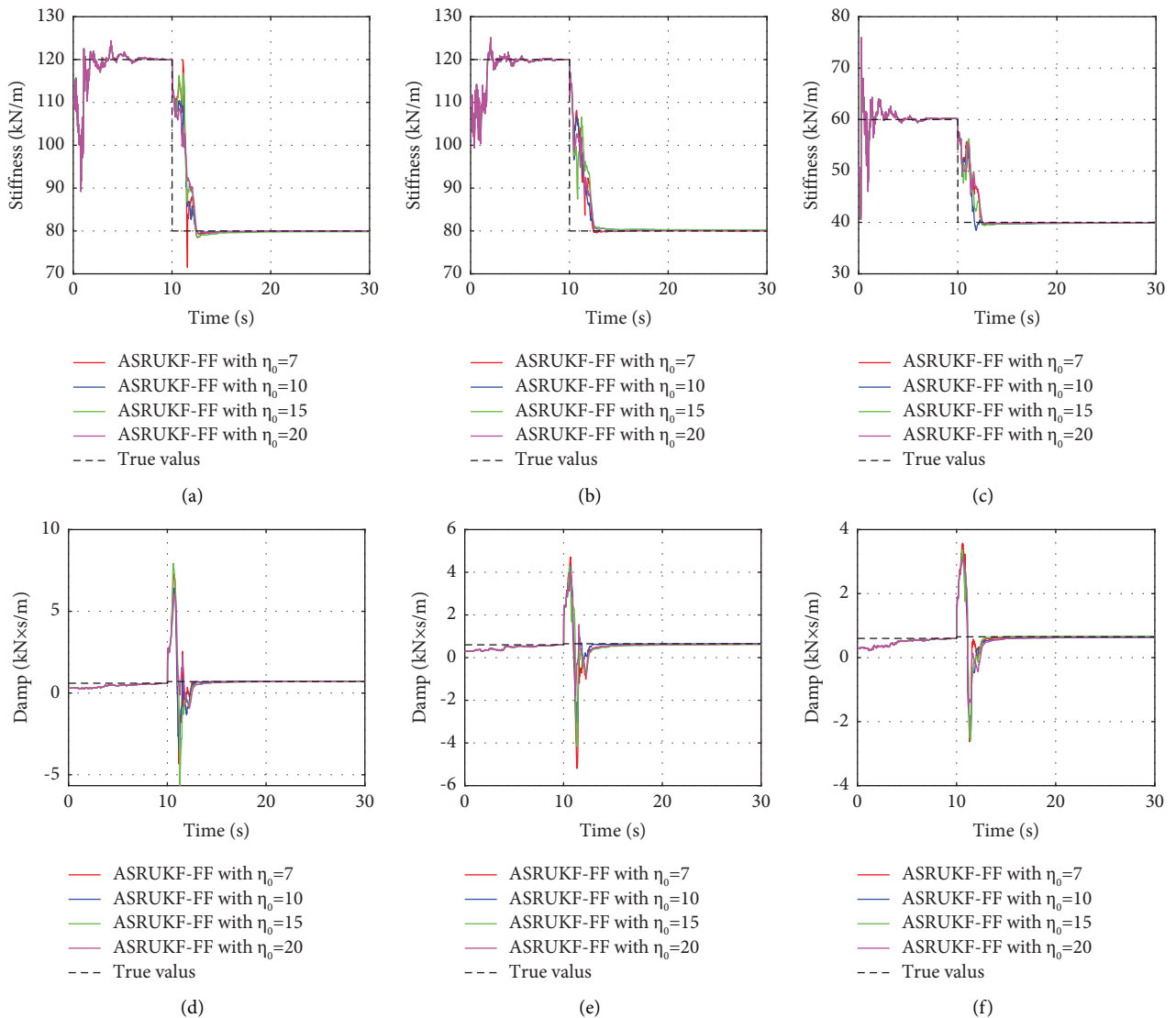


FIGURE 6: Identification performances of different sensitive parameter thresholds (5% noise level): (a) the 1st-story stiffness, (b) the 2nd-story stiffness, (c) the 3rd-story stiffness, (d) the 1st-story damping, (e) the 2nd-story damping, and (f) the 3rd-story damping.

As described in Section 2.3, the calculation method for the sensitivity parameter threshold involves selecting a value slightly larger than the maximum value before the initial pulse in the curve. Considering Figure 1, it can be observed that the threshold value of 20 is significantly higher than the maximum value of 6.966 (Figure 1(b)). Therefore, the range of sensitivity parameter thresholds discussed in this context varies from 7 to 20, with the maximum threshold being nearly three times higher than the minimum threshold. Analyzing Figure 6 and Table 2, it can be observed that the stiffness identification results remain consistent across different sensitive parameter thresholds. However, there are slight variations in the damping identification results. For instance, when the threshold value is set to 15, the maximum identification error for damping is 6.56%, whereas the identification errors for other thresholds do not exceed 4%. Moreover, it can be observed that when the threshold is set to 7, the proposed method exhibits a relatively high identification accuracy. This confirms the effectiveness of the proposed method as outlined in Section 2.3. Therefore, it is possible to choose a smaller threshold while ensuring the convergence of the algorithm. This can be done to improve the identification accuracy of the method. Although there may be slight variations in the identification results for different sensitive parameter thresholds, the overall accuracy of the estimation results remains high. This indicates the stability of the proposed algorithm in consistently producing reliable identification outcomes.

3.2.3. Discussion on the Identification Effect of the Values of \mathbf{X}_0 , \mathbf{P}_0 , \mathbf{Q} , and \mathbf{R} . The identification results are notably affected by the initial values of the state vector (\mathbf{X}_0), state covariance (\mathbf{P}_0), modeling error covariance (\mathbf{Q}), and measurement error covariance (\mathbf{R}). Thus, in this section, we explore the influence of different \mathbf{X}_0 , \mathbf{P}_0 , \mathbf{Q} , and \mathbf{R} values on the identification performance of time-variant structural parameters through the utilization of the ASRUKF-FF method. The comparative analysis employs the control variable method, where parameters other than the ones under study are set according to Section 3.2.1. Furthermore, the initial state variables, \mathbf{X}_0 and \mathbf{P}_0 , primarily consist of displacement, velocity, stiffness, and damping parameters. Typically, the initial displacement and velocity can be assumed to be zero, indicating relatively low uncertainty in these values. Conversely, the initial uncertainty associated with the stiffness and damping parameters is relatively high. Therefore, this section primarily focuses on the stiffness and damping parameters within \mathbf{X}_0 and \mathbf{P}_0 . The specific identification results are illustrated in Figures 7–10, while the final identification error is presented in Table 3.

Based on the analysis of the results in Figures 7–10 and Table 3, for the shear model, in comparison to the original intact state values of $[k_1, k_2, k_3, c_1, c_2, c_3] = [120, 120, 60, 0.6, 0.6, 0.6]$, as mentioned in the first paragraph of Section 3.2, when the stiffness and damping values in the state vector \mathbf{X}_0 are smaller $[50, 50, 10, 0.01, 0.015, 0.02]$ or larger $[220, 220, 220, 1.5, 1.5, 1.5]$, they exert a more significant influence on the accuracy of damping parameter identification. The corresponding maximum identification errors for the damping parameters are 5.9% and 3.7%, respectively. There are two possible reasons for this observation. First, stiffness plays a more significant role in

the response of the frame structure, and acceleration measurements are more sensitive to the identification of stiffness. Second, there is a disparity in numerical magnitudes between stiffness and damping. Hence, it is advisable to select more appropriate values for the stiffness and damping parameters in \mathbf{X}_0 , in order to mitigate the negative impact caused by excessively large or small initial values on the identification results. The values of the stiffness and damping parameters in the initial state covariance \mathbf{P}_0 have a significant influence on the accuracy of damping identification. For example, in the “[20000, 20000, 20000, 1, 1, 1]” operating condition, the maximum identification error for damping reaches 8.37%. Covariance represents the level of uncertainty in the data, and overestimating the degree of uncertainty can potentially impact the accuracy of identification. Furthermore, according to Figure 8, it can be inferred that appropriately increasing the values of the parameters to be identified in \mathbf{P}_0 helps speed up convergence and reduce the time required for the parameters to converge to their true values. The value of the modeling error covariance \mathbf{Q} has a significant impact on the identification of damping. While smaller \mathbf{Q} values may lead to higher accuracy in the final identification results, they might also result in slower convergence rates. In certain cases, the algorithm might not converge to the true parameter values before parameter mutations occur, as indicated by the red line in Figure 9. Furthermore, it is worth noting that the maximum identification error for damping is higher at $\mathbf{Q} = 1 \times 10^{-10} \mathbf{I}$ compared to $\mathbf{Q} = 1 \times 10^{-9} \mathbf{I}$. On the other side, as the value of \mathbf{Q} increases ($1 \times 10^{-9} \mathbf{I} \rightarrow 1 \times 10^{-8} \mathbf{I} \rightarrow 1 \times 10^{-7} \mathbf{I} \rightarrow 1 \times 10^{-6} \mathbf{I}$), the identification error for damping also progressively increases. The main reason behind this observation is that \mathbf{Q} serves as a compensation term for modeling errors. Overestimating the value of \mathbf{Q} can introduce larger model errors, which in turn can result in inaccurate parameter identification. Indeed, the measurement error covariance \mathbf{R} also plays a significant role in the identification of damping. \mathbf{R} value plays a crucial role in the measurement equation, and any underestimation or overestimation of its value can result in inaccurate estimation outcomes. Based on Table 3, it is evident that underestimating \mathbf{R} ($2 \times 10^{-2} \mathbf{I}$) has a more significant impact. Furthermore, despite the minimal impact of a lower \mathbf{R} value ($2 \times 10^{-2} \mathbf{I}$) on the final identification errors of structural stiffness parameters, it leads to a highly oscillatory identification process, as depicted by the red line in Figure 10. To summarize, variant \mathbf{X}_0 , \mathbf{P}_0 , \mathbf{Q} , and \mathbf{R} values have a negligible effect on the identification of stiffness parameters for frame structures. However, they exert a notable influence on the identification of damping, with \mathbf{R} having the most substantial impact. Furthermore, in terms of value rationality, smaller or larger values of \mathbf{X}_0 were not selected as the focus of the research.

3.2.4. Discussion on the Identification Effect of Different Measurements. This section primarily examines the impact of various measurement combinations on the identification outcomes. The control variable method is employed for conducting comparative analysis. The specific settings for algorithm parameters \mathbf{X}_0 , \mathbf{P}_0 , \mathbf{Q} , and \mathbf{R} can be found in Section 3.2.1, and the noise level is 5%. The sensitivity parameter thresholds may vary due to different measurement values.

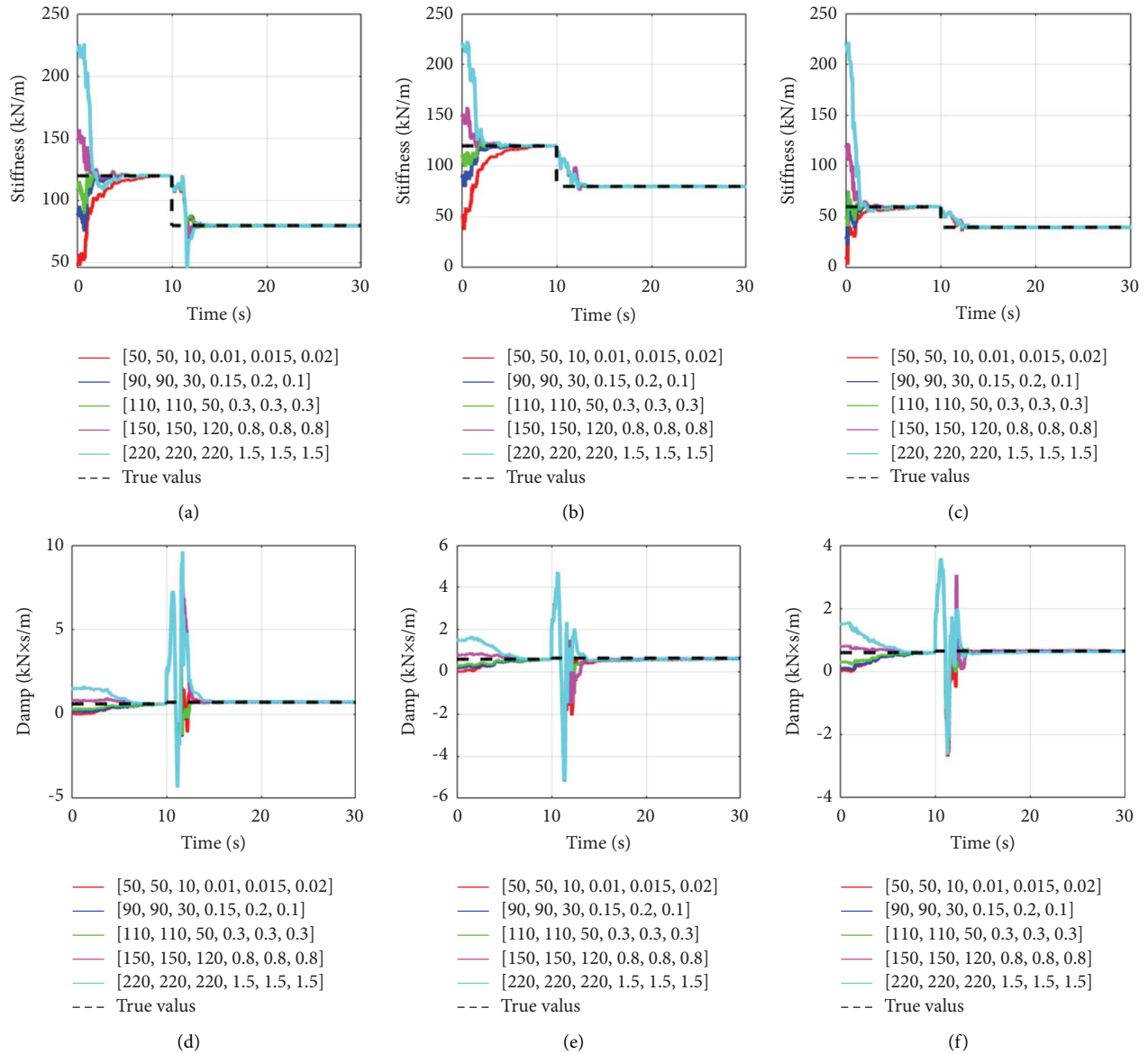


FIGURE 7: Identification results of different X_0 values (the legend values correspond to the initial values of stiffness and damping parameters, respectively; for example, the red line legend “[50, 50, 10, 0.01, 0.015, 0.02]” means $k_1 = 50$, $k_2 = 50$, $k_3 = 10$, $c_1 = 0.01$, $c_2 = 0.015$, and $c_3 = 0.02$): (a) the 1st-story stiffness, (b) the 2nd-story stiffness, (c) the 3rd-story stiffness, (d) the 1st-story damping, (e) the 2nd-story damping, and (f) the 3rd-story damping.

Therefore, the calculation process for each working condition is as follows: first, calculate the sensitivity parameter threshold using MSRUKEF; then, utilize the sensitive parameter threshold calculated in the previous step along with the ASRUKEF-FF algorithm to identify the structural parameters and record the identification results; finally, perform data processing, analysis, and summary. The specific identification results are depicted in Figure 11, while the comparison of identification errors in the final outcomes is presented in Table 4. The meanings of the labels in Figure 11 and Table 4 are explained as follows: (1) “ACC-1-2-3” indicates the utilization of all acceleration measurements, with a total of 3 measurements representing the accelerations of the first, second, and third stories, respectively. (2) “ACC-2 and DIS-1” signifies the simultaneous adoption of

acceleration and displacement as measurements, with the second-story acceleration and first-story displacement being specifically selected.

Based on the information presented in Figure 11 and Table 4, it can be concluded that when using a single measurement value (ACC-1, ACC-2, or ACC-3), the ASRUKEF-FF algorithm exhibits a noticeable identification error and fails to accurately identify all stiffness and damping parameters of the structure simultaneously. Nevertheless, it is observed that the identification effect for stiffness is superior to that of damping. In addition, the identification effect of “ACC-1” and “ACC-3” outperforms that of “ACC-2,” suggesting that using the acceleration measurements from the first or third story alone yields better identification

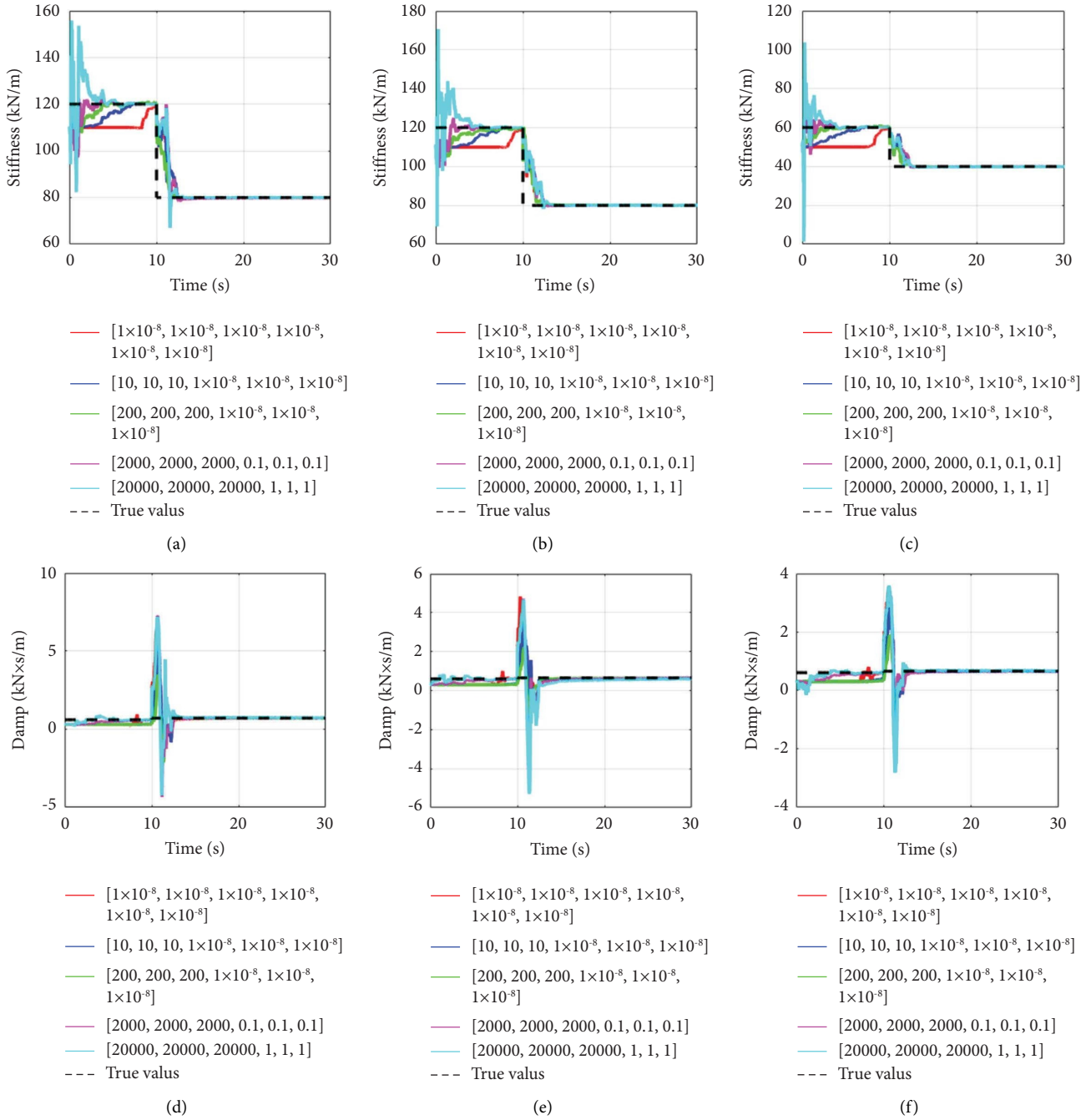


FIGURE 8: Identification results of different P_0 values (the legend values correspond to the initial covariance values of stiffness and damping parameters, respectively; for example, the blue line legend “[10, 10, 10, 1×10^{-8} , 1×10^{-8} , 1×10^{-8}]” means $P_{0_{k_1}} = 10$, $P_{0_{k_2}} = 10$, $P_{0_{k_3}} = 10$, $P_{0_{c_1}} = 1 \times 10^{-8}$, $P_{0_{c_2}} = 1 \times 10^{-8}$, $P_{0_{c_3}} = 1 \times 10^{-8}$): (a) the 1st-story stiffness, (b) the 2nd-story stiffness, (c) the 3rd-story stiffness, (d) the 1st-story damping, (e) the 2nd-story damping, and (f) the 3rd-story damping.

results compared to using the acceleration measurement from the second story alone. When two measurements are utilized, the identification performance of the ASRUKF-FF algorithm demonstrates a notable improvement compared to the case of using a single measurement value. Specifically, the “ACC-1-2” combination achieves better identification performance than the other two measurement combinations. Furthermore, upon comparing “ACC-2” and “ACC-2 and DIS-1,” it is observed that incorporating the first-story

displacement as an additional measurement can enhance the identification accuracy of the algorithm. In practical applications, direct measurement of displacement is feasible, such as utilizing ground-based radar with an accuracy of 0.1 mm [48]. Therefore, it is reasonable to include displacement as a measurement value. The details regarding displacement measurements will be thoroughly discussed in Section 4, while no in-depth research will be conducted in this section. In addition, considering the maximum

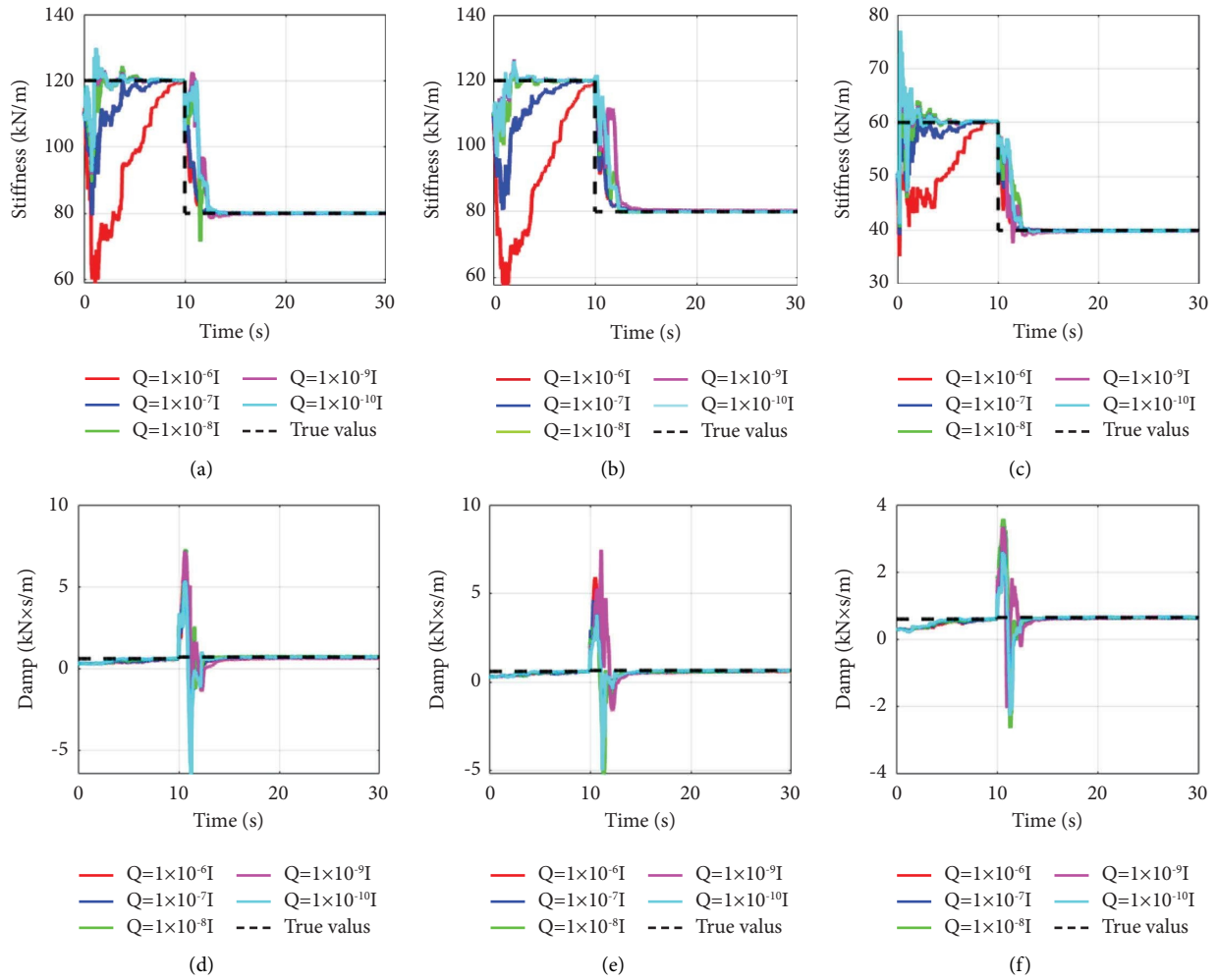


FIGURE 9: Identification results of different Q values. (a) The 1st-story stiffness, (b) the 2nd-story stiffness, (c) the 3rd-story stiffness, (d) the 1st-story damping, (e) the 2nd-story damping, and (f) the 3rd-story damping.

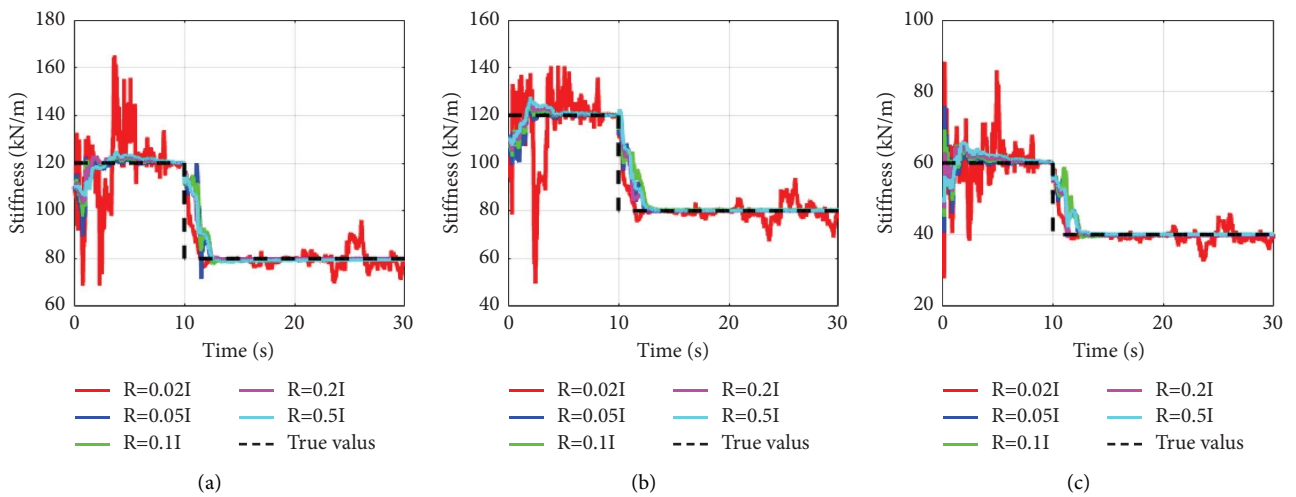


FIGURE 10: Continued.

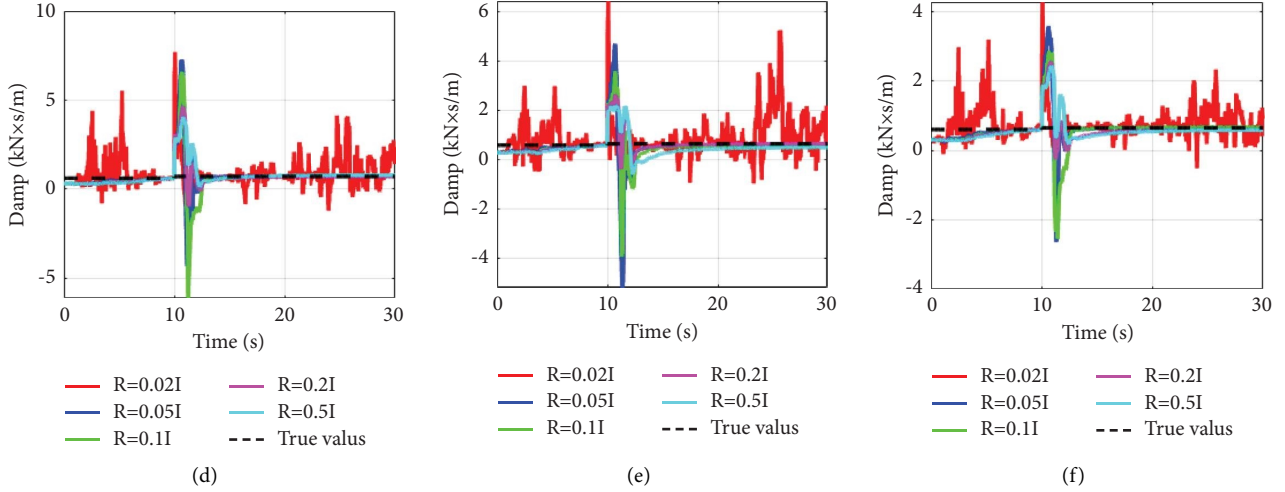


FIGURE 10: Identification results of different R values. (a) The 1st-story stiffness, (b) the 2nd-story stiffness, (c) the 3rd-story stiffness, (d) the 1st-story damping, (e) the 2nd-story damping, and (f) the 3rd-story damping.

TABLE 3: Estimation errors of the final identification results with different parameters.

Variant parameter	Parameter values	Identification error					
		k_1 (%)	k_2 (%)	k_3 (%)	c_1 (%)	c_2 (%)	c_3 (%)
X_0	[50, 50, 10, 0.01, 0.015, 0.02]	0.02	0.02	-0.11	2.53	-5.90	0.12
	[90, 90, 30, 0.15, 0.2, 0.1]	-0.07	0.06	-0.06	1.64	-2.63	-0.94
	[110, 110, 50, 0.3, 0.3, 0.3]	-0.07	0.07	-0.06	1.62	-2.58	-0.97
	[150, 150, 120, 0.8, 0.8, 0.8]	0.00	-0.07	0.08	0.92	-1.22	-0.92
	[220, 220, 220, 1.5, 1.5, 1.5]	0.04	-0.14	0.17	3.55	-3.10	-3.70
P_0	$[1 \times 10^{-8}, 1 \times 10^{-8}, 1 \times 10^{-8}, 1 \times 10^{-8}, 1 \times 10^{-8}, 1 \times 10^{-8}]$	-0.12	0.11	-0.05	-0.78	-0.57	-0.18
	$[10, 10, 10, 1 \times 10^{-8}, 1 \times 10^{-8}, 1 \times 10^{-8}]$	-0.01	0.04	-0.10	1.28	-0.72	-1.72
	$[200, 200, 200, 1 \times 10^{-8}, 1 \times 10^{-8}, 1 \times 10^{-8}]$	-0.05	0.11	-0.08	-0.17	-0.01	-0.76
	[2000, 2000, 2000, 0.1, 0.1, 0.1]	-0.07	0.07	-0.06	1.62	-2.58	-0.97
	[20000, 20000, 20000, 1, 1, 1]	-0.01	0.08	-0.13	3.58	-8.37	0.85
Q	$1 \times 10^{-10}I$	0.01	0.03	-0.12	0.63	-1.94	0.66
	$1 \times 10^{-9}I$	-0.11	0.29	-0.21	-1.07	-0.25	0.95
	$1 \times 10^{-8}I$	-0.07	0.07	-0.06	1.62	-2.58	-0.97
	$1 \times 10^{-7}I$	0.00	0.22	-0.05	-5.52	-3.60	-2.59
	$1 \times 10^{-6}I$	0.00	0.30	-0.06	-9.62	-8.43	-2.62
R	$2 \times 10^{-2}I$	-1.75	-1.09	-0.55	161.92	90.31	48.39
	$5 \times 10^{-2}I$	-0.07	0.07	-0.06	1.62	-2.58	-0.97
	$1 \times 10^{-1}I$	-0.20	0.33	-0.27	0.27	-6.28	1.97
	$2 \times 10^{-1}I$	-0.10	0.11	-0.22	1.11	0.58	-8.86
	$5 \times 10^{-1}I$	-0.67	0.31	0.30	11.00	-22.01	-10.35

identification error, the ranking of identification effects for the measurement combinations in Table 4 is as follows: ACC-1-2-3 > ACC-1-2 > ACC-2-3 > ACC-1-3 > ACC-2 and DIS-1 > ACC-1 > ACC-3 > ACC-2. This implies that utilizing three accelerations as measurement values yields the most favorable identification effect.

3.2.5. Discussion on the Identification Effect of Different Modeling Errors. This section examines the influence of parameter modeling errors on the performance of identification. Based on the model analysis presented in Section 3.1, the focus of this study is on the mass parameter, while the parameter settings for other variables are referenced from Section 3.2.1. Furthermore, different modeling errors

can also lead to variations in sensitivity parameter thresholds. Therefore, the specific implementation process is referenced from Section 3.2.4. It is worth noting that the measurement noise is set at 5%. The specific identification results are depicted in Figure 12, while the final identification error is presented in Table 5.

Based on the simulation analysis, it is found that the location of the maximum error for the stiffness parameter corresponds directly to the location of the mass change. This correlation can be visually observed from the light green or light blue cells in Table 5. However, there is no such relationship between the location of the maximum error for the damping parameter and the location of the mass change. Through the analysis of the simulation results for working

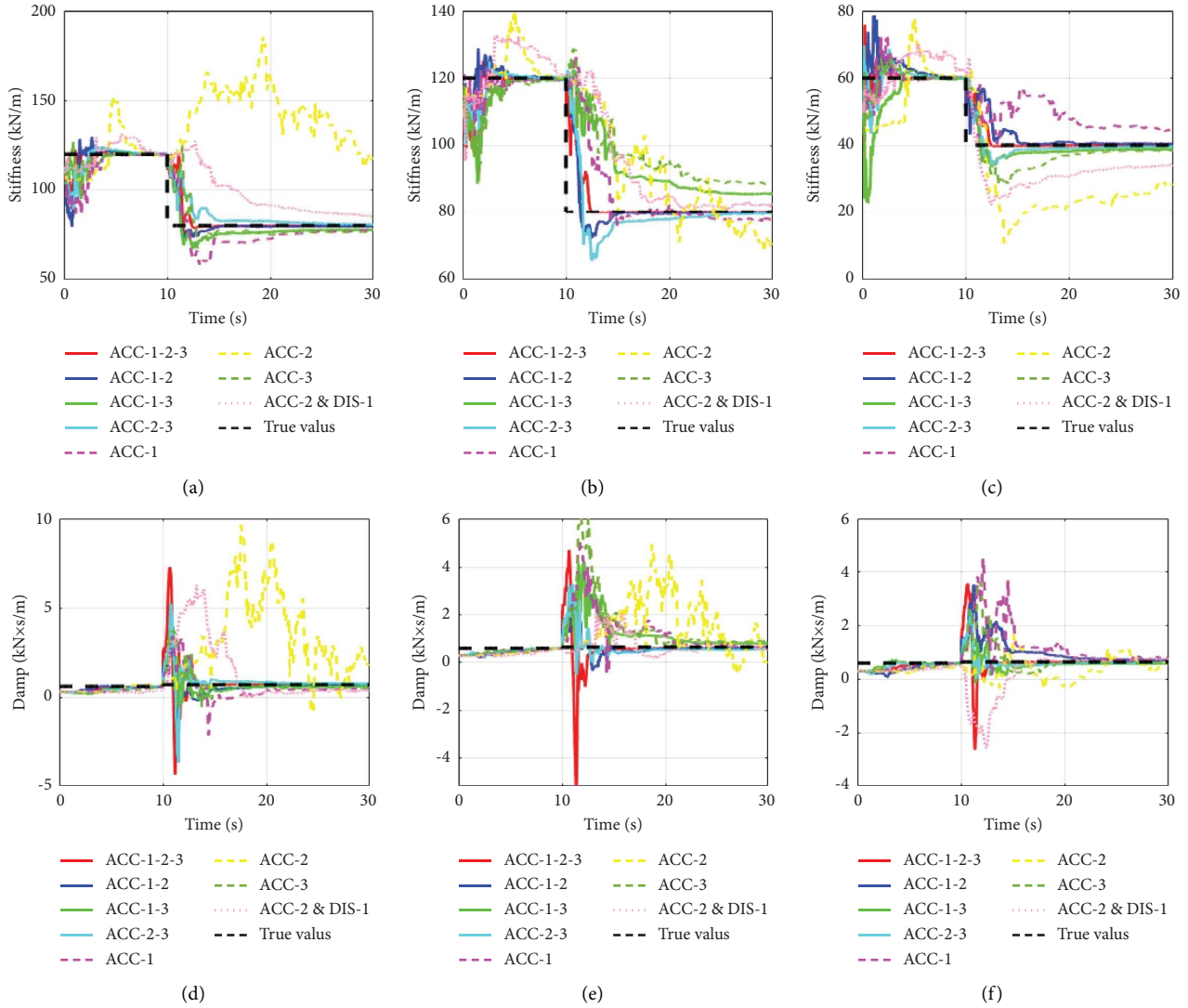


FIGURE 11: Identification effect of different measurements: (a) the 1st-story stiffness, (b) the 2nd-story stiffness, (c) the 3rd-story stiffness, (d) the 1st-story damping, (e) the 2nd-story damping, and (f) the 3rd-story damping.

TABLE 4: Estimation errors of the final identification results with different measurements based on the three-story frame structure.

Working condition	Type of measurements	Identification error					
		k_1 (%)	k_2 (%)	k_3 (%)	c_1 (%)	c_2 (%)	c_3 (%)
1	ACC-1-2-3	-0.07	0.07	-0.06	1.62	-2.58	-0.97
2	ACC-1-2	-0.23	-0.22	0.92	-7.97	-2.96	9.79
3	ACC-1-3	-2.91	7.02	-3.00	-14.40	24.21	-9.68
4	ACC-2-3	0.70	-0.57	-0.71	6.19	-10.70	-5.29
5	ACC-1	-2.84	-3.47	11.95	-33.71	3.29	25.07
6	ACC-2	46.87	-11.59	-29.19	168.82	-110.74	3.66
7	ACC-3	-4.25	10.68	-3.80	-26.17	39.12	-6.76
8	ACC-2 and DIS-1	6.56	3.18	-14.93	-54.59	-9.16	15.92

conditions 1 to 3, it is observed that the modeling error of the third-story mass parameter has the most significant impact on the identification outcomes. It is followed by the second-story mass parameter, while the modeling error of the first-story mass parameter has the least impact on the identification results. Furthermore, in working conditions 4 to 6, it

is observed that the simultaneous modeling error caused by the mass parameters of the second and third stories leads to the poorest identification effect. Through the analysis of the simulation results for working conditions 7 to 9, it is observed that the higher the uncertainty of the mass parameter, the larger the error in parameter identification. This

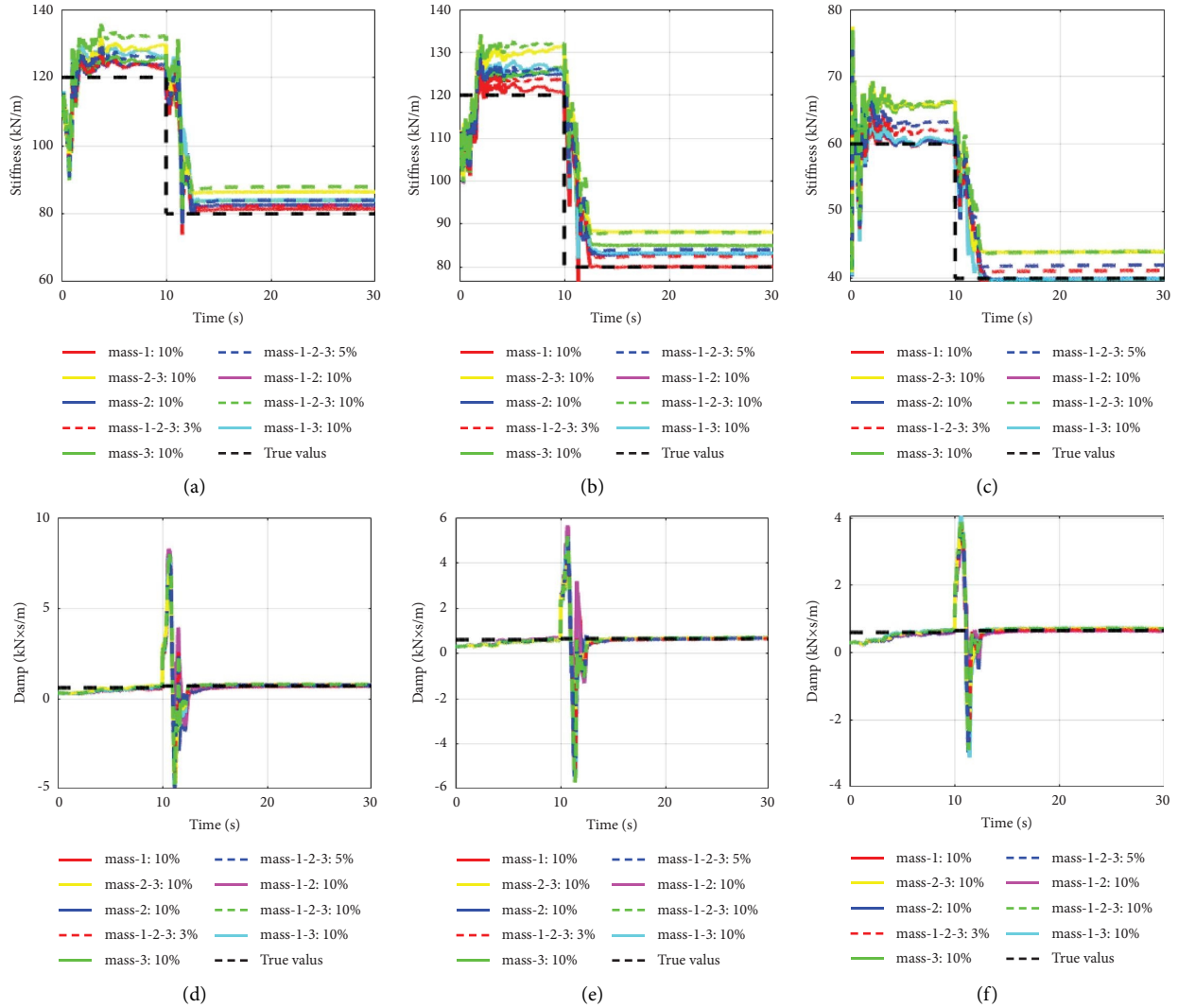


FIGURE 12: Identification effect with different mass modeling errors (explanation of legend characters, “mass 1: 10%” indicates a modeling error of 10% existing in the mass of the first story; “mass 1-2: 10%” indicates a modeling error of 10% existing in the mass of the first and second stories, respectively): (a) the 1st-story stiffness, (b) the 2nd-story stiffness, (c) the 3rd-story stiffness, (d) the 1st-story damping, (e) the 2nd-story damping, and (f) the 3rd-story damping.

indicates a positive correlation between the mass parameter and the identification of the stiffness and damping parameters in the shear model. In summary, for this case study, when the mass parameter has a modeling error of 10%, the maximum identification errors for the structural stiffness and damping parameters are 10.07% and 11.71%, respectively.

4. Identification of Time-Variant Stiffness of the Bridge

4.1. Vehicle Bridge System. To the best of the author’s knowledge, there are few cases of directly identifying the time-variant stiffness of bridges using methods related to the UKF. Hence, to thoroughly demonstrate the effectiveness of the proposed method, this section selects a simply supported bridge as the object of verification. To simplify the

calculation process and improve the computation efficiency, the bridge structure is simulated using a beam model. The purpose is to determine the stiffness parameters of the bridge by the vehicle bridge interaction force when the vehicle crosses the bridge.

The bridge section is assumed to be constant, as illustrated in Figure 13. The specific parameters are bridge span $L = 21$ m, cross-sectional area $A = 1.2$ m², section moment of inertia $I = 0.12$ m⁴, elastic modulus $E = 2.4 \times 10^4$ MPa, and density $\rho = 2000$ kg/m³. Furthermore, pavement roughness is taken into consideration and is characterized by random numbers following a normal distribution.

The finite element model of the bridge is constructed using Euler–Bernoulli beam elements, which are divided into six elements, represented as beams ① to ⑥ in Figure 13. The stiffness and mass matrices of the beam element are given in the following equations, respectively:

TABLE 5: Final identification errors with different mass modeling errors.

Working condition	Uncertain parameter	Modeling error (%)	Identification error					
			k_1 (%)	k_2 (%)	k_3 (%)	c_1 (%)	c_2 (%)	c_3 (%)
1	Mass-1		1.75	0.07	-0.16	-2.35	3.58	0.04
2	Mass-2		3.18	3.92	-0.01	1.86	5.76	0.07
3	Mass-3		4.88	6.22	9.96	5.44	2.99	8.96
4	Mass-1-2	10	4.99	4.00	-0.15	4.43	6.65	-1.53
5	Mass-1-3		6.73	6.17	9.88	5.31	5.84	9.59
6	Mass-2-3		8.09	10.18	9.92	10.57	5.22	9.23
7	Mass-1-2-3	3	2.93	3.07	2.94	4.67	0.31	2.03
8	Mass-1-2-3	5	4.93	5.07	4.94	6.69	2.28	4.02
9	Mass-1-2-3	10	9.92	10.07	9.93	11.71	7.22	9.01

Note. (1) Cell data with light green and light blue backgrounds represent the maximum error and the first two maximum errors of stiffness parameters in each row, respectively. (2) Cell data with orange and yellow backgrounds represent the maximum error and the first two maximum errors of damping parameters in each row, respectively. (3) A modeling error represents an increase in the parameter. If the true parameter value is 10, considering a modeling error of 5%, the parameter value becomes $10 \times (1 + 5\%)$.

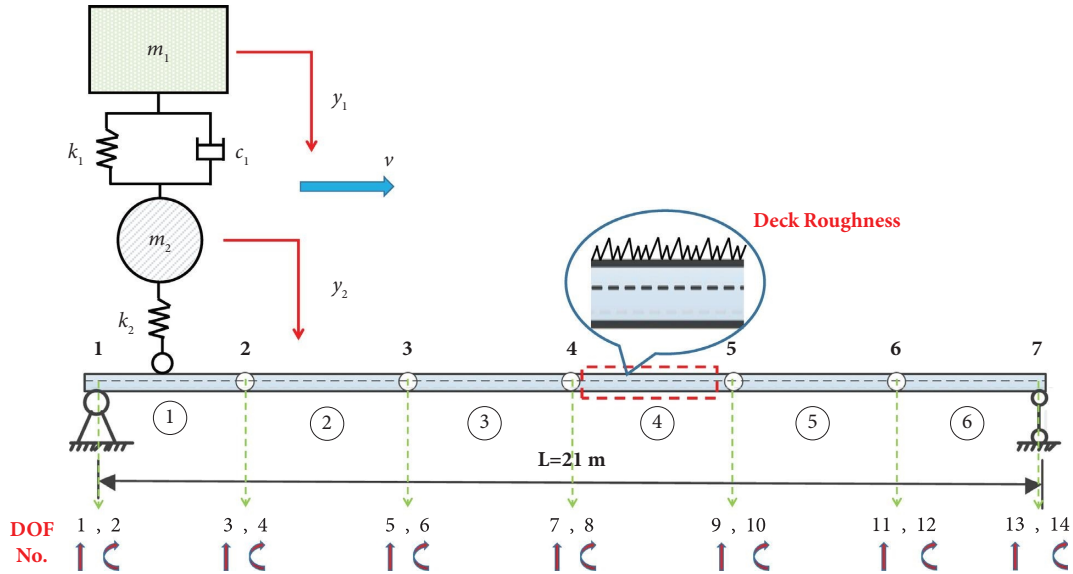


FIGURE 13: The simplified model of the vehicle bridge system (VBS).

$$\mathbf{K}^e = \int_{x_i}^{x_j} \mathbf{B}^T \mathbf{E} \mathbf{I} \mathbf{B} dx, \quad (52)$$

$$\mathbf{M}^e = \int_{x_i}^{x_j} \mathbf{N}^T \rho \mathbf{A} \mathbf{N} dx, \quad (53)$$

where \mathbf{M}^e and \mathbf{K}^e are the element mass and stiffness matrices, respectively; x_i and x_j represent the starting and ending coordinate of one element; \mathbf{N} is the shape function of element i ; and \mathbf{B} is the strain matrix of element i . The specific expression of \mathbf{N} and \mathbf{B} is given in the following equations:

$$\mathbf{N} = [1 - 3\xi^2 + 2\xi^3, l_i \xi (1 - \xi)^2, \xi^2 (3 - 2\xi), -l_i \xi^2 (1 - \xi)], \quad (54)$$

$$\begin{aligned} \mathbf{B} &= \frac{d^2 \mathbf{N}}{dx^2} \\ &= \frac{1}{l_i^2} [-6 + 12\xi, l_i (-4 + 6\xi), 6 - 12\xi, l_i (-2 + 6\xi)], \end{aligned} \quad (55)$$

where ξ is a scalar and $\xi = x/l_i$, x is the distance the vehicle moves on a beam element, and l_i is the length of element i .

The quarter-car model is generally used to demonstrate the theoretical basis of the vehicle bridge interaction model [49, 50] and has been successfully applied to numerous applications [51–53]. Therefore, a moving quarter-car model is chosen as the external excitation for the analysis. The vehicle system has two degrees of freedom (Figure 13), including the body mass $m_1 = 3.6 \times 10^4$ kg, bogie mass $m_2 = 2.5 \times 10^2$ kg, secondary suspension stiffness $k_1 = 6.0 \times 10^5$ N/m, secondary suspension damping $c = 1.0 \times 10^3$ Ns/m, and primary suspension stiffness $k_2 = 8.5 \times 10^5$ N/m. The moving speed is $v = 30.24$ km/h.

Based on the coupling relationship between contact force and displacement, the equations of motion for the VBS are formulated as

$$\mathbf{M}\ddot{\mathbf{U}}(t) + \mathbf{C}\dot{\mathbf{U}}(t) + \mathbf{K}\mathbf{U}(t) = \mathbf{F}(t), \quad (56)$$

where

$$\begin{aligned} \mathbf{M} &= \begin{bmatrix} \mathbf{M}_b & \mathbf{L}^T m_1 & \mathbf{L}^T m_2 \\ 0 & m_1 & 0 \\ 0 & 0 & m_2 \end{bmatrix}, \\ \mathbf{C} &= \begin{bmatrix} \mathbf{C}_b & 0 & 0 \\ 0 & c & -c \\ 0 & -c & c \end{bmatrix}, \\ \mathbf{K} &= \begin{bmatrix} \mathbf{K}_b & 0 & 0 \\ 0 & k_1 & -k_1 \\ -k_2 \mathbf{L} & -k_1 & k_1 + k_2 \end{bmatrix}, \\ \mathbf{F} &= \begin{bmatrix} \mathbf{L}^T [(m_1 + m_2)g] \\ 0 \\ k_2 r(x(t)) \end{bmatrix}, \\ \mathbf{U}(t) &= \begin{bmatrix} \mathbf{u}_b(t) \\ y_1(t) \\ y_2(t) \end{bmatrix}, \end{aligned} \quad (57)$$

\mathbf{M}_b , \mathbf{K}_b , and \mathbf{C}_b are the mass, stiffness, and damping matrices of the bridge, respectively; \mathbf{u}_b is the displacement vector of the bridge; \mathbf{L} is the mapping matrix for the input force, such as $\mathbf{L} = [0, 0, \dots, \mathbf{N}_i(t), \dots, 0, 0]^T$; y_1 is the vertical displacement of the vehicle body; y_2 is the vertical displacement of the vehicle bogie; and $r(x(t))$ is the pavement roughness at position $x(t)$ which is the vehicle position at time t .

In this case study, the Rayleigh damping is selected as

$$\mathbf{C}_b = a_1 \mathbf{M}_b + a_2 \mathbf{K}_b, \quad (58)$$

$$\begin{bmatrix} a_1 \\ a_2 \end{bmatrix} = 2 \frac{\omega_m \omega_n}{\omega_n^2 - \omega_m^2} \begin{bmatrix} \omega_n & -\omega_m \\ -1 & 1 \\ \omega_n & \omega_m \end{bmatrix} \begin{bmatrix} \tau_m \\ \tau_n \end{bmatrix}, \quad (59)$$

where a_1 and a_2 are the Rayleigh damping coefficients of the structure, respectively; ω_m and ω_n represent the m th and n th modal circular frequencies of the structure, respectively; and τ_m and τ_n are the m th and n th modal damping ratios, respectively. In this simulation, take $\tau_m = \tau_n = 0.015$, $\omega_m = \omega_1$, and $\omega_n = \omega_2$.

4.2. Time-Variant Stiffness Parameters Identification

4.2.1. The Effect Comparison of Different Algorithms. In this case study, it is assumed that the stiffness of the ② to ⑤ beam elements of the bridge is unknown. It is further assumed that the ② and ③ beam elements exhibit gradual and abrupt changes, respectively. In addition, the beam stiffness is assumed to be solely dependent on the elastic modulus. The specific parameter changes are illustrated in Table 6.

Because each element of the Euler–Bernoulli beam has 2 nodes and each node has 2 degrees of freedom, the total number of degrees of freedom of the bridge is $n = 14$. As there are four elastic modulus parameters to be identified, the state vector is chosen to be of order $(2n + m)$. The state vector can be written as

$$\begin{aligned} \dot{\mathbf{X}}(t) &= \begin{bmatrix} \dot{\mathbf{u}}_b(t) \\ \ddot{\mathbf{u}}_b(t) \\ \dot{\mathbf{E}} \end{bmatrix} \\ &= \begin{bmatrix} \dot{\mathbf{u}}_b(t) \\ \mathbf{M}_b^{-1} [\mathbf{L}\mathbf{F}_{\text{int}}(t) - \mathbf{C}_b \dot{\mathbf{u}}_b(t) - \mathbf{K}_b \mathbf{u}_b(t)] \\ \mathbf{0}_{4 \times 1} \end{bmatrix}, \end{aligned} \quad (60)$$

where subscript “ $p \times q$ ” represents a vector or matrix with p row(s) and q column(s) and the quantities appearing in the equation are defined as

$$\begin{aligned} \mathbf{X}(t) &= \begin{bmatrix} \mathbf{u}_b(t) \\ \dot{\mathbf{u}}_b(t) \\ \mathbf{E} \end{bmatrix}, \\ \mathbf{E} &= \begin{bmatrix} E_2 \\ E_3 \\ E_4 \\ E_5 \end{bmatrix}, \\ \mathbf{u}_b &= [u_{b1} \ u_{b2} \ u_{b3} \ u_{b4} \ u_{b5} \ u_{b6} \ u_{b7} \ u_{b8} \ u_{b9} \ u_{b10} \ u_{b11} \ u_{b12} \ u_{b13} \ u_{b14}]^T. \end{aligned} \quad (61)$$

TABLE 6: Time-variant stiffness parameters and comparison methods.

E_4, E_5 (1×10^{10} Pa)	E_2 (1×10^{10} Pa)	E_3 (1×10^{10} Pa)	Comparison methods
2.4	$E_2 = \begin{cases} 2.4 & 0 \leq t \leq 0.8 \\ 4.96 - 3.2t & 0.8 < t < 1.1 \\ 1.44 & 1.1 \leq t \leq 2.5 \end{cases}$	$E_3 = \begin{cases} 2.4 & 0 \leq t \leq 0.8 \\ 1.56 & 0.8 \leq t \leq 2.5 \end{cases}$	MSRUKF AUKF ASRUKF-FF MSTRUKF

In this case study, it is observed that using displacements as measurements yields better results. Therefore, the vertical displacements of nodes 2, 3, 4, 5, and 6, as shown in Figure 13, are selected as the measurements. The measurement equation can be expressed as follows:

$$\begin{aligned} \mathbf{Y} &= [y_1 \ y_2 \ y_3 \ y_4 \ y_5]^T \\ &= [u_{b3} \ u_{b5} \ u_{b7} \ u_{b9} \ u_{b11}]^T. \end{aligned} \quad (62)$$

$$\begin{aligned} \hat{\mathbf{X}}_0^+(t) &= \begin{bmatrix} \mathbf{u}_b(t) \\ \dot{\mathbf{u}}_b(t) \\ E_2 \\ E_3 \\ E_4 \\ E_5 \end{bmatrix}, \\ &= \begin{bmatrix} \mathbf{0}_{1 \times 14} \\ \mathbf{0}_{1 \times 14} \\ 0.264 \\ 0.264 \\ 0.264 \\ 0.264 \end{bmatrix}, \\ \hat{\mathbf{P}}_0^+ &= \begin{bmatrix} 1 \times 10^{-8} \text{diag}(14) & \mathbf{0}_{14 \times 1} & \mathbf{0}_{14 \times 1} & \mathbf{0}_{14 \times 1} & \mathbf{0}_{14 \times 1} & \mathbf{0}_{14 \times 1} \\ \mathbf{0}_{14 \times 14} & 1 \times 10^{-8} \text{diag}(14) & \mathbf{0}_{14 \times 1} & \mathbf{0}_{14 \times 1} & \mathbf{0}_{14 \times 1} & \mathbf{0}_{14 \times 1} \\ \mathbf{0}_{1 \times 14} & \mathbf{0}_{1 \times 14} & 1 \times 10^{-2} & 0 & 0 & 0 \\ \mathbf{0}_{1 \times 14} & \mathbf{0}_{1 \times 14} & 0 & 1 \times 10^{-2} & 0 & 0 \\ \mathbf{0}_{1 \times 14} & \mathbf{0}_{1 \times 14} & 0 & 0 & 1 \times 10^{-2} & 0 \\ \mathbf{0}_{1 \times 14} & \mathbf{0}_{1 \times 14} & 0 & 0 & 0 & 1 \times 10^{-2} \end{bmatrix}, \end{aligned} \quad (63)$$

where the initial values of E_2 to E_5 are set to 0.264, respectively, to reduce the difference in the order of magnitude between state variables; however, the corresponding missing order of magnitude should be considered when solving the actual equation; $1 \times 10^{-8} \text{diag}(14)$ represents a diagonal matrix with the order of 14 and the diagonal elements are all 1×10^{-8} .

In this section, the RMS noise percentage is set to 2%, and the sampling frequency is 100Hz. The threshold β_0 of the AUKF is calculated as 21 using transcendental probability [1]. In addition, the gradual forgetting factor of the MSTSRUKF is set to 0.95. The identification results of different algorithms are shown in Figure 14, and the error analysis of the final identification results is described in Table 7.

Based on Figure 14 and Table 7, it can be observed that the MSRUKF method is unable to accurately identify the time-variant parameters of the beam structure, resulting in a maximum identification error of 77.63%. The MSTSRUKF method demonstrates a better identification effect on time-variant parameters compared to constant parameters. The

The modeling error covariance matrix \mathbf{Q} is set as $1 \times 10^{-8} \mathbf{I}$, and the measurement error covariance matrix \mathbf{R} is set as $1 \times 10^{-8} \mathbf{I}$. Furthermore, the initial state vector and covariance are given by

maximum error in time-variant parameter identification is 6.2%, while the maximum error in constant parameter identification is 16.67%. Furthermore, the identification process of MSTSRUKF exhibits nonsmoothness and significant fluctuations. The AUKF and ASRUKF-FF methods exhibit satisfactory performance in identifying time-variant parameters of beam structures, with a maximum identification error of no more than 3%. However, the ASRUKF-FF method achieves higher accuracy in identifying time-variant parameters.

4.2.2. Algorithm Robustness Analysis. To evaluate the robustness of the algorithm and its adaptability to larger uncertainties, the noise level is increased to 5% in this section, while keeping the other parameters the same as in Section 4.2.1. Due to the difficulty of achieving convergence with the MSTSRUKF method in the presence of high levels of noise in the vehicle bridge system, the remaining three algorithms are compared in this scenario. In addition, it is important to note that when the noise level is set to 5%, the AUKF algorithm

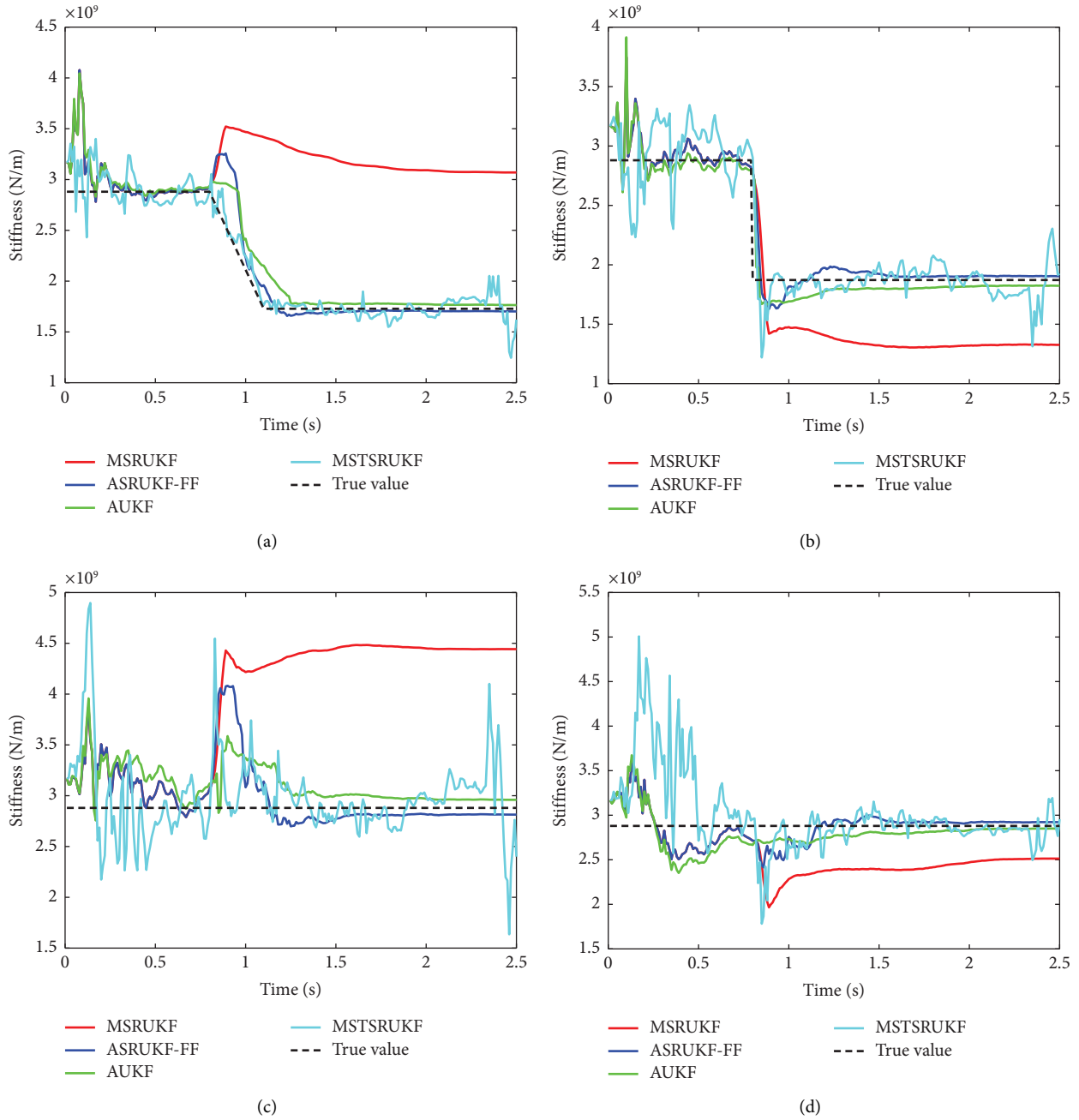


FIGURE 14: Identification effect of different algorithms: (a) the stiffness of beam ②, (b) the stiffness of beam ③, (c) the stiffness of beam ④, and (d) the stiffness of beam ⑤.

TABLE 7: Estimation errors of the final identification results with 2% noise.

Algorithms	Stiffness identification error			
	Beam ② (%)	Beam ③ (%)	Beam ④ (%)	Beam ⑤ (%)
MSRUKF	77.63	-29.13	54.26	-12.74
ASRUKF-FF	-1.53	1.73	-2.31	1.47
AUKF	2.10	-2.56	2.75	-1.04
MSTSRUKF	-6.20	2.88	-16.67	2.60

Note. Stiffness identification error = (identification value - true value)/true value × 100%.

cannot use a threshold $\beta_0 = 21$ to complete the identification task, and a low threshold value would cause identification divergence. Hence, in this analysis section, the AUKF algorithm utilizes the threshold calculated through the method proposed in this article to accomplish the identification of stiffness parameters. The specific identification results are presented in Figure 15, and a detailed error analysis of the final identification results is provided in Table 8.

From Figure 15 and Table 8, it is evident that as the system uncertainty increases, the maximum error of the MSUKF method in identifying time-variant parameters of the beam structure also increases, with the maximum identification error reaching 95.21%. Furthermore, as the noise level increases, both the AUKF and ASRUKF-FF methods exhibit a reduced capability to identify time-variant parameters of the beam structures. However, it is worth noting that the ASRUKF-FF method outperforms the AUKF method in terms of identification effectiveness. As indicated in Table 8, the AUKF method exhibits a maximum identification error of 7.61%, whereas the ASRUKF-FF method achieves a maximum error of 4.14%. This demonstrates that the proposed ASRUKF-FF method exhibits greater robustness in the identification of time-variant parameters.

4.2.3. Discussion on the Identification Effect of the Values of \mathbf{X}_0 , \mathbf{P}_0 , \mathbf{Q} , and \mathbf{R} . Similar to Section 3.2.3, this section focuses on examining the identification performance of time-variant structural parameters using the ASRUKF-FF method under different values of \mathbf{X}_0 , \mathbf{P}_0 , \mathbf{Q} , and \mathbf{R} . The aim is to assess the impact of these algorithm parameters on the accuracy and effectiveness of parameter identification. The comparative analysis adopts the control variable method, and except for the parameters to be studied, all other parameter settings are the same as those in Section 4.2.1. Furthermore, this section primarily considers the parameters to be identified in \mathbf{X}_0 and \mathbf{P}_0 . The specific identification results are depicted in Figures 16–19, while the final identification error is presented in Table 9.

Based on simulation analysis research conducted on the beam model, it has been observed that when solely considering variations in the initial state vector, there exists a specific range requirement for the optimal elastic modulus value within \mathbf{X}_0 . Values outside this range can result in the matrix becoming ill-conditioned, which in turn leads to divergent identification. The appropriate range for this case is about $\mathbf{X}_0 \in [0.09 \times 10^{11}, 1 \times 10^{11}]$, and within this range, the specific value of \mathbf{X}_0 has minimal impact on the identification results. Likewise, there is an upper limit requirement for the initial values to be identified in \mathbf{P}_0 . Values outside this range can also result in the matrix becoming ill-conditioned, which in turn leads to computational divergence. Furthermore, an excessively small value for \mathbf{P}_0 , such as $\mathbf{P}_0 = 1 \times 10^{-8} \mathbf{I}$, can decrease the convergence rate, as illustrated by the red line in Figure 17. This observation aligns with the conclusion stated in Section 3.2.3. Simultaneously, excessive values for \mathbf{P}_0 can result in significant jitter during the initial stages of identification (as depicted by the yellow line in Figure 17), leading to algorithmic instability. However, within a certain range, the value of \mathbf{P}_0 has minimal influence on the accuracy of stiffness parameter identification. When solely

considering variations in the modeling error covariance \mathbf{Q} , both excessively large and excessively small \mathbf{Q} values (such as $1 \times 10^{-7} \mathbf{I}$ or $1 \times 10^{-10} \mathbf{I}$) would result in an increase in identification error. This observation aligns with the conclusion stated in Section 3.2.3. The reasoning behind this observation can also be found in Section 3.2.3. When solely considering variations in the measurement error covariance \mathbf{R} , an increase in \mathbf{R} would correspondingly lead to a further increase in the identification error of stiffness parameters. This observation aligns with the conclusion stated in Section 3.2.3. However, in this case, when the \mathbf{R} value is excessively small, it can cause the matrix to become ill-conditioned, leading to divergent identification. Based on the above analysis, it can be concluded that within a certain range, the values of \mathbf{X}_0 and \mathbf{P}_0 have minimal impact on the identification performance of the ASRUKF-FF algorithm. The initial values of \mathbf{Q} and \mathbf{R} have a substantial impact on the identification results, with particular sensitivity observed in the \mathbf{R} value, which significantly affects the accuracy of stiffness parameter identification for the beam structure.

4.2.4. Discussion on the Identification Effect of Different Measurements. Analogous to Section 3.2.4, this section primarily focuses on the examination of the influence of different combinations of measurements on the identification outcomes. The comparative analysis employs the control variable method, where all parameter settings remain the same as those in Section 4.2.1, except for the variations in measurements. Furthermore, the calculation process for each working condition can be referenced from Section 3.2.4. The specific identification results are illustrated in Figures 20–22, while the comparison of final identification errors is provided in Table 10. The meanings of the characters in Figures 20–22 and Table 10 are explained as follows: taking “DIS-3-5-7-9-11” as an example, “DIS-3-5-7-9-11” indicates that all displacement measurements are utilized, with a total of 5 measurement values included. The measurement values used are the vertical displacements of the simply supported bridge, as depicted in Figure 13, with degrees of freedom of 3, 5, 7, 9, and 11. Furthermore, for the purpose of facilitating comparative observation, a structural diagram of the simply supported bridge is depicted in Figure 13 is provided in Figure 23. It is worth noting that during the simulation analysis process, it has been observed that the time history curve of the sensitive parameter based on the “DIS-7-9” working condition does not exhibit a distinct pulse response characteristic. In addition, the working condition based on “DIS-2-4-8” fails to converge. Therefore, the subsequent discussion and analysis will exclude these two working conditions.

Based on the findings from Figures 20–22 and Table 10, it can be observed that, for the simply supported bridge structure depicted in Figure 13, a minimum of 3 measurements is sufficient to accurately identify the middle four stiffness parameters simultaneously. However, it should be noted that not every combination of three measurements can successfully accomplish the identification task in this particular case. Through data analysis, no evident pattern of measurement combinations has been identified. However, among the combinations of working conditions with three

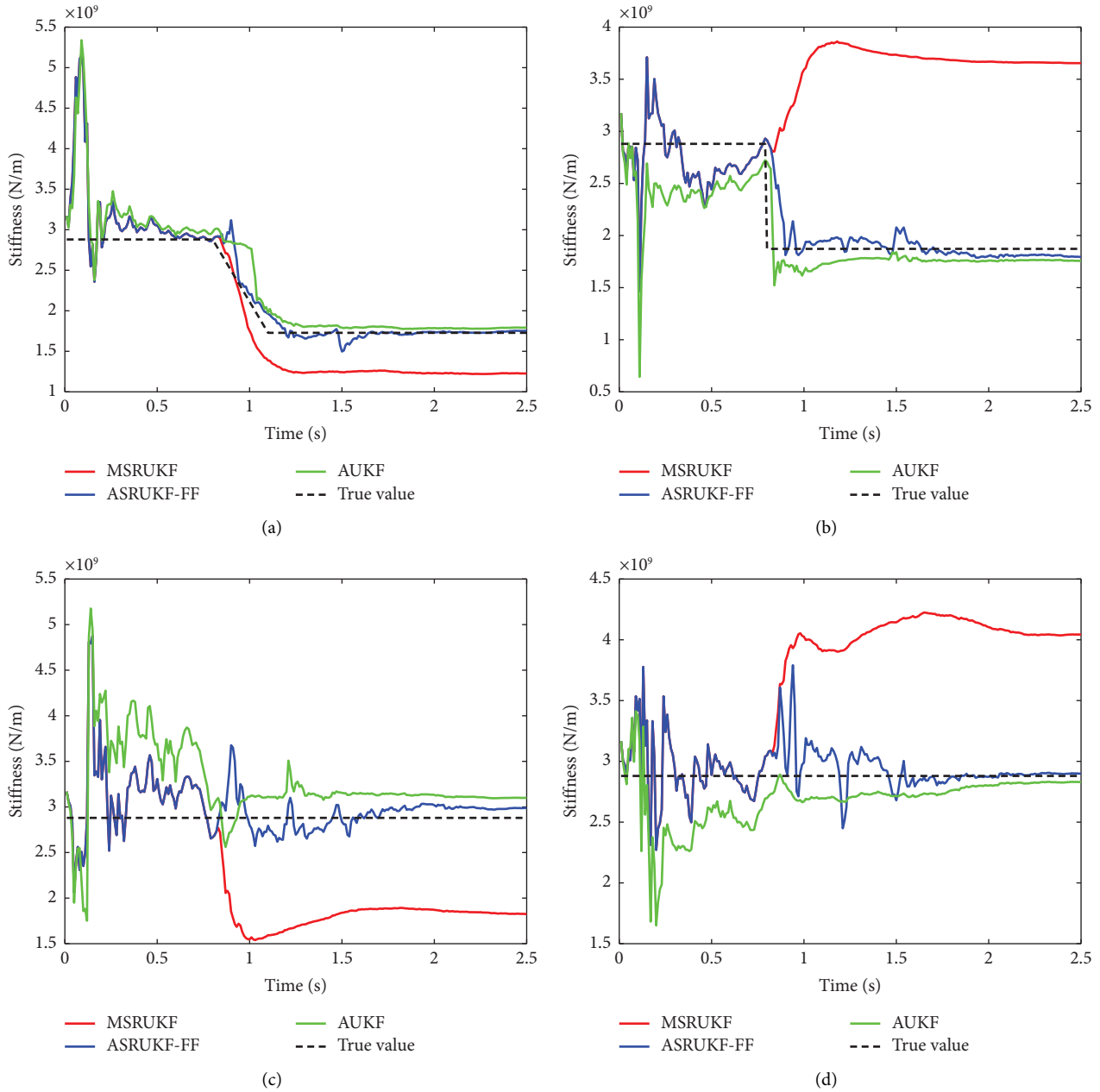


FIGURE 15: Identification effect of different algorithms (5% noise level): (a) the stiffness of beam ②, (b) the stiffness of beam ③, (c) the stiffness of beam ④, and (d) the stiffness of beam ⑤.

TABLE 8: Estimation errors of the final identification results with 5% noise.

Algorithms	Stiffness identification error			
	Beam ② (%)	Beam ③ (%)	Beam ④ (%)	Beam ⑤ (%)
MSRUKF	-29.08	95.21	-36.63	40.38
ASRUKF-FF	1.36	-4.14	3.74	0.65
AUKF	3.66	-6.20	7.61	-1.75

Note. Stiffness identification error = (identification value - true value) / true value × 100%.

measurements, those that include degrees of freedom 7 and 9, and where the third degree of freedom is located in the left half of the bridge (such as DIS-3-7-9 and DIS-5-7-9), higher

identification accuracy is exhibited. In addition, it is worth noting that in this case study, there is no positive correlation between the number of measurements and identification

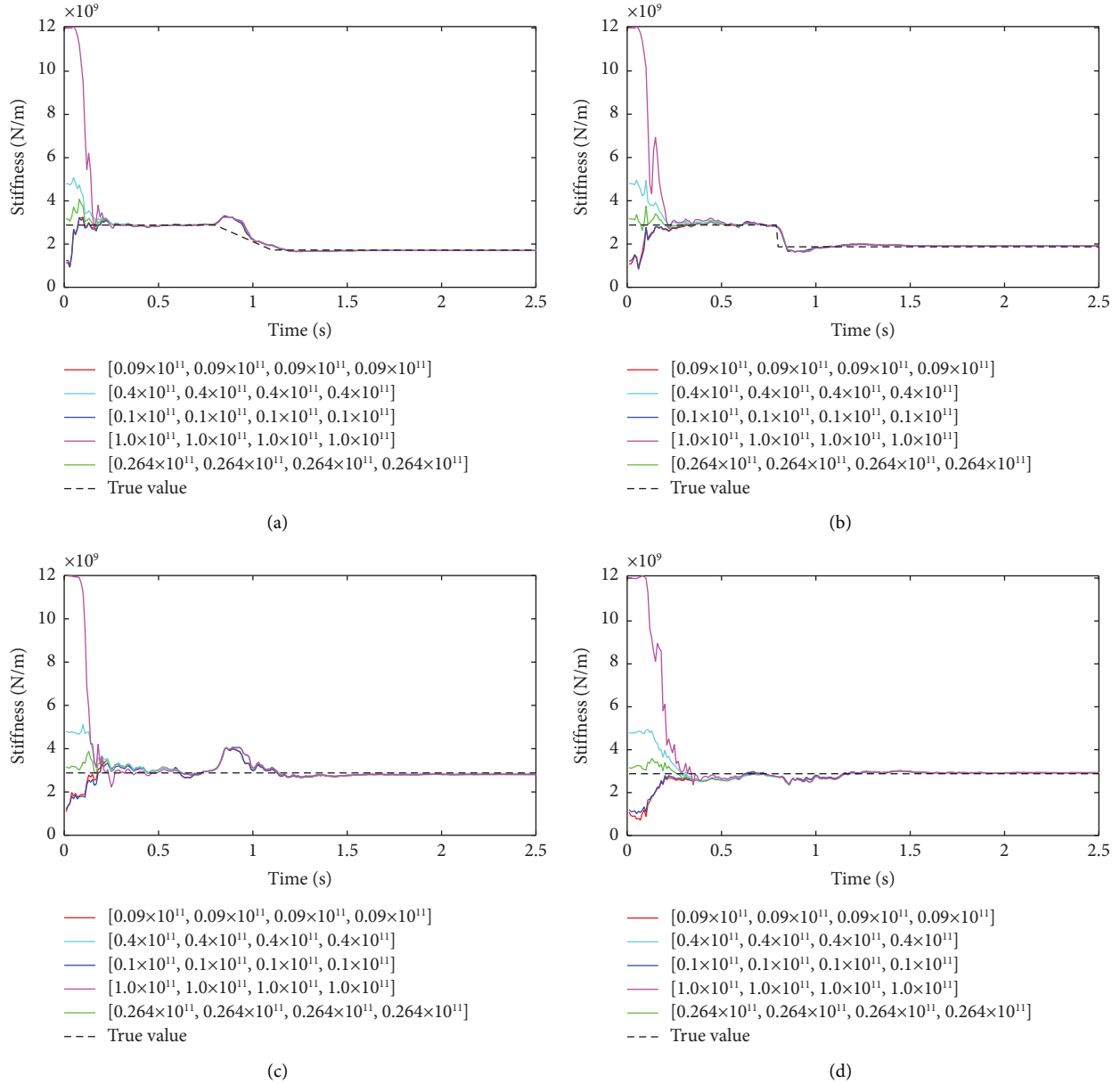


FIGURE 16: Identification results of different \mathbf{X}_0 values (the legend values correspond to the initial elastic modulus parameters; for example, the legend “[0.9×10^{11} , 0.9×10^{11} , 0.9×10^{11} , 0.9×10^{11}]” in red indicates that the initial values of E_2 , E_3 , E_4 , and E_5 in the state vector are all 0.09 , with 10^{11} representing a scale factor in practical computations): (a) the stiffness of beam ②, (b) the stiffness of beam ③, (c) the stiffness of beam ④, and (d) the stiffness of beam ⑤.

accuracy. Having a large number of measurement values does not necessarily guarantee high identification accuracy. For instance, in this case, the identification performance of the “DIS-3-5-9-11” and “DIS-3-7-9-11” working conditions is superior to that of the original five measured values. The combination of measurements is an optimization problem, which is related to the type of structure, environmental noise, response sensitivity, and modal shape. In this case, due to the relatively small number of measurement value combinations, a comprehensive study is conducted to examine the identification effect of each combination. In the future, further research is needed to explore the

determination method of the optimal measurement value combination scheme, incorporating optimization algorithms for enhanced accuracy.

4.2.5. Discussion on the Identification Effect of Modeling Error. This section takes into account the influence of modeling errors on the estimation effect. Based on the model analysis conducted in Section 4.1, the parameters of elastic modulus (E_1 and E_6), unit length mass (ρA), section moment of inertia (I), and modal damping ratio (τ) are chosen as the focus of investigation. Referring to Sections 4.1 and 4.2.1 for the remaining parameter settings, it is worth noting that the

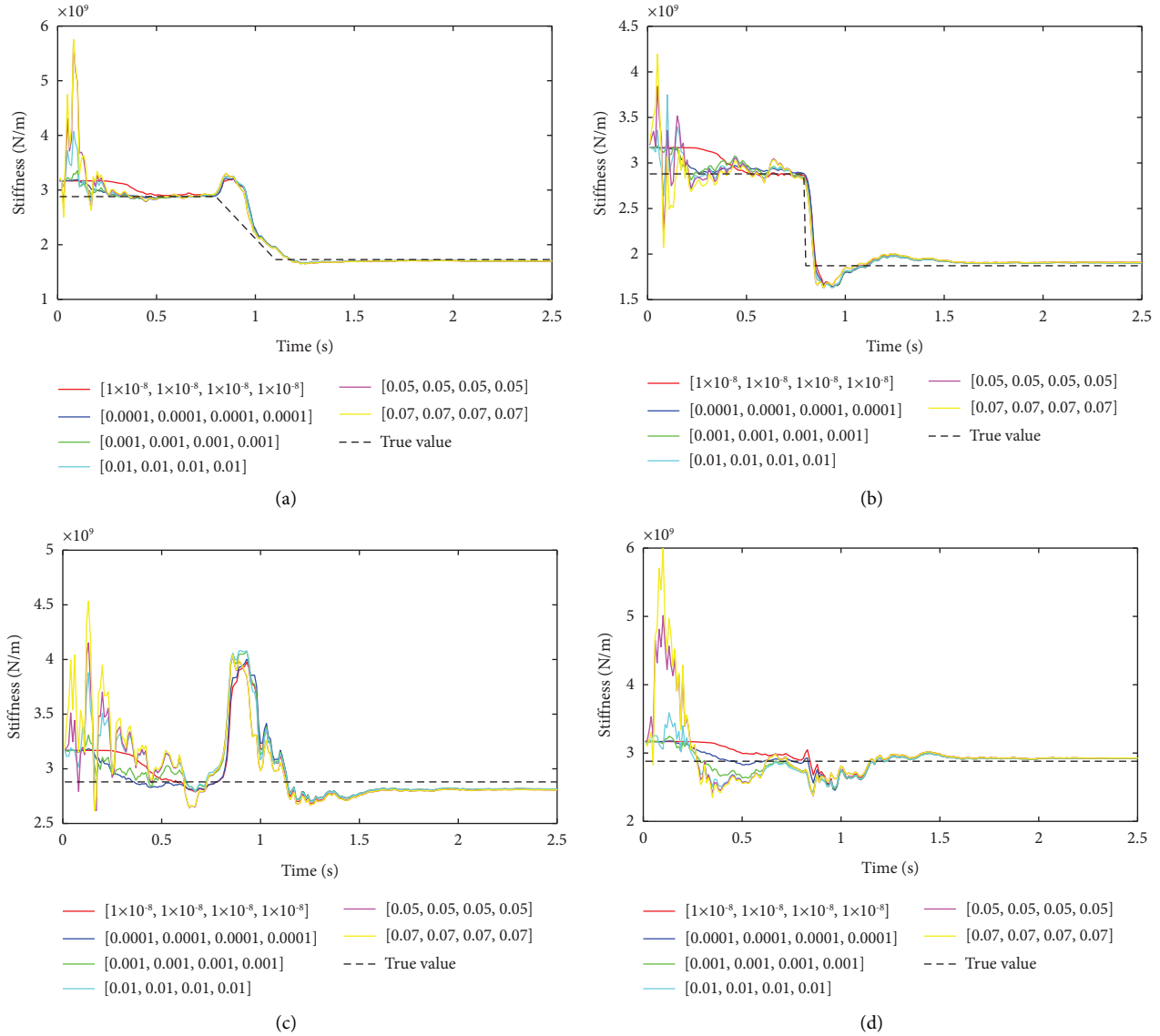


FIGURE 17: Identification results of different \mathbf{P}_0 values (the legend values correspond to the initial covariance values of elastic modulus parameters; for example, the legend “[1×10^{-8} , 1×10^{-8} , 1×10^{-8} , 1×10^{-8}]” in red indicates that $\mathbf{P}_{0_E2} = 1 \times 10^{-8}$, $\mathbf{P}_{0_E3} = 1 \times 10^{-8}$, $\mathbf{P}_{0_E4} = 1 \times 10^{-8}$, $\mathbf{P}_{0_E5} = 1 \times 10^{-8}$): (a) the stiffness of beam ②, (b) the stiffness of beam ③, (c) the stiffness of beam ④, and (d) the stiffness of beam ⑤.

measurement noise is set at 2%. In addition, different modeling errors can result in variations in sensitivity parameter thresholds. Therefore, the specific implementation process is referenced from Section 3.2.4. The specific identification results can be observed in Figures 24–27, while the final identification error is presented in Table 11.

Based on the simulation analysis, it has been determined that the section moment of inertia (I) is the modeling parameter with the most significant impact on the identification results for the beam model. Furthermore, it has been observed that the maximum identification error of the stiffness parameters can reach 9.05% when a negative 5% modeling error is present. Meanwhile, the modal damping ratio τ is identified as the modeling parameter that has the least impact on the identification effect.

Moreover, the maximum identification errors of stiffness parameters are 2.16% and 2.50% under $a \pm 30\%$ modeling error. When considering only the modeling error of the elastic modulus, it has been observed that the maximum identification error of the stiffness parameters gradually increases with higher modeling errors. Notably, negative modeling errors have a greater impact on the identification effect. Furthermore, it is important to note that the modeling errors of the mass and modal damping ratio parameters do not exhibit a positive correlation with the identification errors of the stiffness parameters. Interestingly, there is a peculiar phenomenon, where a large modeling error is present, yet the identification accuracy remains high. It is speculated that the modeling parameters may compensate for the uncertainties introduced by

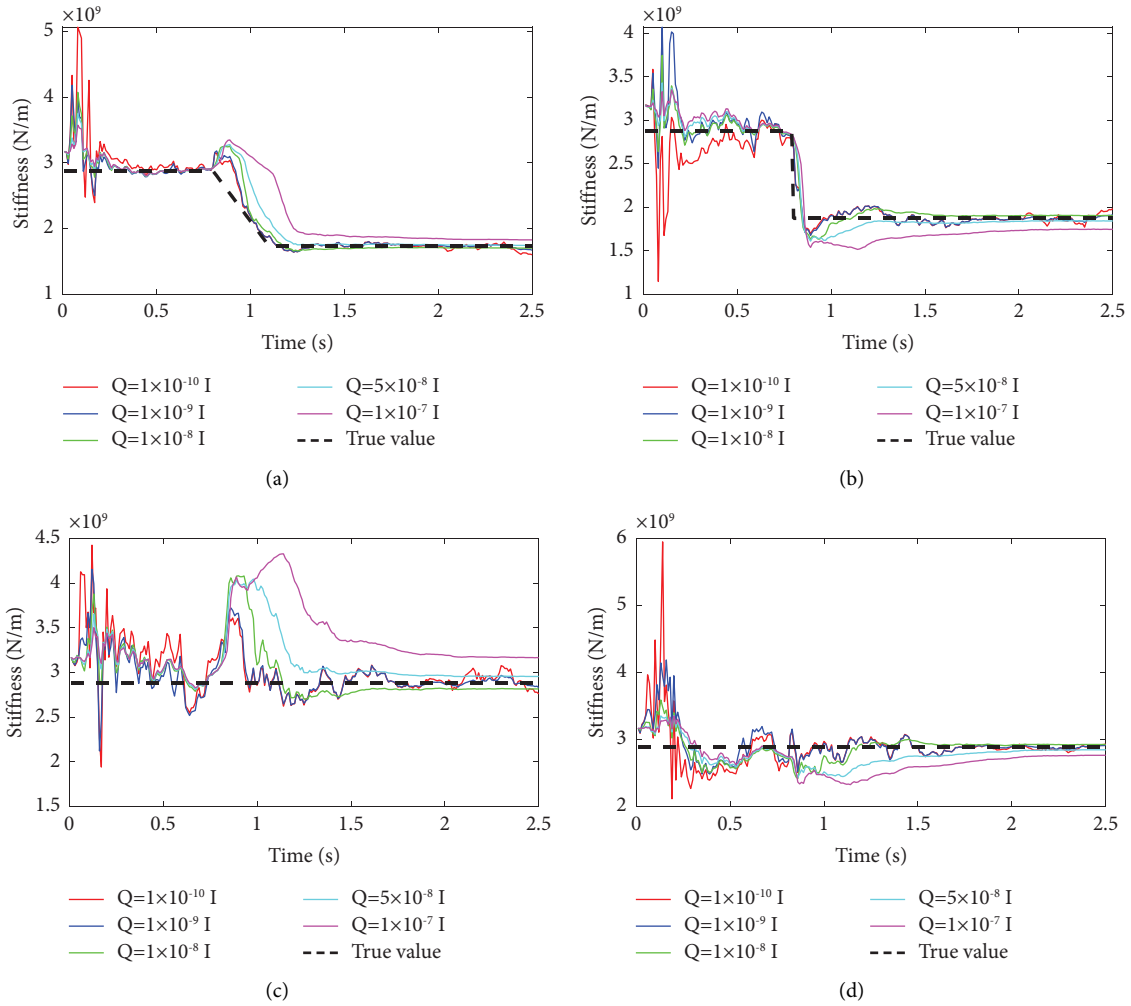


FIGURE 18: Identification results of different Q values: (a) the stiffness of beam ②, (b) the stiffness of beam ③, (c) the stiffness of beam ④, and (d) the stiffness of beam ⑤.

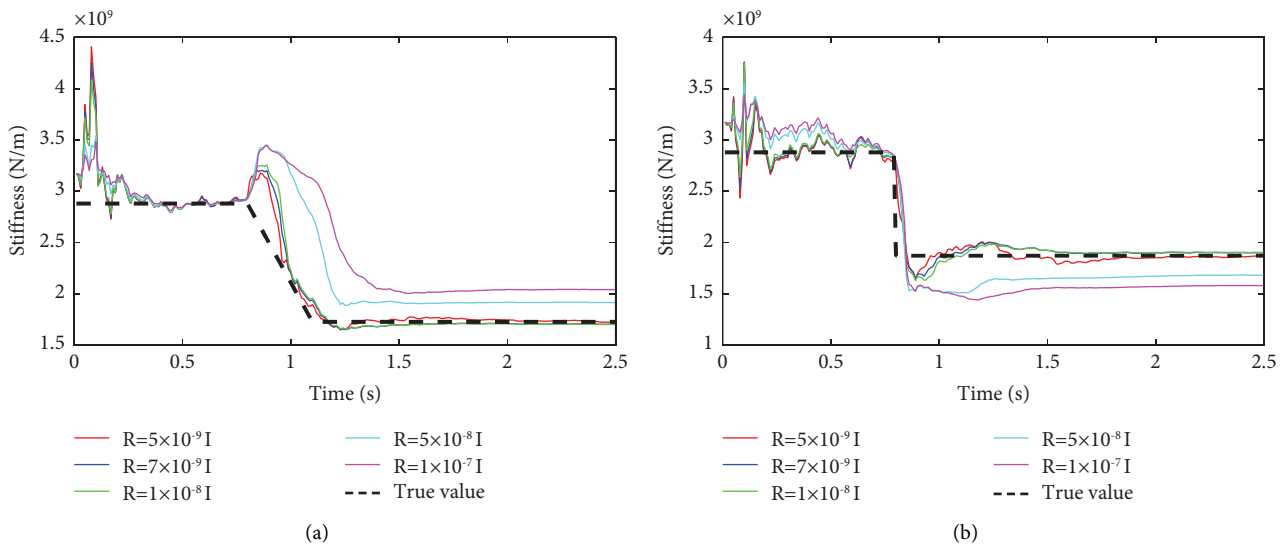


FIGURE 19: Continued.

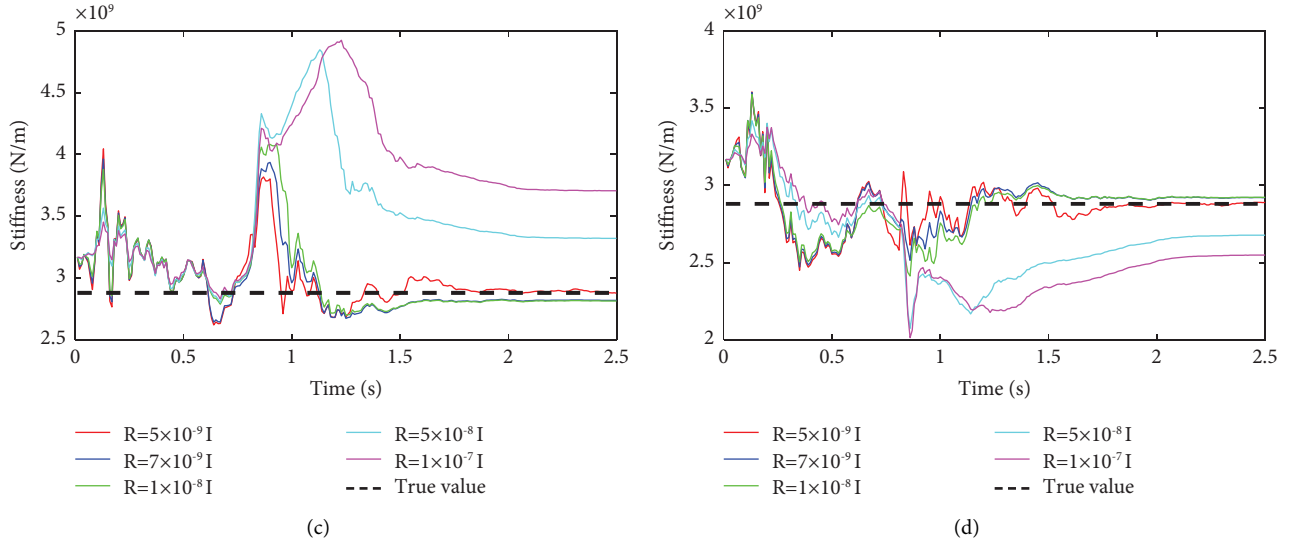


FIGURE 19: Identification results of different \mathbf{R} values: (a) the stiffness of beam ②, (b) the stiffness of beam ③, (c) the stiffness of beam ④, and (d) the stiffness of beam ⑤.

TABLE 9: Estimation errors of the final identification results with different parameter settings.

Variant parameter	Parameter values	Stiffness identification error			
		Beam ② (%)	Beam ③ (%)	Beam ④ (%)	Beam ⑤ (%)
\mathbf{X}_0	$[0.09 \times 10^{11}, 0.09 \times 10^{11}, 0.09 \times 10^{11}, 0.09 \times 10^{11}]$	-1.65	1.90	-2.53	1.61
	$[0.1 \times 10^{11}, 0.1 \times 10^{11}, 0.1 \times 10^{11}, 0.1 \times 10^{11}]$	-1.65	1.90	-2.53	1.61
	$[0.264 \times 10^{11}, 0.264 \times 10^{11}, 0.264 \times 10^{11}, 0.264 \times 10^{11}]$	-1.53	1.73	-2.31	1.47
	$[0.4 \times 10^{11}, 0.4 \times 10^{11}, 0.4 \times 10^{11}, 0.4 \times 10^{11}]$	-1.53	1.73	-2.31	1.47
	$[1.0 \times 10^{11}, 1.0 \times 10^{11}, 1.0 \times 10^{11}, 1.0 \times 10^{11}]$	-1.53	1.73	-2.30	1.47
\mathbf{P}_0	$[1 \times 10^{-8}, 1 \times 10^{-8}, 1 \times 10^{-8}, 1 \times 10^{-8}]$	-1.65	1.89	-2.52	1.62
	$[0.0001, 0.0001, 0.0001, 0.0001]$	-1.52	1.70	-2.27	1.45
	$[0.001, 0.001, 0.001, 0.001]$	-1.52	1.71	-2.28	1.46
	$[0.01, 0.01, 0.01, 0.01]$	-1.53	1.73	-2.31	1.47
	$[0.05, 0.05, 0.05, 0.05]$	-1.66	1.91	-2.54	1.62
	$[0.07, 0.07, 0.07, 0.07]$	-1.66	1.91	-2.54	1.62
\mathbf{Q}	$1 \times 10^{-10} \mathbf{I}$	-7.35	5.96	-4.19	1.68
	$1 \times 10^{-9} \mathbf{I}$	-3.31	2.34	-1.75	1.09
	$1 \times 10^{-8} \mathbf{I}$	-1.53	1.73	-2.31	1.47
	$5 \times 10^{-8} \mathbf{I}$	0.83	-1.57	2.55	-1.26
	$1 \times 10^{-7} \mathbf{I}$	5.74	-6.69	9.87	-4.09
\mathbf{R}	$5 \times 10^{-9} \mathbf{I}$	-0.34	-0.17	-0.07	0.35
	$7 \times 10^{-9} \mathbf{I}$	-1.43	1.54	-2.13	1.41
	$1 \times 10^{-8} \mathbf{I}$	-1.53	1.73	-2.31	1.47
	$5 \times 10^{-8} \mathbf{I}$	10.83	-10.10	15.30	-7.05
	$1 \times 10^{-7} \mathbf{I}$	18.11	-15.55	28.66	-11.53

certain random noise components. In summary, even with 2% measurement noise, the proposed adaptive algorithm exhibits a certain ability to mitigate modeling errors for

beam structures. However, it is crucial to emphasize the strict control of the parameter value for the section moment of inertia.

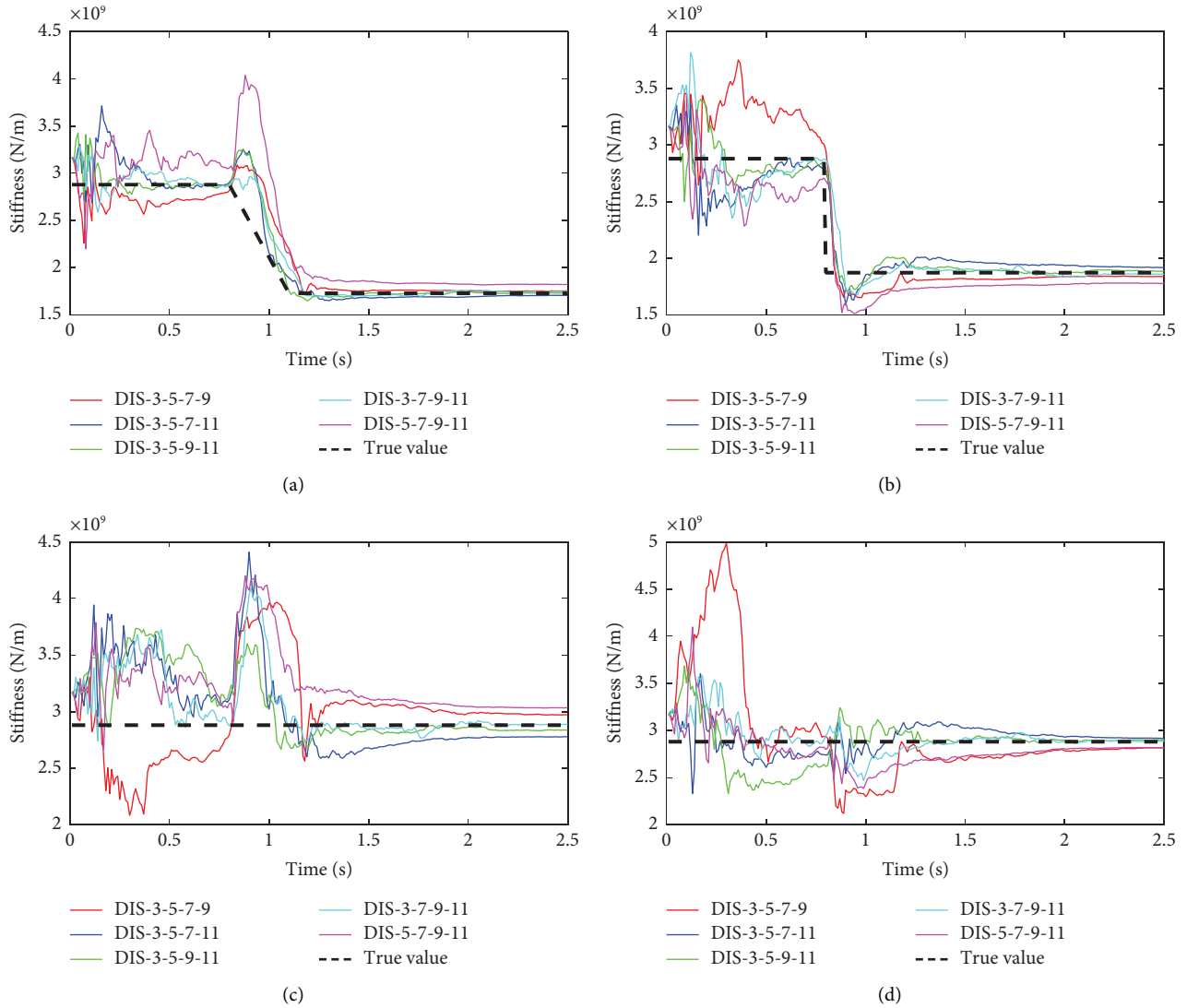


FIGURE 20: Identification results with 4 measurement values by ASRUKF-FF: (a) the stiffness of beam ②, (b) the stiffness of beam ③, (c) the stiffness of beam ④, and (d) the stiffness of beam ⑤.

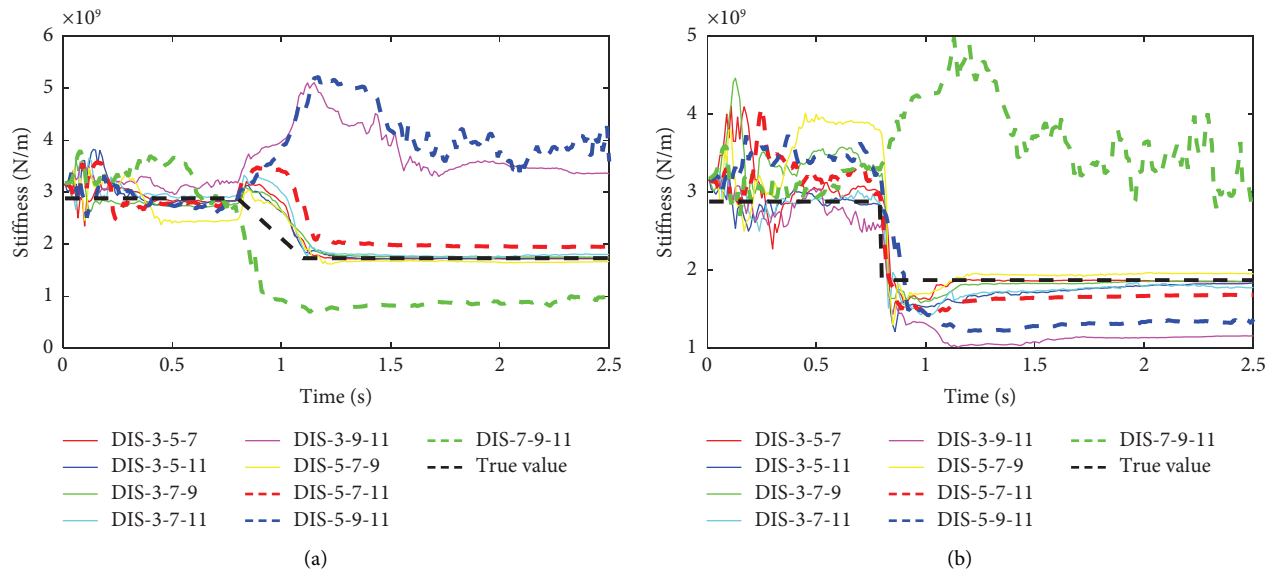


FIGURE 21: Continued.

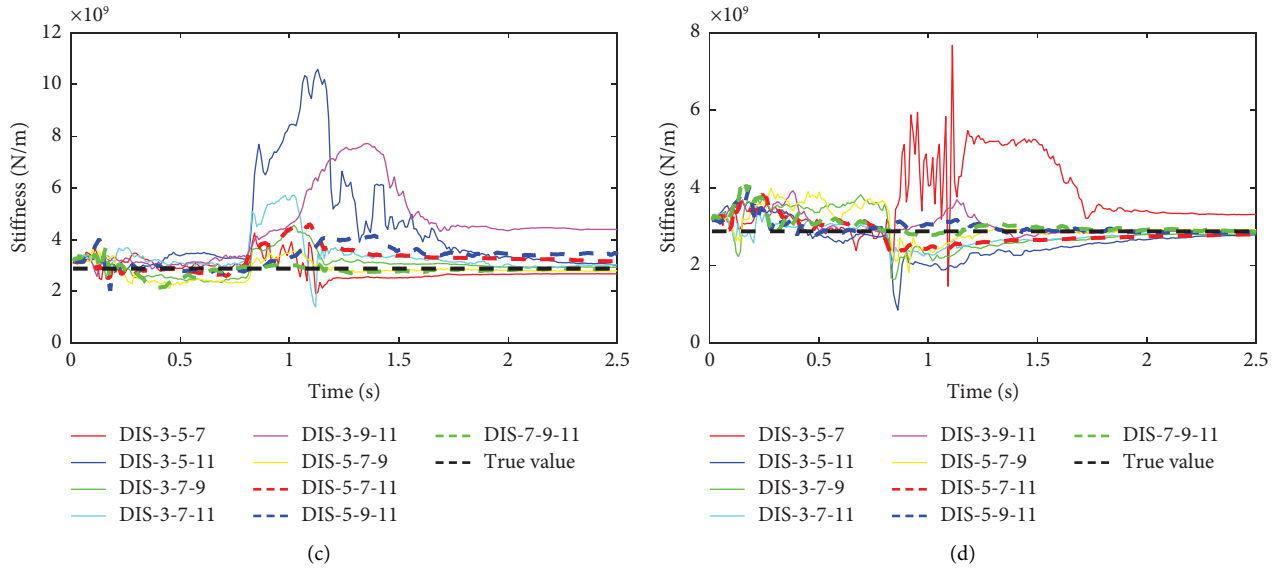


FIGURE 21: Identification results with 3 measurement values by ASRUKF-FF: (a) the stiffness of beam ②, (b) the stiffness of beam ③, (c) the stiffness of beam ④, and (d) the stiffness of beam ⑤.

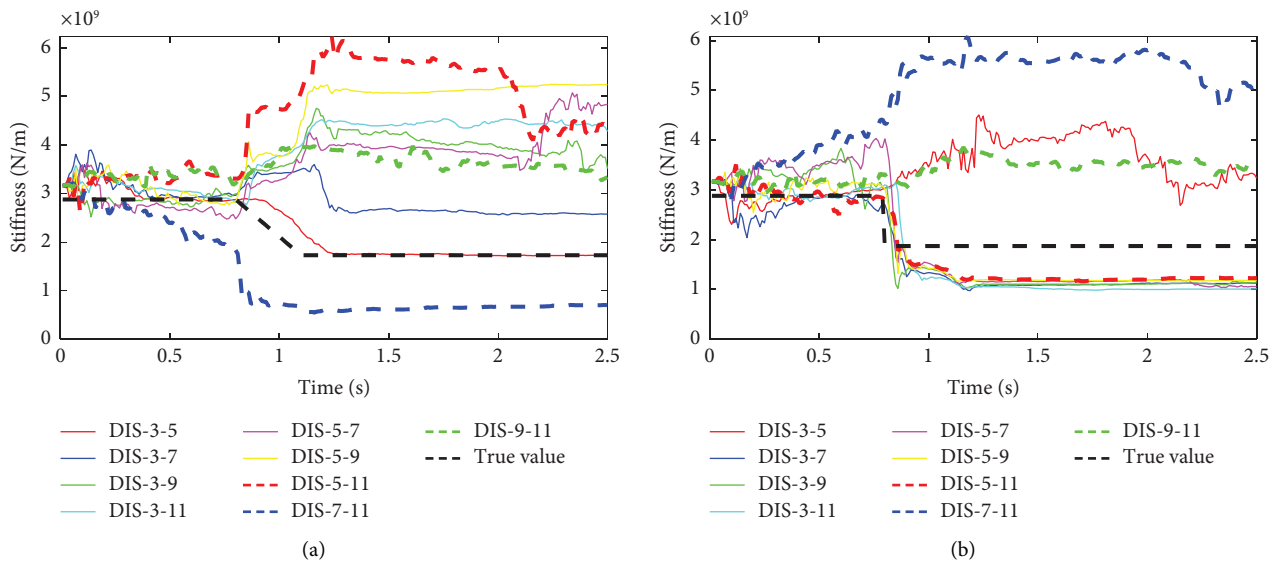


FIGURE 22: Continued.

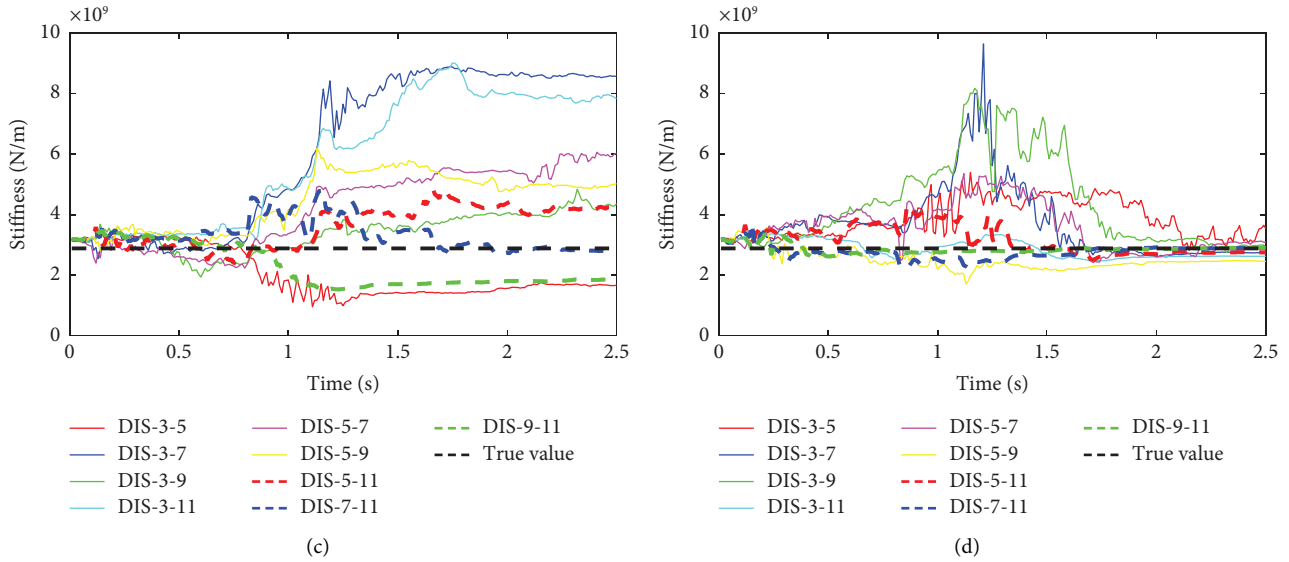


FIGURE 22: Identification results with 2 measurement values by ASRUKF-FF: (a) the stiffness of beam ②, (b) the stiffness of beam ③, (c) the stiffness of beam ④, and (d) the stiffness of beam ⑤.

TABLE 10: Estimation errors in the final identification results using various measurements for the simply-supported bridge.

Working condition	Type of measurements	Stiffness identification error			
		Beam ② (%)	Beam ③ (%)	Beam ④ (%)	Beam ⑤ (%)
1	DIS-3-5-7-9-11	-1.53	1.73	-2.31	1.47
2	DIS-3-5-7-9	1.46	-1.80	3.20	-2.26
3	DIS-3-5-7-11	-1.32	2.43	-3.57	1.30
4	DIS-3-5-9-11	0.15	0.78	-1.52	0.69
5	DIS-3-7-9-11	1.18	-0.70	0.28	0.23
6	DIS-5-7-9-11	5.46	-5.08	5.32	-2.17
7	DIS-3-5-7	-0.55	-1.03	-6.89	15.06
8	DIS-3-5-11	0.16	-2.15	5.03	-3.31
9	DIS-3-7-9	1.33	-0.88	1.93	-2.56
10	DIS-3-7-11	4.16	-4.95	4.83	-0.12
11	DIS-3-9-11	94.20	-38.14	52.40	0.11
12	DIS-5-7-9	-3.68	4.40	-3.08	1.48
13	DIS-5-7-11	12.99	-10.14	10.08	-2.82
14	DIS-5-9-11	107.64	-26.68	18.82	-1.28
15	DIS-7-9-11	-41.95	55.43	0.24	-0.43
16	DIS-3-5	0.18	72.66	-42.20	22.93
17	DIS-3-7	49.14	-39.88	197.28	-4.88
18	DIS-3-9	103.28	-38.60	51.15	1.07
19	DIS-3-11	147.82	-45.81	171.77	-9.09
20	DIS-5-7	180.02	-43.58	109.19	6.80
21	DIS-5-9	203.52	-37.06	74.38	-14.93
22	DIS-5-11	154.05	-34.50	46.98	-4.63
23	DIS-7-11	-59.43	180.20	-3.16	0.75
24	DIS-9-11	93.08	84.58	-35.90	0.60

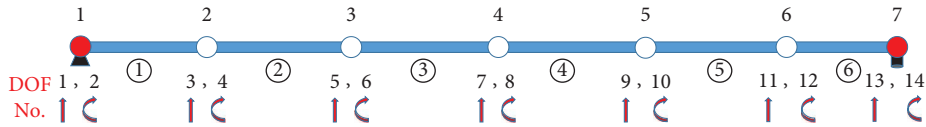


FIGURE 23: Simplified diagram of the simply supported bridge of Figure 13.

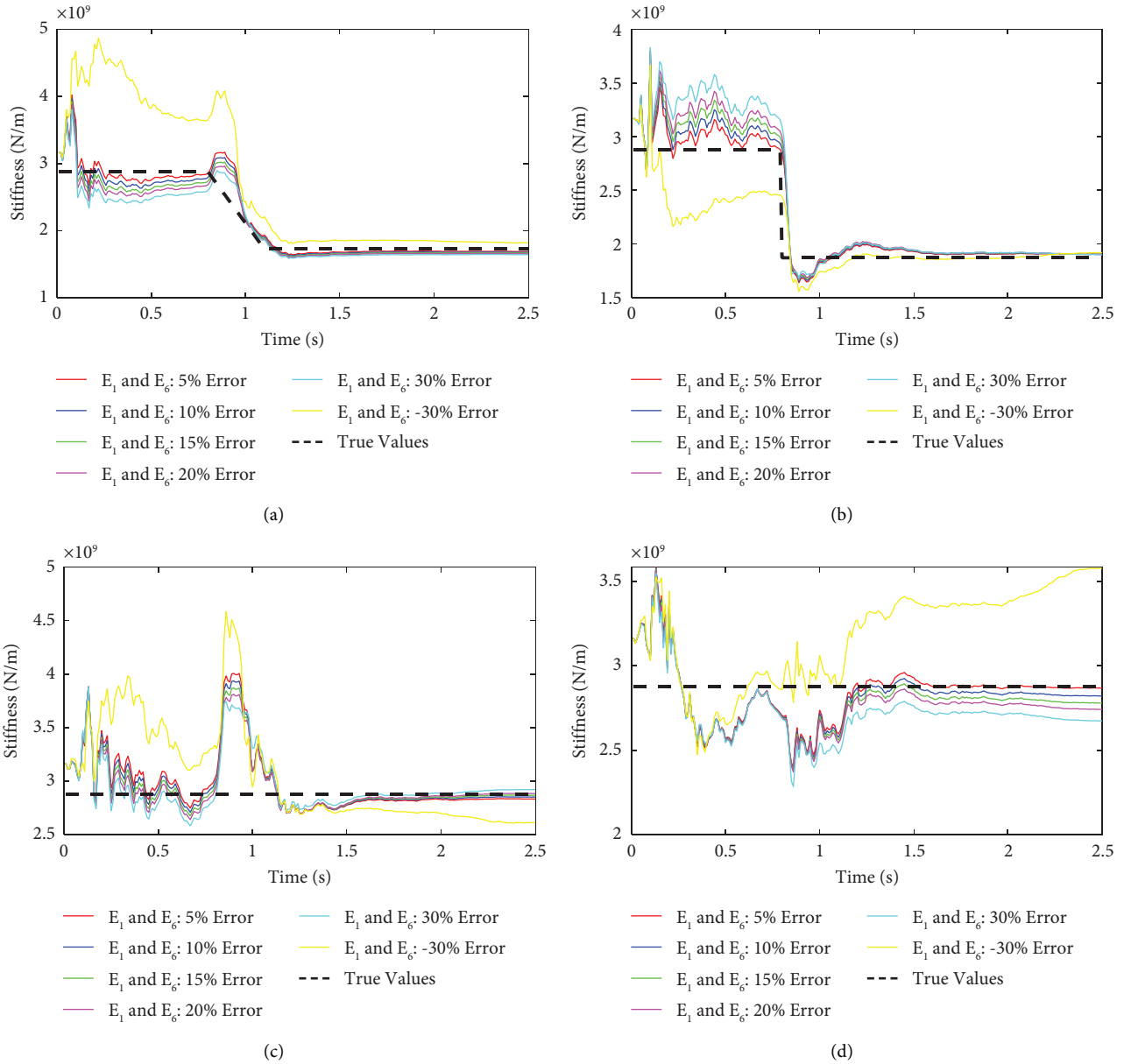
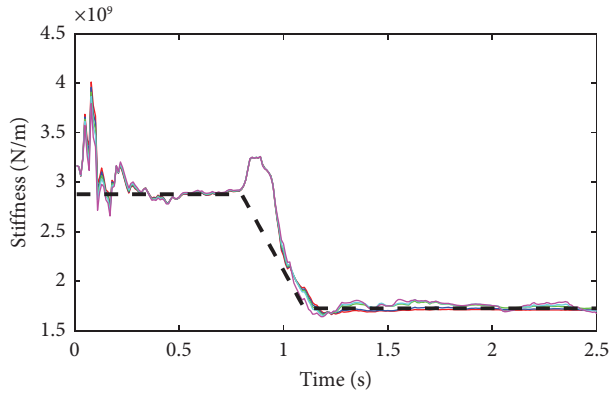
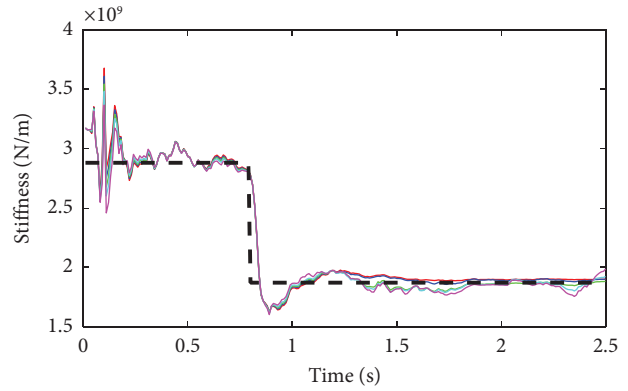


FIGURE 24: Identification results based on different elastic modulus modeling errors: (a) the stiffness of beam ②, (b) the stiffness of beam ③, (c) the stiffness of beam ④, and (d) the stiffness of beam ⑤.



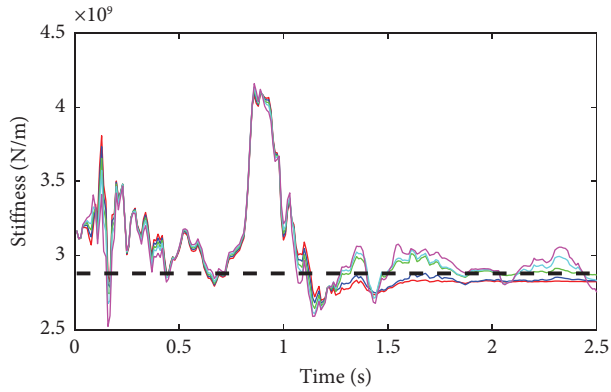
— Unit length mass: 5% Error
 — Unit length mass: 10% Error
 — Unit length mass: 15% Error
 — Unit length mass: 20% Error
 — Unit length mass: 30% Error
 - - - True Values

(a)



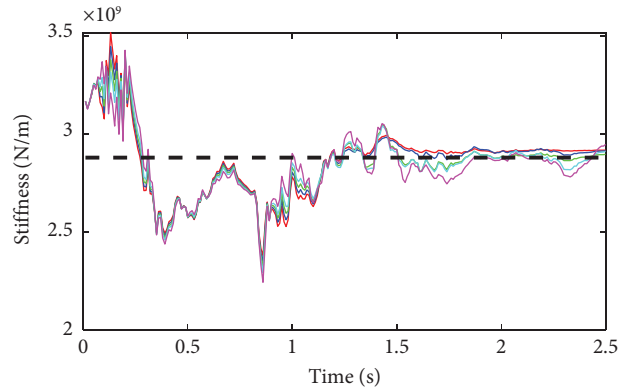
— Unit length mass: 5% Error
 — Unit length mass: 10% Error
 — Unit length mass: 15% Error
 — Unit length mass: 20% Error
 — Unit length mass: 30% Error
 - - - True Values

(b)



— Unit length mass: 5% Error
 — Unit length mass: 10% Error
 — Unit length mass: 15% Error
 — Unit length mass: 20% Error
 — Unit length mass: 30% Error
 - - - True Values

(c)



— Unit length mass: 5% Error
 — Unit length mass: 10% Error
 — Unit length mass: 15% Error
 — Unit length mass: 20% Error
 — Unit length mass: 30% Error
 - - - True Values

(d)

FIGURE 25: Identification results based on different unit length mass modeling errors: (a) the stiffness of beam ②, (b) the stiffness of beam ③, (c) the stiffness of beam ④, and (d) the stiffness of beam ⑤.

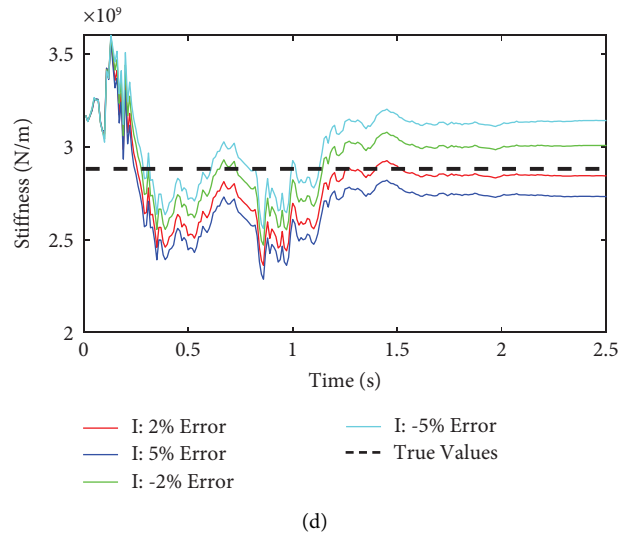
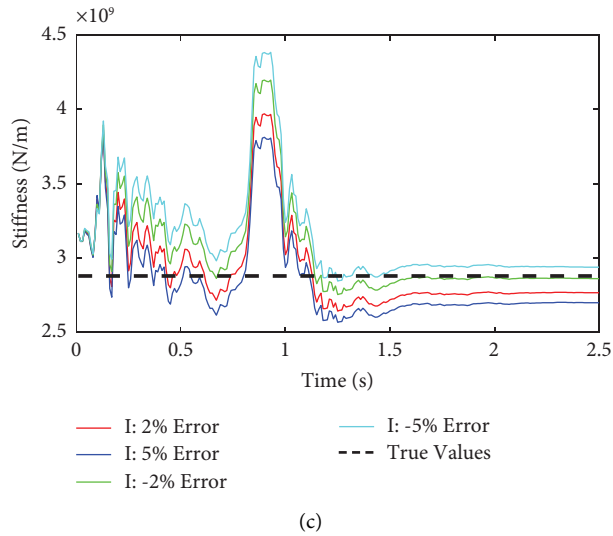
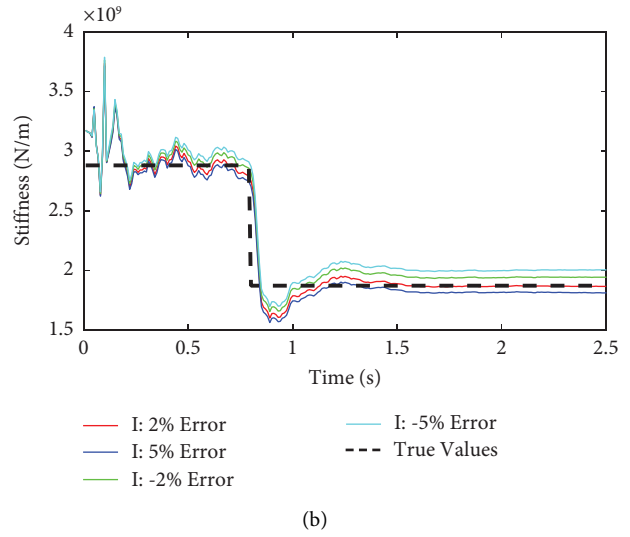
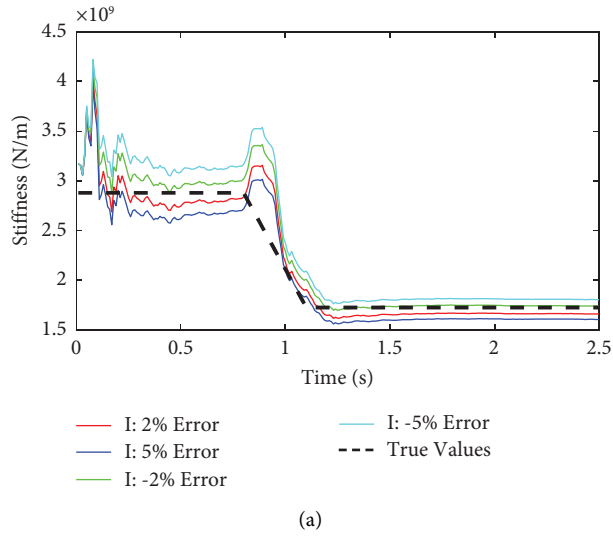


FIGURE 26: Identification results based on different modeling errors of section moment of inertia: (a) the stiffness of beam ②, (b) the stiffness of beam ③, (c) the stiffness of beam ④, and (d) the stiffness of beam ⑤.

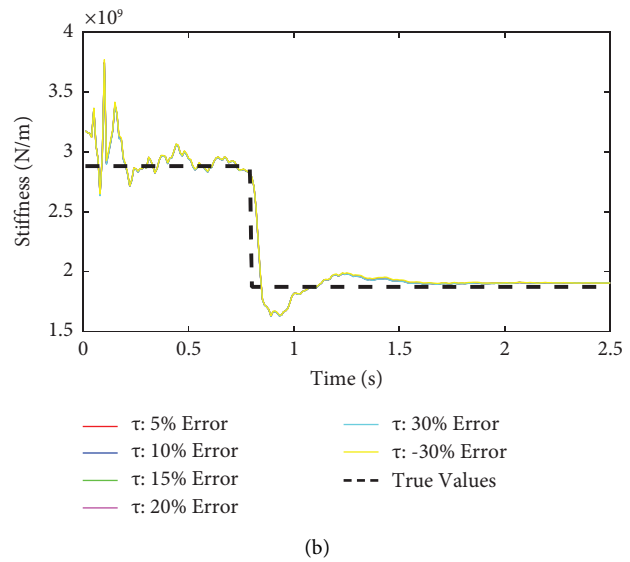
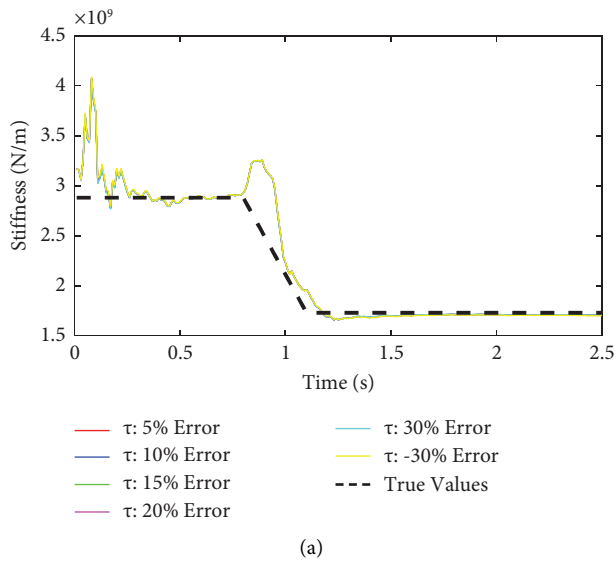


FIGURE 27: Continued.

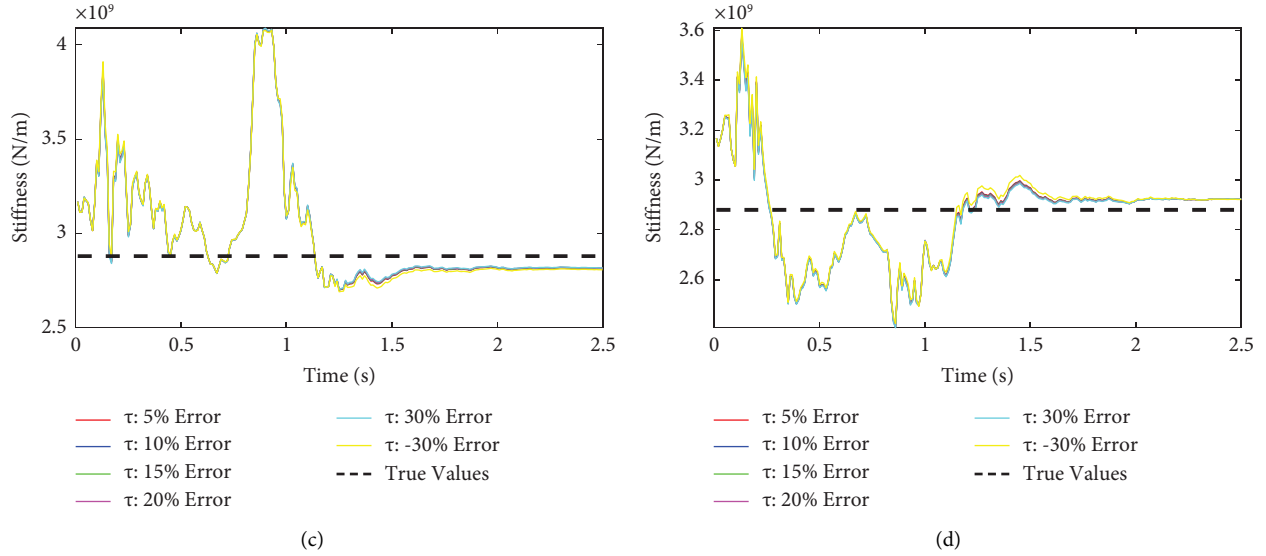


FIGURE 27: Identification results based on different modeling errors of modal damping ratio: (a) the stiffness of beam ②, (b) the stiffness of beam ③, (c) the stiffness of beam ④, and (d) the stiffness of beam ⑤.

TABLE 11: Final identification errors with different modeling errors.

Uncertain parameter	Modeling error (%)	Stiffness identification error			
		Beam ② (%)	Beam ③ (%)	Beam ④ (%)	Beam ⑤ (%)
Elastic modulus: E_1 and E_6	5	-2.32	1.74	-1.65	-0.37
	10	-3.01	1.74	-1.02	-2.01
	15	-3.63	1.72	-0.44	-3.47
	20	-4.18	1.70	0.12	-4.78
	30	-5.08	1.53	1.37	-7.16
	-30	5.30	2.64	-9.31	24.24
Mass per length: ρA	5	-1.13	1.51	-1.93	1.31
	10	-0.98	1.60	-1.76	1.20
	15	0.01	0.61	-0.39	0.59
	20	-1.65	2.72	-1.73	1.12
	30	-3.11	6.18	-4.40	2.35
Section moment of inertia: I	2	-3.78	-0.28	-3.93	-1.28
	-2	0.82	3.82	-0.62	4.38
	5	-6.95	-3.16	-6.27	-5.15
	-5	4.58	7.10	2.04	9.05
Modal damping ratio: τ	5	-1.50	1.74	-2.28	1.48
	10	-1.47	1.75	-2.25	1.49
	15	-1.43	1.76	-2.22	1.49
	20	-1.40	1.78	-2.20	1.50
	30	-1.34	1.81	-2.16	1.52
	-30	-1.75	1.68	-2.50	1.46

Note. (1) Cell data with background color represents the maximum error in each row. (2) A positive modeling error represents an increase in the parameter, while a negative modeling error represents a decrease in the parameter. If the true parameter value is 10, considering a modeling error of $\pm 5\%$, the parameter value becomes $10 \times (1 \pm 5\%)$.

5. Conclusion

In this paper, the standard SRUKF method is modified by incorporating QR decomposition technology. This modification aims to eliminate the requirements for a positive-definite covariance matrix in the unscented transform process and ensure the numerical stability of the algorithm unconditionally. Building upon this modification, the ASRUKF-FF method is proposed in this study by incorporating an adaptive forgetting factor. This enhancement aims to improve the algorithm's capability to identify time-variant parameters. The main conclusions are summarized as follows:

- (1) The proposed ASRUKF-FF method utilizes a sensitive parameter threshold to intelligently determine whether to invoke the adaptive algorithm. Numerical simulation verification, as depicted in Figure 4 and Table 2, demonstrates that the method of determining the threshold based on the time history curve of sensitive parameters calculated by MSRUKF is reliable and accurate. Further simulation results indicate that the proposed ASRUKF-FF method exhibits insensitivity to the threshold within a certain range. This characteristic ensures the stability of the algorithm.
- (2) In contrast to adaptive methods, where the covariance correction coefficient is typically an empirical constant or determined through experience, the forgetting factor correction coefficient used in this paper is calculated based on the residual information obtained at each recursive step. This approach allows for automatic adjustment of the coefficient based on the system's uncertainty. In addition, the forgetting factor can be mathematically derived, providing high reliability.
- (3) The proposed ASRUKF-FF method offers a broader range of applications and can be effectively utilized in research on inverse problems in the field of building and bridge structures. Moreover, the method is characterized by its simplicity in implementation, ease of programming, and robustness.
- (4) For shear models, variations in \mathbf{X}_0 , \mathbf{P}_0 , \mathbf{Q} , and \mathbf{R} values have a minimal impact on the identification of stiffness parameters. However, they do have a significant effect on the identification of damping parameters, with \mathbf{R} having the most pronounced impact. In the case of stiffness parameter identification for beam models, the values of \mathbf{X}_0 and \mathbf{P}_0 have a minor influence on the identification performance. However, the initial values of \mathbf{Q} and \mathbf{R} play a crucial role in determining the identification results, particularly with regard to the sensitivity of the \mathbf{R} value in achieving accurate identification of the stiffness parameters of the beam structure. In addition, for the beam model, it is important to consider the parameter range requirements for \mathbf{X}_0 , \mathbf{P}_0 , and \mathbf{R} . Exceeding the specified value range can lead to ill-

conditioned matrices and ultimately result in identification failure.

- (5) The proposed algorithm demonstrates high identification accuracy even when dealing with incomplete measurement values. In the case of the shear model examined in this paper, as the number of measured values increases, the identification accuracy is further improved. In the case of the more complex beam model, the number of measurements is not positively correlated with identification accuracy. The determination method of the optimal measurement value combination scheme still requires further research, particularly in combination with optimization algorithms.
- (6) In the case of the shear model, when there is a 10% modeling error in the mass parameter, the maximum identification errors of the structural stiffness and damping parameters are 10.07% and 11.71%, respectively. In the case of the beam model, the section moment of inertia is identified as the most sensitive modeling parameter, while the modal damping ratio is identified as the least sensitive modeling parameter. In summary, the proposed ASRUKF-FF algorithm exhibits a certain level of resilience against the influence of modeling errors.

Data Availability

The data used to support this study are available from the corresponding author upon reasonable request.

Conflicts of Interest

The authors declare that they have no conflicts of interest.

Authors' Contributions

Yanzhe Zhang and Yong Ding contributed equally to this research work.

Acknowledgments

The authors gratefully acknowledge the financial support by the National Key R&D Program of China (Grant nos. 2021YFB2600605 and 2021YFB2600600), the Key R&D Program of Hebei Province (Grant no. 19275405D), the Hebei Provincial Transport Bureau Research Program (Grant no. TH-201902), and the Scientific Research Fund of Institute of Engineering Mechanics, China Earthquake Administration (Grant no. 2019D22).

References

- [1] S. S. Bisht and M. P. Singh, "An adaptive unscented Kalman filter for tracking sudden stiffness changes," *Mechanical Systems and Signal Processing*, vol. 49, no. 1-2, pp. 181-195, 2014.
- [2] A. Calabrese, S. Strano, and M. Terzo, "Adaptive constrained unscented Kalman filtering for real-time nonlinear structural

- system identification,” *Structural Control and Health Monitoring*, vol. 25, no. 2, Article ID e2084, 2018.
- [3] E. Ghorbani, O. Buyukozturk, and Y. J. Cha, “Hybrid output-only structural system identification using random decrement and Kalman filter,” *Mechanical Systems and Signal Processing*, vol. 144, 2020.
 - [4] H. P. Wan and Y. Q. Ni, “A new approach for interval dynamic analysis of train-bridge system based on bayesian optimization,” *Journal of Engineering Mechanics*, vol. 146, no. 5, Article ID 04020029, 2020.
 - [5] Y. B. Yang, Z. L. Wang, K. Shi, H. Xu, and Y. T. Wu, “State-of-the-Art of vehicle-based methods for detecting various properties of highway bridges and railway tracks,” *International Journal of Structural Stability and Dynamics*, vol. 20, no. 13, Article ID 2041004, 2020.
 - [6] Y. Lei and N. Yang, “Simultaneous identification of structural time-varying physical parameters and unknown excitations using partial measurements,” *Engineering Structures*, vol. 214, Article ID 110672, 2020.
 - [7] Z. C. Wang, W. X. Ren, and G. D. Chen, “A Hilbert transform method for parameter identification of time-varying structures with observer techniques,” *Smart Materials and Structures*, vol. 21, no. 10, Article ID 105007, 9 pages, 2012.
 - [8] J. Chen and G. Y. Zhao, “Numerical and experimental investigation on parameter identification of time-varying dynamical system using Hilbert Transform and Empirical Mode Decomposition,” *Mathematical Problems in Engineering*, vol. 2014, no. 2, Article ID 568637, 15 pages, 2014.
 - [9] P. H. Ni, J. Li, H. Hao et al., “Time-varying system identification using variational mode decomposition,” *Structural Control and Health Monitoring*, vol. 25, no. 6, Article ID e2175, 2018.
 - [10] N. Yang, J. Li, and Y. Lei, “Identification of time-varying nonlinear structural physical parameters by integrated WMA and UKF/UKF-UI,” *Nonlinear Dynamics*, 2021.
 - [11] Y. Lei, J. Lu, and J. Huang, “Synthesize identification and control for smart structures with time-varying parameters under unknown earthquake excitation,” *Structural Control and Health Monitoring*, vol. 27, no. 4, 2020.
 - [12] S. Schleiter and O. Altay, “Identification of abrupt stiffness changes of structures with tuned mass dampers under sudden events,” *Structural Control and Health Monitoring*, vol. 27, no. 6, 2020.
 - [13] S. W. Doebling, C. R. Farrar, and M. B. Prime, “A summary review of vibration-based damage identification methods,” *The Shock and Vibration Digest*, vol. 30, no. 2, pp. 91–105, 1998.
 - [14] J. N. Yang and S. Lin, “Identification of parametric variations of structures based on least squares estimation and adaptive tracking technique,” *Journal of Engineering Mechanics*, vol. 131, pp. 290–298, 2005.
 - [15] J. N. Yang, S. L. Lin, H. W. Huang, and L. Zhou, “An adaptive extended Kalman filter for structural damage identification,” *Structural Control and Health Monitoring*, vol. 13, no. 4, pp. 849–867, 2006.
 - [16] C. M. Pappalardo and D. Guida, “Control of nonlinear vibrations using the adjoint method,” *Meccanica*, vol. 52, no. 11–12, pp. 2503–2526, 2017.
 - [17] M. Chung and T. Sato, “Structural identification using stochastic filtering techniques based on measurements from wireless data acquisition system,” *Steel Structures*, vol. 6, pp. 353–360, 2006.
 - [18] C. M. Pappalardo and D. Guida, “Adjoint-based optimization procedure for active vibration control of nonlinear mechanical systems,” *Journal of Dynamic Systems, Measurement, and Control*, vol. 139, no. 8, Article ID 081010, 2017.
 - [19] J. Humar, A. Bagchi, and H. P. Xu, “Performance of vibration-based techniques for the identification of structural damage,” *Structural Health Monitoring*, vol. 5, no. 3, pp. 215–241, 2006.
 - [20] E. Manoach, S. Samborski, A. Mitura, and J. Warminski, “Vibration based damage detection in composite beams under temperature variations using Poincaré maps,” *International Journal of Mechanical Sciences*, vol. 62, no. 1, pp. 120–132, 2012.
 - [21] L. J. Wang, Y. X. Xie, Z. J. Wu, Y. X. Du, and K. D. He, “A new fast convergent iteration regularization method,” *Engineering with Computers*, vol. 35, no. 1, pp. 127–138, 2018.
 - [22] S. Soyoz, M. Q. Feng, and E. Safak, *Real-time Structural Health Monitoring Incorporating Soil-Structure Interaction*, Hundredth Anniversary Earthquake Conference, San Francisco, CA, USA, 2006.
 - [23] J. X. Cao, H. B. Xiong, and L. Chen, “Procedure for parameter identification and mechanical properties assessment of CLT connections,” *Engineering Structures*, vol. 203, 2020.
 - [24] J. Naranjo-Pérez, J. F. Jiménez-Alonso, A. Pavic, and A. Sáez, “Finite-element-model updating of civil engineering structures using a hybrid UKF-HS algorithm,” *Structure and Infrastructure Engineering*, vol. 17, no. 5, pp. 620–637, 2020.
 - [25] S. J. Julier, J. K. Uhlmann, and H. F. Durrant-Whyte, “A New approach for filtering nonlinear systems,” in *Proceedings of the 1995 American Control Conference-ACC’95*, pp. 1628–1632, Seattle, WA, USA, June 1995.
 - [26] S. J. Julier, J. K. Uhlmann, and H. F. Durrant-Whyte, “A new method for the nonlinear transformation of means and covariances in filters and estimators,” *IEEE Transactions on Automatic Control*, vol. 45, no. 3, pp. 477–482, 2000.
 - [27] L. N. Guo, Y. Ding, Z. Wang, G. Xu, and B. Wu, “A dynamic load estimation method for nonlinear structures with unscented Kalman filter,” *Mechanical Systems and Signal Processing*, vol. 101, pp. 254–273, 2018.
 - [28] Y. Ding, L. N. Guo, and B. Y. Zhao, “Parameter identification for nonlinear structures by a constrained Kalman filter with limited input information,” *International Journal of Structural Stability and Dynamics*, vol. 17, no. 1, Article ID 1750010, 2017.
 - [29] R. van der Merwe and E. A. Wan, “The square-root unscented Kalman filter for state and parameter-estimation. 2001 IEEE international conference on acoustics, speech, and signal processing,” *Proceedings*, vol. 6, pp. 3461–3464, 2001.
 - [30] N. Wang, L. Y. Li, and Q. Wang, “Adaptive UKF-based parameter estimation for bouc-wen model of magneto-rheological elastomer materials,” *Journal of Aerospace Engineering*, vol. 32, no. 1, 2019.
 - [31] X. Xiao, X. Xu, and W. Shen, “Simultaneous identification of the frequencies and track irregularities of high-speed railway bridges from vehicle vibration data,” *Mechanical Systems and Signal Processing*, vol. 152, Article ID 107412, 2020.
 - [32] M. Zhao, X. Yu, M. Cui, X. Wang, and J. Wu, *Square Root Unscented Kalman Filter Based on Strong Tracking*, Springer International Publishing, Berlin, Germany, 2015.
 - [33] J. P. Yang, Y. Xia, Y. X. Yan, and L. M. Sun, “Time-varying structural parametric identification with MSTSRUKF,” *Journal of Vibration and Shock*, vol. 40, no. 23, pp. 74–82, 2021.
 - [34] R. Mohammadi Asl, Y. Shabbouei Hagh, S. Simani, and H. Handroos, “Adaptive square-root unscented Kalman filter: an experimental study of hydraulic actuator state estimation,”

- Mechanical Systems and Signal Processing*, vol. 132, pp. 670–691, 2019.
- [35] W. X. Su, “Application of Sage-Husa adaptive filtering algorithm for high precision SINS initial alignment,” in *Proceedings of the 2014 11th International Computer Conference on Wavelet Active Media Technology and Information Processing (ICCWAMTIP)*, pp. 359–364, Chengdu, China, December 2014.
- [36] Z. J. Chen, X. F. He, H. Jiang, and D. H. Li, “Research on initial alignment for large azimuth misalignment angle with Sage-Husa adaptive filtering,” in *Proceedings of the 2013 25th Chinese Control and Decision Conference (CCDC)*, pp. 1744–1749, Guiyang, China, May 2013.
- [37] J. Xing and P. Wu, “State of charge estimation of lithium-ion battery based on improved adaptive unscented Kalman filter,” *Sustainability*, vol. 13, no. 9, p. 5046, 2021.
- [38] R. Astroza, A. Alessandri, and J. P. Conte, “A dual adaptive filtering approach for nonlinear finite element model updating accounting for modeling uncertainty,” *Mechanical Systems and Signal Processing*, vol. 115, pp. 782–800, 2019.
- [39] W. Zhou, X. L. Li, J. Yi, and H. B. He, “A Novel UKF-RBF Method based on adaptive noise factor for fault diagnosis in pumping unit,” *IEEE Transactions on Industrial Informatics*, vol. 15, no. 3, pp. 1415–1424, 2019.
- [40] M. Song, R. Astroza, H. Ebrahimian, B. Moaveni, and C. Papadimitriou, “Adaptive Kalman filters for nonlinear finite element model updating,” *Mechanical Systems and Signal Processing*, vol. 143, Article ID 106837, 2020.
- [41] C. Sadhukhan, S. K. Mitra, M. K. Naskar, and M. Sharifpur, “Fault diagnosis of a nonlinear hybrid system using adaptive unscented Kalman filter bank,” *Engineering with Computers*, vol. 38, 2021.
- [42] Y. Yang and W. Gao, “An optimal adaptive Kalman filter,” *Journal of Geodesy*, vol. 80, no. 4, pp. 177–183, 2006.
- [43] S. Mariani and A. Ghisi, “Unscented Kalman filtering for nonlinear structural dynamics,” *Nonlinear Dynamics*, vol. 49, no. 1–2, pp. 131–150, 2007.
- [44] R. Jategaonkar and E. Plaetenschke, “Estimation of aircraft parameters using filter error methods and extended Kalman filter,” *DFVLR FB*, vol. 22, pp. 88–15, 1998.
- [45] G. Chowdhary and R. Jategaonkar, “Aerodynamic parameter estimation from flight data applying extended and unscented Kalman filter,” *Aerospace Science and Technology*, vol. 14, no. 2, pp. 106–117, 2010.
- [46] J. Lim, M. Shin, and W. Hwang, “Variants of extended Kalman filtering approaches for Bayesian tracking,” *International Journal of Robust and Nonlinear Control*, vol. 27, no. 2, pp. 319–346, 2017.
- [47] Y. Bar-Shalom, X. R. Li, and T. Kirubarajan, *Estimation with Application to Tracking and Navigation*, John Wiley and Sons Inc, NJ, USA, 2001.
- [48] R. H. Byrd, M. E. Hribar, and J. Nocedal, “An interior point algorithm for large-scale nonlinear programming,” *SIAM Journal on Optimization*, vol. 9, no. 4, pp. 877–900, 1999.
- [49] H. Shokravi, H. Shokravi, N. Bakhary, M. Heidarzaei, S. S. Rahimian Koloor, and M. Petru, “Vehicle-assisted techniques for health monitoring of bridges,” *Sensors*, vol. 20, no. 12, p. 3460, Basel, Switzerland, 2020.
- [50] A. Malekjafarian, P. J. McGetrick, and E. J. O'Brien, “A review of indirect bridge monitoring using passing vehicles,” *Shock and Vibration*, vol. 2015, Article ID 286139, 16 pages, 2015.
- [51] K. Lin, C. A. Tan, C. Ge, and H. Lu, “Time-varying transmissibility analysis of vehicle-bridge interaction systems with application to bridge-friendly vehicles,” *International Journal of Structural Stability and Dynamics*, vol. 22, 2021.
- [52] C. Ge, C. A. Tan, K. Lin, and L. Wang, “On the efficacy and accuracy of freezing technique for the response analysis of time-varying vehicle-bridge interaction systems,” *Journal of Sound and Vibration*, vol. 514, Article ID 116453, 2021.
- [53] Y. B. Yang and J. P. Yang, “State-of-the-Art review on modal identification and damage detection of bridges by moving test vehicles,” *International Journal of Structural Stability and Dynamics*, vol. 18, 2017.